UC Santa Barbara
UC Santa Barbara Electronic Theses and Dissertations

Title

Mapping Core-Collapse and Superluminous Supernova Observables to Their Progenitors

Permalink

https://escholarship.org/uc/item/00m450bs

Author

Hiramatsu, Daichi

Publication Date

2021

Peer reviewed|Thesis/dissertation

University of California
Santa Barbara

Mapping Core-Collapse and Superluminous Supernova Observables to Their Progenitors

A dissertation submitted in partial satisfaction
of the requirements for the degree

Doctor of Philosophy

in

Physics

by

Daichi Hiramatsu

Committee in charge:

    Professor D. Andrew Howell, Co-Chair
    Professor Lars Bildsten, Co-Chair
    Professor Timothy D. Brandt

September 2021

The dissertation of Daichi Hiramatsu is approved.

Professor Timothy D. Brandt

Professor Lars Bildsten, Committee Co-Chair

Professor D. Andrew Howell, Committee Co-Chair

September 2021

Mapping Core-Collapse and Superluminous Supernova Observables to Their Progenitors

To my parents who named me Daichi, the "Earth" in Japanese,
and let me explore the "Universe" in the USA.

Acknowledgements

Curriculum Vitæ
Daichi Hiramatsu

EDUCATION

University of California, Santa Barbara   September 2016 – September 2021
Ph.D. Physics, Astrophysics Emphasis, September 2021
M.A. Physics, Astrophysics Emphasis, July 2019
Advisor: Professor D. Andrew Howell

University of Hawaiʻi at Mānoa   August 2014 – May 2016
B.S. Physics, Astrophysics Minor

De Anza College   September 2012 – June 2014
Physics and Engineering Major

RESEARCH

Center for Astrophysics | Harvard & Smithsonian   starting October 2021
Postdoctoral Researcher
Time-Domain Research Group

Las Cumbres Observatory   January 2017 – September 2021
Graduate Student Researcher
Global Supernova Project
Supernova Key Project

Institute for Astronomy – University of Hawaiʻi   May 2015 – May 2016
Undergraduate Researcher
Unbiased Wide Range Survey for RR Lyraes with ATLAS
Extremely Low Metallicity Galaxies with the Subaru HSC
Cosmic Near-Infrared Background Fluctuations with the Subaru HSC

University of Hawaiʻi at Mānoa   January 2015 – August 2015
Undergraduate Researcher
Nonlinear Dynamics of Variable Stars with Kepler
Neutron Tomography

OBSERVING

Las Cumbres Observatory   January 2017 – Present
Imaging with SBIG, Sinistro, and Spectral
Spectroscopy with FLOYDS

Gemini Observatory   June 2017 – Present
Spectroscopy with the Gemini Multi-Object Spectrographs

Neil Gehrels *Swift* Observatory   October 2018 – Present
Imaging with the Ultraviolet/Optical Telescope
Imaging and Spectroscopy with the X-Ray Telescope

Hubble Space Telescope   June 2018 – December 2018
Imaging with the Wide Field Camera 3

Lick Observatory   October 2018
Imaging with the Nickel Direct Imaging Camera
Spectroscopy with the Kast Double Spectrograph and Hamilton Echelle Spectrograph

W. M. Keck Observatory   August 2018
Spectroscopy with the Low Resolution Imaging Spectrometer

Asteroid Terrestrial-impact Last Alert System   January 2016 – May 2016
Imaging with the Pathfinder

University of Hawaiʻi 2.2m Telescope   August 2015 – December 2015
Imaging with the Orthogonal Parallel Transfer Imaging Camera

TEACHING

University of California, Santa Barbara   September 2016 – June 2018
Teaching Assistant
ASTRO 1 – Basic Astronomy
ASTRO 2 – History of the Universe
PHYS 1 – Basic Physics
PHYS 3L – Basic Physics Laboratory
PHYS 132 – Stellar Structure and Evolution
PHYS 133 – Galaxies and Cosmology

University of Hawaiʻi at Mānoa   January 2015 – May 2016
Math and Science Tutor

De Anza College   September 2013 – June 2014
Math and Science Tutor

OUTREACH

Astronomy on Tap Santa Barbara   January 2018 – February 2021
Coordinator of free, short, public, astronomy-related presentations in a bar

AWARDS & HONORS

Academic Year Fellowship   Academic Year 2016–17
Department of Physics – University of California, Santa Barbara

The College of Natural Sciences Achievement Scholarship   Springs 2015 & 16
Department of Physics & Astronomy – University of Hawaiʻi at Mānoa

International Undergraduate Student Scholarship   Academic Years 2014–16
International Student Services – University of Hawaiʻi at Mānoa

Phi Beta Kappa   Spring 2016 – Present
Alpha of Hawaiʻi Chapter – University of Hawaiʻi at Mānoa

Golden Key   Fall 2015 – Present
International Honour Society Chapter – University of Hawaiʻi at Mānoa

Phi Theta Kappa   Spring 2013 – Present
Alpha Sigma Alpha Chapter – De Anza College

SOFTWARE

`lcogtgemini`   github.com/cmccully/lcogtgemini
Reduces spectra from the Gemini Observatory GMOS

`snhst`   github.com/cmccully/snhst
Measures photometry on images from the *Hubble Space Telescope*

`lcogtsnpipe`   github.com/LCOGT/lcogtsnpipe
Measures photometry on images from the Las Cumbres Observatory

`floyds_pipeline`   github.com/LCOGT/floyds_pipeline
Reduces spectra from the Las Cumbres Observatory FLOYDS spectrographs

PRESENTATIONS

Invited Talks

5. Caltech/IPAC Lunch Seminar, Pasadena, CA, USA (virtual)   January 2021
   "Progenitor Mass Spectrum of Core-Collapse Supernovae"

4. NAOJ Science Colloquium, Mitaka, Tokyo, Japan (virtual)   January 2021
   "Progenitor Mass Spectrum of Core-Collapse Supernovae"

3. ASIAA Colloquium, Taipei, Taiwan, R.O.C.   January 2020
   "Recent Advancements in Core-collapse Supernova Observation"

2. Kavili IPMU APEC Seminar, Kashiwa, Chiba, Japan   November 2019
   "[Recent Advancements in Core-collapse Supernova Observation](#)"

1. Time-domain astronomy workshop 2019, Sendai, Miyagai, Japan   October 2019
   "Hydrogen-rich Supernova Observation and Modeling"

Contributed Talks

3. ASJ Autumn Annual Meeting, Kyoto, Kyoto, Japan (virtual)   September 2021
   "The electron-capture supernova 2018zd"

2. Stellar deaths and their diversity, Mitaka, Tokyo, Japan   January 2019
   "[Type II Short-plateau Supernovae](#)"

1. Chaos Among the Stars?, Honolulu, HI, USA August 2015
   "*Extracting Fractal Dimensions from Uneven Time Series*"

PUBLICATIONS

Lead Author

3. **Hiramatsu, D.**, Moriya, T. J., Howell, D. A., Arcavi, I., Burke, J. et al., "*Super-linear Type II Superluminous Supernovae 2017fck and 2019cmv: A Possible Origin from Interacting Type Ia Supernovae*," in prep.

2. **Hiramatsu, D.**, Howell, D. A., Moriya, T. J., Goldberg, J. A., Hosseinzadeh, G. et al., 2021, "*Luminous Type II Short-Plateau Supernovae 2006Y, 2006ai, and 2016egz: A Transitional Class from Stripped Massive Red Supergiants*," ApJ, 913, 55

1. **Hiramatsu, D.**, Howell, D. A., Van Dyk, S. D., Goldberg, J. A., Maeda, K. et al., 2021, "*The electron-capture origin of supernova 2018zd*," Nature Astronomy, 5, 903

Major Contribution

8. Jacobson-Galán, W. V., Margutti, R., Kilpatrick, C. D., **Hiramatsu, D.**, Perets, H. et al., 2020, "*SN 2019ehk: A Double-peaked Ca-rich Transient with Luminous X-Ray Emission and Shock-ionized Spectral Features*," ApJ, 898, 166

7. Pellegrino, C., Howell, D. A., Sarbadhicary, S. K., Burke, J., **Hiramatsu, D.**, et al., 2020, "*Constraining the Source of the High-velocity Ejecta in Type Ia SN 2019ein*," ApJ, 897, 159

6. French, K. D., Arcavi, I., Zabludoff, A. I., Stone, N., **Hiramatsu, D.**, et al. 2020, "*The Structure of Tidal Disruption Event Host Galaxies on Scales of Tens to Thousands of Parsecs*," ApJ, 891, 93

5. Gangopadhyay, A., Misra, K., **Hiramatsu, D.**, Wang, S., Hosseinzadeh, G. et al. 2020, "*Flash ionization signatures in the type Ibn supernova SN 2019uo*," ApJ, 889, 170

4. Anderson, J. P., Pessi, P. J., Dessart, L., Inserra, C., **Hiramatsu, D.**, et al., 2018, "*A nearby super-luminous supernova with a long pre-maximum & 'plateau' and strong C II features*," A&A, 620, 67

3. Sand, D. J., Graham, M. L., Botyánszki, J., **Hiramatsu, D.**, McCully, C., et al., 2018, "*Nebular Spectroscopy of the 'Blue Bump' Type Ia Supernova 2017cbv*," ApJ, 863, 24

2. Graham, M. L., Kumar, S., Hosseinzadeh, G., **Hiramatsu, D.**, Arcavi, I., et al., 2017, "*Nebular-Phase Spectra of Nearby Type Ia Supernovae*," MNRAS, 472, 3437

1. McCully, C., **Hiramatsu, D.**, Howell, D. A., Hosseinzadeh, G., Arcavi, I., et al. 2017, "*The rapid reddening and featureless optical spectra of the optical counterpart of GW170817, AT 2017gfo, during the first four days*," ApJL, 848, L32

Collaboration

45. Kilpatrick, C. D. et al., 2021, "*The Gravity Collective: A Search for the Electromagnetic Counterpart to the Neutron Star-Black Hole Merger GW190814*," ApJ, accepted, arXiv:2106.06897

44. Sand, D. J. et al., 2021, "*Circumstellar Medium Constraints on the Environment of Two Nearby Type Ia Supernovae: SN 2017cbv and SN 2020nlb*," ApJ, accepted, arXiv:2108.11407

43. Jencson, J. E. et al., 2021, "*AT 2019qyl in NGC 300: Early Outflow Collisions for a Very Fast Nova in a Symbiotic Binary*," ApJ, accepted, arXiv:2102.11291

42. Burke, J. et al., 2021, "*A Bright Ultraviolet Excess in the Transitional 02es-like Type Ia Supernova 2019yvq*," ApJ, accepted, arXiv:2101.06345

41. Zeng, X. et al., 2021, "*SN 2017fgc: A Fast-Expanding Type Ia Supernova Exploded in Massive Shell Galaxy NGC 474*," ApJ, accepted, arXiv:2106.12164

40. Armstrong, P. et al., 2021, "*SN2017jgh - A high-cadence complete shock cooling lightcurve of a SN IIb with the Kepler telescope*," MNRAS, 507, 3125

39. Parrag, E. et al., 2021, "*SN 2019hcc: a Type II supernova displaying early O II lines*," MNRAS, 506, 4819

38. Medler, K. et al., 2021, "*SN 2020cpg: an energetic link between type IIb and Ib supernovae*," MNRAS, 506, 1832

37. Utrobin, V. P. et al., 2021, "*Enormous explosion energy of Type IIP SN 2017gmr with bipolar Ni-56 ejecta*," MNRAS, 505, 116

36. Gutiérrez, C. P. et al., 2021, "*The double-peaked type Ic Supernova 2019cad: another SN 2005bf-like object*," MNRAS, 504, 4907

35. Pritchard, T. A. et al., 2021, "*The Exotic Type Ic Broad-lined Supernova SN 2018gep: Blurring the Line between Supernovae and Fast Optical Transients*," ApJ, 915, 121

34. Cannizzaro, G. et al., 2021, "*Accretion disc cooling and narrow absorption lines in the tidal disruption event AT 2019dsg*," MNRAS, 504, 792

33. Baltay, C. et al., 2021, "*Low-redshift Type Ia Supernova from the LSQ/LCO Collaboration*," PASP, 133, 4002

32. Fiore, A. et al., 2021, "*SN 2017gci: a nearby Type I Superluminous Supernova with a bumpy tail*," MNRAS, 502, 2120

31. Xiang, D. et al., 2021, "*The Peculiar Transient AT2018cow: A Possible Origin of a Type Ibn/IIn Supernova*," ApJ, 910, 42

30. Zeng, X. et al., 2021, "*SN 2017hpa: A Nearby Carbon-rich Type Ia Supernova with a Large Velocity Gradient*," ApJ, 909, 176

29. Khetan, N. et al., 2021, "*A new measurement of the Hubble constant using Type Ia supernovae calibrated with surface brightness fluctuations*," A&A, 647, 72

28. Malyali, A. et al., 2021, "*AT 2019avd: a novel addition to the diverse population of nuclear transients*," A&A, 647, 9

27. Barna, B. et al., 2021, "*SN 2019muj – a well-observed Type Iax supernova that bridges the luminosity gap of the class*," MNRAS, 501, 1078

26. Rho, J. et al., 2021, "*Near-infrared and Optical Observations of Type Ic SN 2020oi and Broad-lined Type Ic SN 2020bvc: Carbon Monoxide, Dust, and High-velocity Supernova Ejecta*," ApJ, 908, 232

25. Tartaglia, L. et al., 2021, "*The Early Discovery of SN 2017ahn: Signatures of Persistent Interaction in a Fast-declining Type II Supernova*," ApJ, 907, 52

24. Dong, Y. et al., 2021, "*Supernova 2018cuf: A Type IIP Supernova with a Slow Fall from Plateau*," ApJ, 906, 56

23. Prentice, S. J. et al., 2020, "*SN 2018gjx reveals that some SNe Ibn are SNe IIb exploding in dense circumstellar material*," MNRAS, 499, 1450

22. Gutiérrez, C. P. et al., 2020, "*SN 2017ivv: two years of evolution of a transitional Type II supernova*," MNRAS, 499, 974

21. Nicholl, M. et al., 2020, "*An outflow powers the optical rise of the nearby, fast-evolving tidal disruption event AT2019qiz*," MNRAS, 499, 482

20. Short, P. et al., 2020, "*The tidal disruption event AT 2018hyz - I. Double-peaked emission lines and a flat Balmer decrement*," MNRAS, 498, 4119

19. Yang, Y. et al., 2020, "*The Young and Nearby Normal Type Ia Supernova 2018gv: UV-Optical Observations and the Earliest Spectropolarimetry*," ApJ, 902, 46

18. Gomez, S. et al., 2020, "*The Tidal Disruption Event AT 2018hyz II: Light-curve modelling of a partially disrupted star*," MNRAS, 497, 1925

17. Müller-Bravo, T. E. et al., 2020, "*The low-luminosity Type II SN 2016aqf: a well-monitored spectral evolution of the Ni/Fe abundance ration*," MNRAS, 497, 361

16. Bostroem, K. A. et al., 2020, "*Discovery and Rapid Follow-up Observations of the Unusual Type II SN 2018ivc in NGC 1068*," ApJ, 895, 31

15. Han, X. et al., 2020, "*SN 2017cfd: A Normal Type Ia Supernova Discovered Very Young*," ApJ, 892, 142

14. Leloudas, G. et al., 2019, "*The Spectral Evolution of AT 2018dyb and the Presence of Metal Lines in Tidal Disruption Events*," ApJ, 887, 218

13. Andrews, J. E. et al., 2019, "*SN 2017gmr: An energetic Type II-P supernova with asymmetries*," ApJ, 885, 43

12. Galbany, L. et al., 2019, "*Evidence for a Chandrasekhar-mass explosion in the Ca-strong 1991bg-like type Ia supernova 2016hnk*," A&A, 630, 76

11. Trakhtenbrot, B. et al., 2019, "*1ES 1927+654: an AGN Caught Changing Look on a Timescale of Months*," ApJ, 883, 94

10. Pastorello, A. et al., 2019, "*A luminous stellar outburst during a long-lasting eruptive phase first, and then SN IIn 2018cnf*," A&A, 628, 93

9. Brown, P. J., et al., 2019, "*Red and Reddened: Ultraviolet through Near-Infrared Observations of Type Ia Supernova 2017erp*," ApJ, 877, 152

8. Sand, D. J., et al., 2019, "*Nebular Hα Limits for Fast Declining SNe Ia*," ApJL, 877, 4

7. Szalai, T., et al., 2019, "*The Type II-P Supernova 2017eaw: From Explosion to the Nebular Phase*," ApJ, 876, 19

6. Hosseinzadeh, G., et al., 2019, "*Type Ibn Supernovae May not all Come from Massive Stars*," ApJL, 871, 9

5. Dimitriadis, G., et al., 2019, "*K2 Observations of SN 2018oh Reveal a Two-component Rising Light Curve for a Type Ia Supernova*," ApJ, 870, 1

4. Li, W., et al., 2019, "*Photometric and Spectroscopic Properties of Type Ia Supernova 2018oh with Early Excess Emission from the Kepler 2 Observations*," ApJ, 870, 12

3. Taddia, F., et al., 2019, "*Analysis of broad-lined Type Ic supernovae from the (intermediate) Palomar Transient Factory*," A&A, 621, 71

2. Sollerman, J., et al., 2019, "*Late-time observations of the extraordinary Type II supernova iPTF14hls*," A&A, 621, 30

1. LIGO Scientific Collaboration and Virgo Collaboration et al., 2017, "*Multi-Messenger Observations of a Binary Neutron Star Merger*," ApJL, 848, 12

Submitted

3. Wang, Q. et al., 2021, "*SN2018agk: A prototypical Type Ia Supernova with a smooth power-law rise in Kepler (K2)*," ApJ, submitted, arXiv:2108.13607

2. Brennan, S. J. et al., 2021, "*An impostor among us II: Progenitor, environment, and modelling of AT 2016jbu*," MNRAS, submitted, arXiv:2102.09576

1. Brennan, S. J. et al., 2021, "*An impostor among us I: Photometric and spectroscopic evolution of AT 2016jbu*," MNRAS, submitted, arXiv:2102.09572

Astronomical Circulars

221 transient classifications and circulars (89 as lead author).

Abstract

Mapping Core-Collapse and Superluminous Supernova Observables to Their Progenitors

by

Daichi Hiramatsu

New wide-field and high-cadence transient surveys have enabled us to watch supernovae (SNe) from the moment of explosion. Paired with rapid and continuous monitoring facilities, these observations have revealed unprecedented features that bridge our understanding of their progenitor systems to explosion mechanisms. The Global Supernova Project (GSP) is a world-wide collaboration that uses Las Cumbres Observatory and various other ground- and space-based telescopes to study SNe from their discovery through all phases of follow-up. Here, I present three major advancements in core-collapse and superluminous SN observations from GSP and numerical modeling with `MESA` and `STELLA`. (1) SN 2018zd is a hydrogen-rich (Type II) SN discovered within a few hours of explosion. Its early ultraviolet color and narrow emission lines, along with light-curve morphology and nebular emission lines, are all consistent with an electron-capture SN explosion of a super-asymptotic giant branch star – the lowest-mass Type II SN. (2) Short-plateau SNe are luminous Type II core-collapse SNe with short light-curve plateaus, indicating significant pre-explosion mass loss resulting in partially stripped hydrogen-rich envelopes and early circumstellar material (CSM) interaction. Our light-curve model grid puts them in a rare transitional class from stripped red supergiants on the high-mass end of Type II SN progenitors. (3) Superlinear superluminous SNe (SLSNe) are Type II SLSNe with superlinear light curves powered by CSM interaction. Sample comparison and modeling suggest that the superlinear SLSNe are possibly compatible to thermonuclear SNe interacting with massive CSM which might be produced during common envelope evolution.

Contents

Chapter 1

Introduction

1.1 Supernovae

Supernovae (SNe) are the terminal explosions of massive stars or white dwarfs (WDs) that are so bright that they overshine their host galaxies and can be observed from cosmological distances (Fig. 1.1). SNe produce effects on nearly every astrophysical scale, from atomic, as sites of nucleosynthesis; to stellar, as progenitors of neutron stars and black holes; to galactic, as contributors to chemical evolution; to cosmological, as standardizable candles. They are important as endpoints of stellar evolution and as probes of extreme physics, but remarkably, remain poorly understood in certain regimes.

The majority of massive stars (zero-age main-sequence masses roughly above 9 solar masses; $M_{\mathrm{ZAMS}} \gtrsim 9\,M_\odot$) end their lives when their iron (Fe) cores collapse and explode as hydrogen-rich (H-rich) Type II SNe (SNe II; see Smartt 2009, 2015 for reviews) with subclasses: Type IIP SNe (SNe IIP; light-curve 'p'lateau of ~ 100 days); Type IIL SNe (SNe IIL; 'l'inear decline light curve); and Type IIb SNe (SNe IIb; spectrum dominated initially by H and then by He due to mostly stripped H-rich envelope; see Arcavi 2017 for a review). Another subclass, Type IIn SNe (SNe IIn), shows 'n'arrow H emission lines, indicating strong interaction between SN ejecta and circumstellar material (CSM) from pre-explosion mass-loss activities (see Smith 2017 for a review). While there is consensus
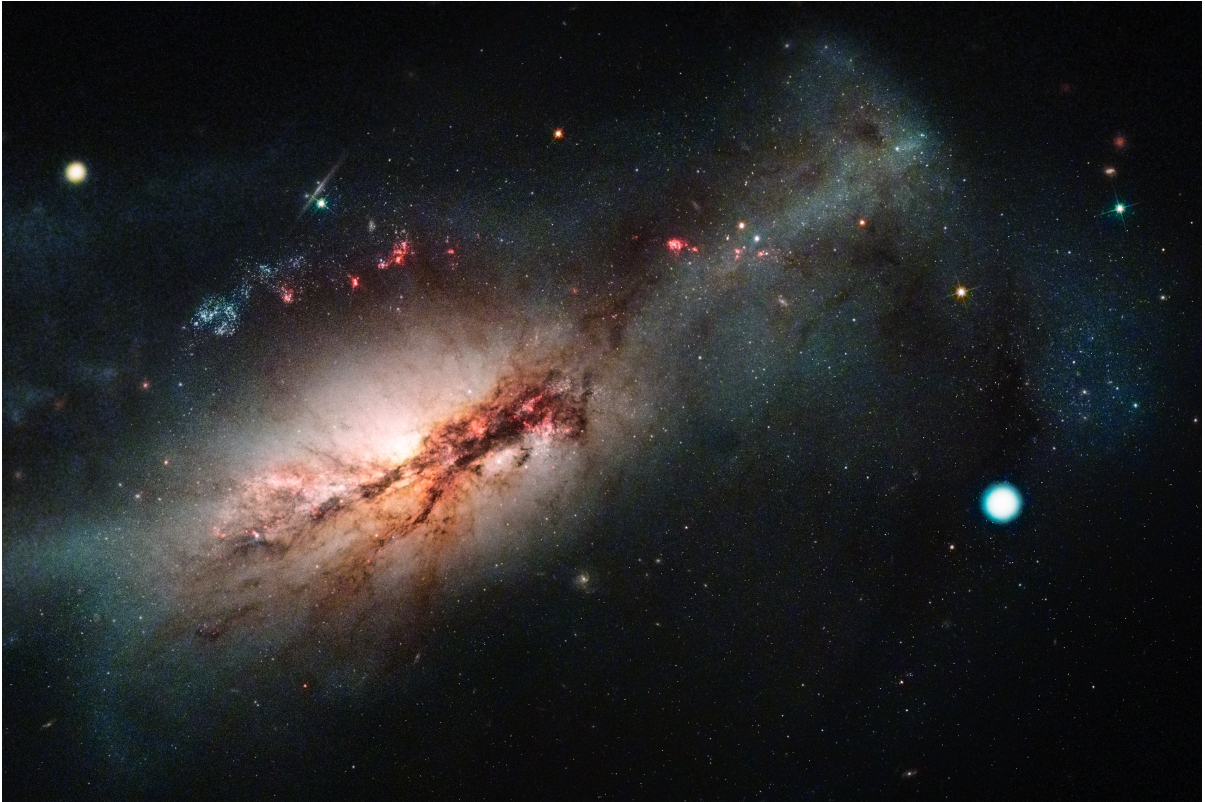
Figure 1.1: Las Cumbres Observatory and *Hubble Space Telescope* color composite of the electron-capture supernova 2018zd (the large white dot on the right) hosted in the starburst galaxy NGC 2146 (towards the left), courtesy of Joseph DePasquale (STScI) and Las Cumbres Observatory.

that the progenitors of SNe IIP are red supergiants (RSGs; $\simeq$ 9–18 $M_\odot$), the fate at the low- and high-mass ends of SN IIP progenitor spectrum and their nucleosynthetic contributions to galactic chemical evolution are uncertain. The complicated evolutionary path in the low-mass end (6–9 $M_\odot$; accounting for $\simeq 50\%$ of massive stars $\geq 6\,M_\odot$) results in diverse outcomes, from C+O WDs, to O+Ne WDs, to super-asymptotic giant branch (SAGB) stars exploding as electron-capture SNe (ECSNe; see Doherty et al. 2017 for a review). The apparent lack of RSGs in the high-mass end (18–25 $M_\odot$) in observed SN IIP progenitor samples (the so-called "RSG problem"; Smartt 2009, 2015) also challenges our understanding of the end products of massive-star evolution: either Fe core-collapse SNe (CCSNe)+neutron stars/black holes, or direct collapse to black holes.

Superluminous SNe (SLSNe) are another mysterious class that is characterized by bright light curves ($\lesssim -21$ mag) requiring additional power sources beyond those of traditional SNe (see Gal-Yam 2012, 2019; Howell 2017; Moriya et al. 2018b for reviews). CSM interaction is thought to be a main power source for H-rich SLSNe (SLSNe-II); however, the nature of underlying SNe and their progenitor systems remain elusive. On the other hand, H-poor Type Ia SNe (SNe Ia) are the thermonuclear explosions of CO WDs whose exact progenitor systems and explosion mechanisms are still open questions (see Howell 2011; Maoz et al. 2014; Maguire 2016 for reviews), despite their cosmological applications (Riess et al. 1998; Perlmutter et al. 1999). In this context, SNe Ia-CSM represent an intriguing intersection between SNe IIn/SLSNe-II and SNe Ia in that they show H emission lines on top of a diluted SN Ia-like continuum (e.g., Silverman et al. 2013b). If SNe Ia-CSM indeed originate from SNe Ia, then these are the best candidates for the single-degenerate scenario, one of the two main leading SN Ia formation channels, in which a CO WD accrete material from a nondegerate stellar companion with H-rich atmosphere (see Taam & Sandquist 2000 for a review).

1.2   Las Cumbres Observatory

Las Cumbres Observatory (LCO; Brown et al. 2013) consists of a network of twenty-five robotic optical telescopes, scheduled by custom software, at seven sites around the world, allowing prompt and continuous monitoring of transients anywhere in the sky (Fig. 1.2). Our SN group at LCO consists of eight members triggering, monitoring, and reducing all SN observations, providing each member with a significant role in this unique science. In addition to SN research, we are one of the first six teams that independently discovered the optical counterpart of a gravitational wave source, the first kilonova (Arcavi et al. 2017; Abbott et al. 2017), in which I co-led our optical spectroscopic follow-up
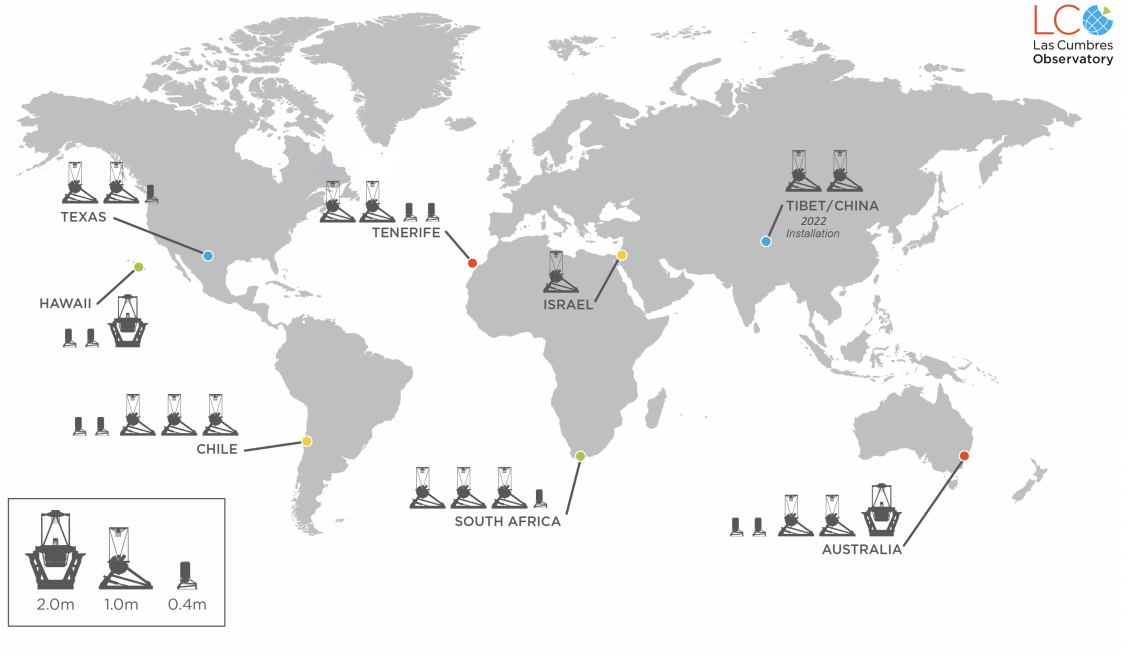
Figure 1.2: A map of Las Cumbres Observatory's global telescope network with twenty-five robotic 2 m, 1 m, and 0.4 m telescopes, as of August 2021. The two 1 m telescopes in Tenerife have come online in 2021, and the additional two 1 m telescopes in Tibet will be installed in 2022. The growing global telescope network allows unprecedented time coverage of astronomical transients.

campaign (McCully et al. 2017), although I will not focus on the topic in this dissertation.

The Global Supernova Project (GSP; Howell & Global Supernova Project 2017), a Key Project at LCO, is a global collaboration of more than 150 SN observers and theorists using more than 3,000 hours of LCO telescope time to obtain light curves and spectra of more than 150 SNe per year. The collaboration works with several survey groups, such as Asteroid Terrestrial-impact Last Alert System (ATLAS; Tonry 2011) and Distance Less Than 40 Mpc (DLT40; Tartaglia et al. 2018), for prompt responses to their new discoveries. I initiated a collaboration with amateur SN hunter Koichi Itagaki for quick follow-ups of his galaxy-targeted ($\lesssim$ 30 Mpc), high-cadence ($\sim$ 1 day) survey using his network of telescopes in Japan, which resulted in the discovery of an ECSN (see below). We also collaborate with the Public ESO Spectroscopic Survey for Transient Objects

(PESSTO; Smartt et al. 2015) that uses the 3.58 m New Technology Telescope (NTT) for SN classifications and follow-ups. In addition, our collaborators provide access to the world's largest ground-based telescopes, such as the W. M. Keck Observatory and Gemini Observatory, as well as space-based telescopes, such as the Neil Gehrels *Swift* Observatory and *Hubble Space Telescope* (*HST*), for covering a wide electromagnetic spectral range: X-ray, ultraviolet (UV), optical, near-infrared (NIR), and mid-infrared (MIR) to study SNe from multiple aspects.

1.3   Mapping Methods

The work presented in this dissertation takes advantage of the data sets of aforementioned extreme supernovae (§ 1.1) with unprecedented temporal coverage from LCO/GSP (§ 1.2). Along with novel analytical and numerical methods, I utilize the 1D stellar evolution code MESA (Paxton et al. 2011, 2013, 2015, 2018, 2019) and the 1D multi-frequency radiation-hydrodynamics code STELLA (Blinnikov et al. 1998, 2000, 2006) for computing massive-star evolution and SN light curves, respectively, to map their observables to their progenitor systems (Fig. 1.3). Progenitor identifications in pre-explosion *HST* images (if available in the archive) are the most direct means to determine the progenitor masses and radii (see Van Dyk 2016 for a review). From the modeling of well-observed light curves (e.g., with LCO and *Swift*), the explosion properties (e.g., ejecta mass and explosion energy) and CSM distributions can be inferred (e.g., Hiramatsu et al. 2021a, b). Well-observed spectral sequences (e.g., with LCO, NTT, Keck, and Gemini), along with synthetic models, give estimates on the progenitor chemical composition and SN nucleosynthetic yields (see Jerkstrand 2017 for a review).

The following three chapters cover the main findings of this dissertation. Chapter 2 presents the discovery of the first convincing candidate of an ECSN from an SAGB
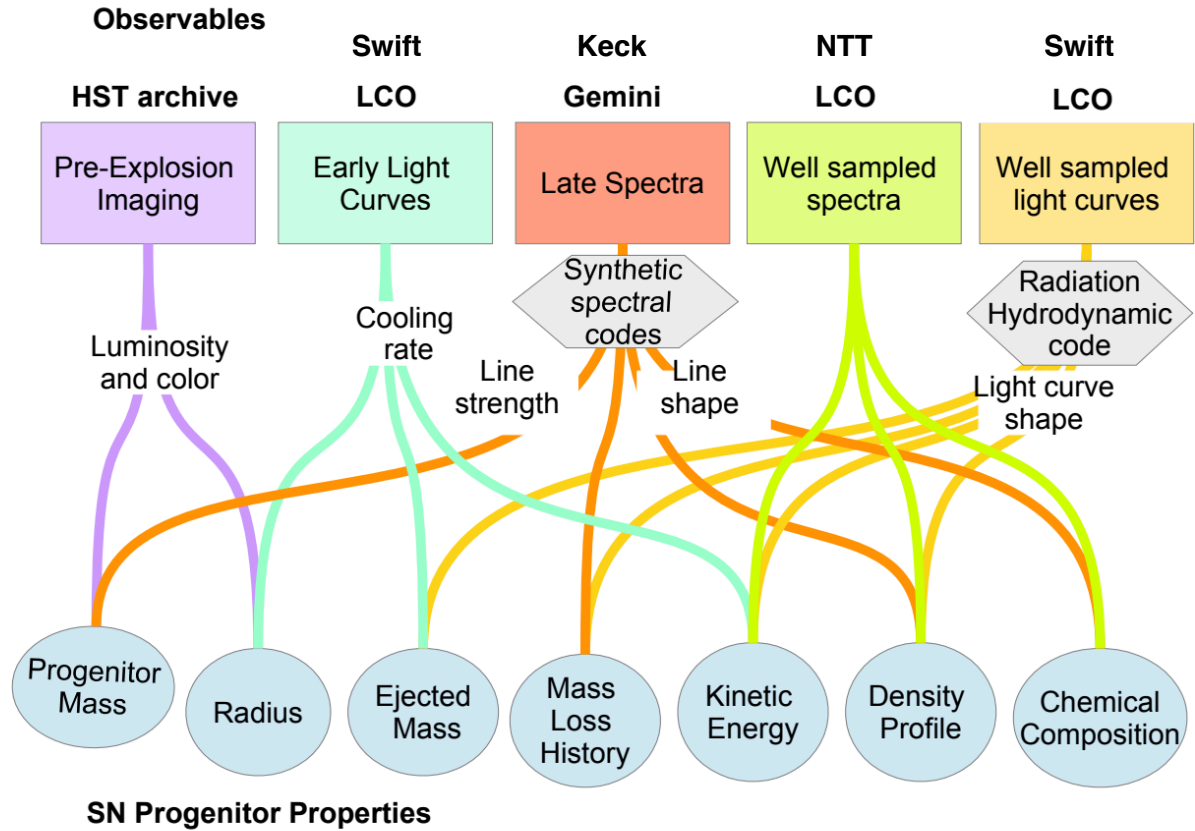
Figure 1.3: A summary of mapping methods used in this work. LCO/GSP can provide all the above SN observables, and numerical modeling along with other novel analytical methods are utilized to extract SN progenitor properties.

star – a third explosion mechanism theorized 40 years ago, representing the low-mass end ($\sim 8\,M_\odot$) of the SN IIP progenitor mass spectrum. In contrast, Chapter 3 analyzes luminous SNe IIP with short plateaus (~ 50–70 days as compared to typical ~ 100 days), finding their rare transitional nature between SNe IIL and IIb from stripped RSGs on the high-mass end ($\gtrsim 18\,M_\odot$). Finally, Chapter 4 explores SLSNe-II with superlinear light curves and shows that they are possibly compatible to SNe Ia-CSM with massive CSM (~ 1–$15\,M_\odot$) which might result from the common envelope evolution of CO WDs and giant or supergiant companion stars.

Chapter 2

The Electron-Capture Origin of Supernova 2018zd

This chapter is reproduced from Hiramatsu et al. (2021b) by permission of Springer Nature. I would like to thank my coauthors, without whom this work would not have been possible: D. Andrew Howell, Schuyler D. Van Dyk, Jared A. Goldberg, Keiichi Maeda, Takashi J. Moriya, Nozomu Tominaga, Ken'ichi Nomoto, Griffin Hosseinzade, Iair Arcavi, Curtis McCully, Jamison Burke, K. Azalee Bostroem, Stefano Valenti, Yize Dong, Peter J. Brown, Jennifer E. Andrews, Christopher Bilinski, G. Grant Williams, Paul S. Smith, Nathan Smith, David J. Sand, Gagandeep S. Anand, Chengyuan Xu, Alexei V. Filippenko, Melina C. Bersten, Gastón Folatelli, Patrick L. Kelly, Toshihide Noguchi, and Koichi Itagaki.

2.1 Introduction

In the transitional mass range (~ 8–$10\,M_\odot$) between WD formation and Fe CCSNe, stars are expected to produce an ECSN. Theoretically, these progenitors are thought to be SAGB stars with a degenerate O+Ne+Mg core, and electron capture onto Ne and Mg nuclei should initiate core collapse (Miyaji et al. 1980; Nomoto et al. 1982; Nomoto 1984, 1987). However, no SNe have unequivocally been identified from an electron-capture

origin, partly because of uncertainty in theoretical predictions. Here we present six indicators of ECSNe and show that SN 2018zd is the only known SN having strong evidence for or consistent with all six: progenitor identification, CSM, chemical composition (Poelarends et al. 2008; Jones et al. 2013; Doherty et al. 2017), explosion energy, light curve, and nucleosynthesis (Kitaura et al. 2006; Janka et al. 2008; Tominaga et al. 2013; Wanajo et al. 2009; Jerkstrand et al. 2018). For SN 2018zd, we infer an SAGB progenitor based on the faint candidate in the pre-explosion images and the chemically-enriched CSM revealed by the early UV colours and flash spectroscopy. The light-curve morphology and nebular emission lines can be explained by the low explosion energy and neutron-rich nucleosynthesis produced in an ECSN. This identification provides insights into the complex stellar evolution, SN physics, cosmic nucleosynthesis, and remnant populations in the transitional mass range.

2.2   Main

On 2018 Mar. 2.49 (UT dates are used throughout), we discovered AT 2018zd (Itagaki 2018) at an unfiltered optical magnitude of 17.8 in the outskirts of NGC 2146 (redshift $z = 0.002979$; de Vaucouleurs et al. 1991), where pre-explosion *HST* and *Spitzer Space Telescope* images yield a faint progenitor candidate (Figs. 2.5 & 2.6, and §2.3.3). Combined with our pre-discovery detection at 18.1 mag on 2018 Mar. 1.54, we estimate an explosion epoch of 2018 Mar. 1.4 ± 0.1 (~ 3 hr before the first detection; Fig. 2.7) and use it as a reference epoch for all phases. At 4.9 days post explosion, we classified AT 2018zd as a young Type II SN, designating it SN 2018zd (Arcavi et al. 2018). Over time, SN 2018zd developed a plateau and broad Balmer-series P Cygni lines in the optical light curves and spectra (respectively), further classifying it as a Type IIP SN (Figs. 2.7 & 2.8). The luminosity distance of NGC 2146 is uncertain, ranging from 11 Mpc

to 18 Mpc in the literature (Adamo et al. 2012). Thus, we apply the standard candle method and adopt a distance of 9.6 ± 1.0 Mpc (§ 2.3.2). Because of the wide distance range, we focus mainly on distance-independent measurements.

Unlike Fe CCSN explosions of RSG stars, ECSN explosions of SAGB stars are robustly realised by first-principle simulations, facilitated by the steep density gradient outside the degenerate core. Simulations consistently predict explosion energy ($\sim 2 \times 10^{50}$ erg) and ^{56}Ni yield ($\sim 3 \times 10^{-3} M_\odot$, with an upper limit $\lesssim 10^{-2} M_\odot$) that are an order of magnitude lower than those observed for typical Fe CCSNe (Kitaura et al. 2006; Janka et al. 2008; Wanajo et al. 2009), but are consistent within the lowest-mass Fe CCSNe (§ 2.4.6). Despite the low explosion energy, the low mass and large radius of an SAGB star result in a light-curve morphology virtually identical to that of Type IIP SNe, except for a larger drop (~ 4 mag) from the plateau to the radioactive decay tail, owing to the low ^{56}Ni production (Tominaga et al. 2013).

Among a sample of well-observed Type II SN light curves (Valenti et al. 2016; Fig. 2.1), SN 2018zd fits in the Type IIP morphology and displays the largest plateau drop (~ 3.8 mag). Even among a sample of low-luminosity Type IIP SNe (Spiro et al. 2014) that often show larger plateau drops than other Type II subclasses (Fig. 2.1), SN 2018zd is comparable to SNe 1999eu and 2006ov with the largest drops ever observed, indicating an intrinsically low ^{56}Ni production. For SNe 1999eu and 2006ov, the lack of additional data prevents the investigations of other ECSN indicators; the light curves alone cannot be conclusive evidence (see § 2.3.4 for the light-curve degeneracy). The tail decline rate of SN 2018zd is consistent with the ^{56}Co heating rate, and an estimated ^{56}Ni mass is $(8.6 \pm 0.5) \times 10^{-3} M_\odot$ at the assumed luminosity distance of 9.6 Mpc (Fig. 2.7). This is larger than the canonical ^{56}Ni yield for ECSNe, but still within the upper limit (see also § 2.4.6 for the effect of distance uncertainty).

As SAGB stars are thought to have mass-loss rates ($\dot{M} \approx 10^{-4} M_\odot \, \mathrm{yr}^{-1}$) a few orders
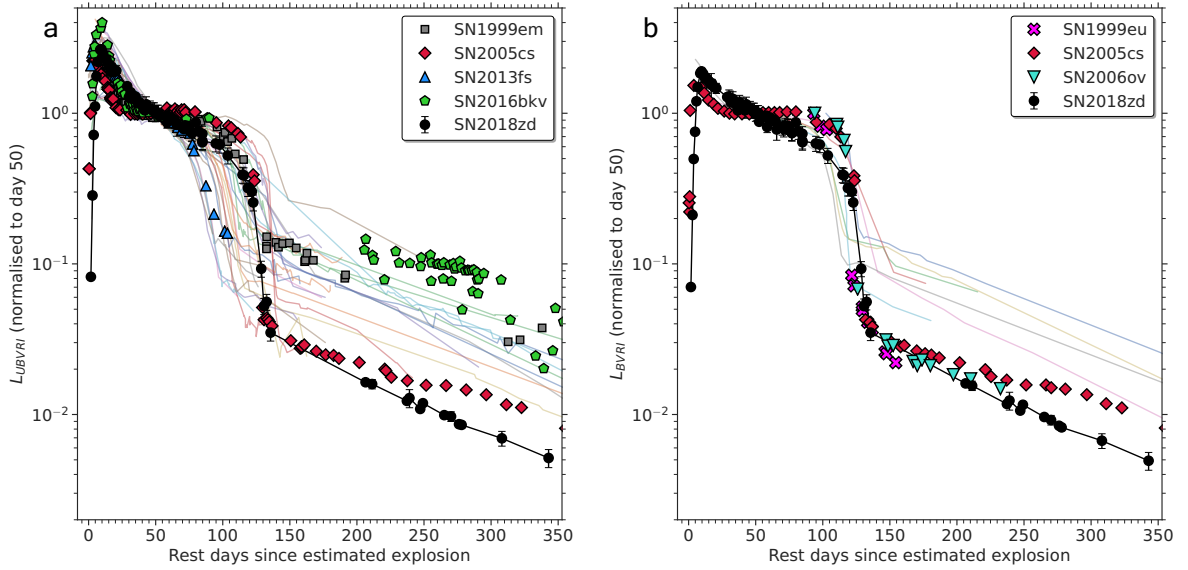
Figure 2.1:   **Normalised pseudobolometric light curves. a,** Comparison of
the normalised pseudobolometric (*UBVRI*; § 2.4.1) light curve of SN 2018zd with a
well-observed Type II SN sample (Valenti et al. 2016; transparent lines), including
archetypal SN 1999em, low-luminosity SN 2005cs, and early-flash SN 2013fs, along
with low-luminosity and early-flash SN 2016bkv (Hosseinzadeh et al. 2018). **b,** Com-
parison of the normalised pseudobolometric (*BVRI*) light curve of SN 2018zd with
a low-luminosity Type IIP SN sample (Spiro et al. 2014), including SNe 1999eu and
2006ov with the largest plateau drops ever (to our knowledge). Error bars denote 1σ
uncertainties. Because of the distance uncertainty of SN 2018zd, we normalise each
light curve to day 50 and make the comparisons distance independent. SN 2018zd
shows the largest plateau drop and is comparable to that of SNe 1999eu and 2006ov,
indicating an intrinsically low ^{56}Ni production.

of magnitude higher than those of RSG stars of similar initial mass (Poelarends et al.
2008), the CSM density is expected to be a few orders of magnitude higher, as it scales as
$\rho_{\mathrm{CSM}} \propto \dot{M}/v_{\mathrm{wind}}$, assuming constant-wind mass loss with similar SAGB and RSG wind
velocities v_{wind} (Moriya et al. 2014). Compared with RSG stars, the CSM composition
of SAGB stars can be He-, C-, and N-rich, but O-poor, depending on the efficiency of
the SAGB dredge-up and dredge-out that bring the partial H- and He-burning products
to the stellar surface (Jones et al. 2013; Doherty et al. 2017).

In a sample of Type II SN UV colours (Valenti et al. 2016), SN 2018zd stands out,
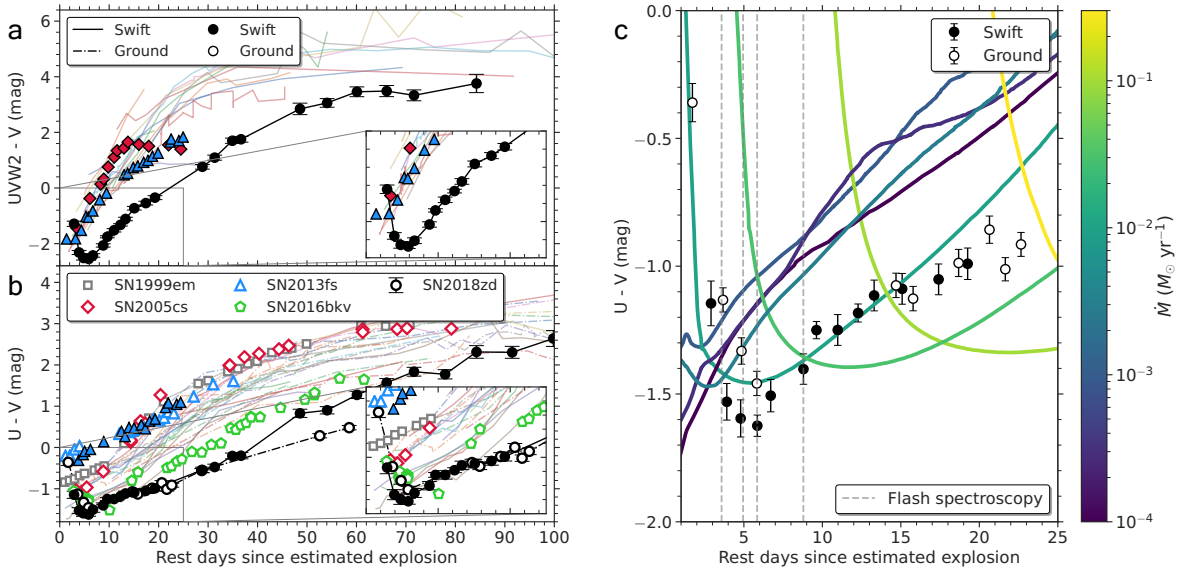
Figure 2.2: **UV colour light curves. a, b,** Comparison of the UV colours of SN 2018zd with the sample as in Fig. 2.1a. The panels show *Swift* $UVW2 - V$ (**a**) and *Swift* and ground-based $U - V$ colour evolution (**b**). Note the pronounced sharp blueward colour evolution of SN 2018zd over the first ~ 5 d, shown in the insets, suggesting a possible delayed shock-breakout through dense CSM. **c,** Comparison of the $U - V$ colour of SN 2018zd with our MESA+STELLA CSM models (§ 2.3.4 and Fig. 2.10) assuming a typical constant wind velocity of $20 \, \mathrm{km \, s^{-1}}$ (Fig. 2.3), colour–coded by the mass-loss rate. To reproduce the observed early blueward evolution, $\dot{M} \approx 0.01 \, M_\odot \, \mathrm{yr^{-1}}$ for the last $\sim 10 \, \mathrm{yr}$ before the explosion is required. The observed flash-spectroscopy epochs (Fig. 2.3) are marked by the vertical dashed lines and are consistent with the blueward colour evolution. Error bars denote 1σ uncertainties.

reaching the minimum in $U - V$ colour (that is, becoming bluer until) ~ 5 d after the explosion (Fig. 2.2), which suggests a possible delayed shock-breakout through dense CSM. In such a case, a photosphere initially forms inside the unshocked optically-thick CSM (Moriya et al. 2018a); this provides an additional power source leading to the bluer colour when the shock front is propagating through the CSM (see Fig. 2.9 for the same effect on the photospheric velocity). Our MESA+STELLA CSM light-curve models (§ 2.3.4 and Fig. 2.10) show that $\dot{M} \approx 0.01 \, M_\odot \, \mathrm{yr^{-1}}$ for the last $\sim 10 \, \mathrm{yr}$ before the explosion is required to reproduce the early-time $U - V$ colour of SN 2018zd, assuming a typical constant $v_{\mathrm{wind}} = 20 \, \mathrm{km \, s^{-1}}$ (Moriya et al. 2014; Fig. 2.2). Since the estimated mass loss

is a few orders of magnitude greater than that expected from SAGB or RSG winds, it is probably dominated by eruptive events (Poelarends et al. 2008; Jones et al. 2013).

Consistent with the possible delayed shock breakout seen in the early UV colour, SN 2018zd exhibits unusually persistent ($\gtrsim 9$ d) flash features, reaching the highest ionisation states at ~ 5 d after the explosion (Fig. 2.3). The strengths of flash features depend on the photospheric temperature, CSM density, and CSM abundance (Yaron et al. 2017; Boian & Groh 2019, 2020). We constrain the photospheric temperature and CSM density of SN 2018zd by the `MESA+STELLA` UV-colour models. Then we use emission-line intensity ratios as diagnostics of CSM abundance by comparing with the flash spectral models of solar-abundance and He-rich atmospheres (Boian & Groh 2019; Fig. 2.3); note that the line ratios are not well reproduced by either solar-abundance or He-rich models alone (Boian & Groh 2020), and a mixture of both with higher density needs to be modelled for a more detailed abundance analysis. On the basis of the model comparisons, we estimate He- C-, and N-rich, but O-poor CSM mass fractions of $X_{\mathrm{He}} \approx 0.3$–$0.8$, $X_{\mathrm{C}} \approx 3 \times 10^{-3}$, $X_{\mathrm{N}} \approx 8 \times 10^{-3}$, and $X_{\mathrm{O}} \approx 10^{-4}$, which is more consistent with an SAGB than an RSG atmosphere (Jones et al. 2013; Doherty et al. 2017).

Since the core composition and explosion nucleosynthesis are different from Fe CCSNe (but see §2.4.6 for some caveats on the low-mass end), ECSNe are expected to show distinct nebular spectral features: stronger Ni than Fe lines due to a more stable ^{58}Ni yield than radioactive ^{56}Ni (a parent nuclide of ^{56}Fe) from the innermost neutron-rich ejecta (electron fraction $Y_e \lesssim 0.49$; Wanajo et al. 2009; Jerkstrand et al. 2018); weak O, Mg, and Fe lines owing to the thin ($\sim 0.01\,M_\odot$) O+C shell, which is further burned to Fe-group elements (Kitaura et al. 2006; Janka et al. 2008); and weak C lines because of the efficient dredge-up/out reducing most of the He-rich layer before the explosion (Poelarends et al. 2008; Jones et al. 2013; Doherty et al. 2017). N lines are hard to be constrained in Type IIP SNe, as [N II] $\lambda\lambda 6548, 6583$ are hidden by strong Hα. For
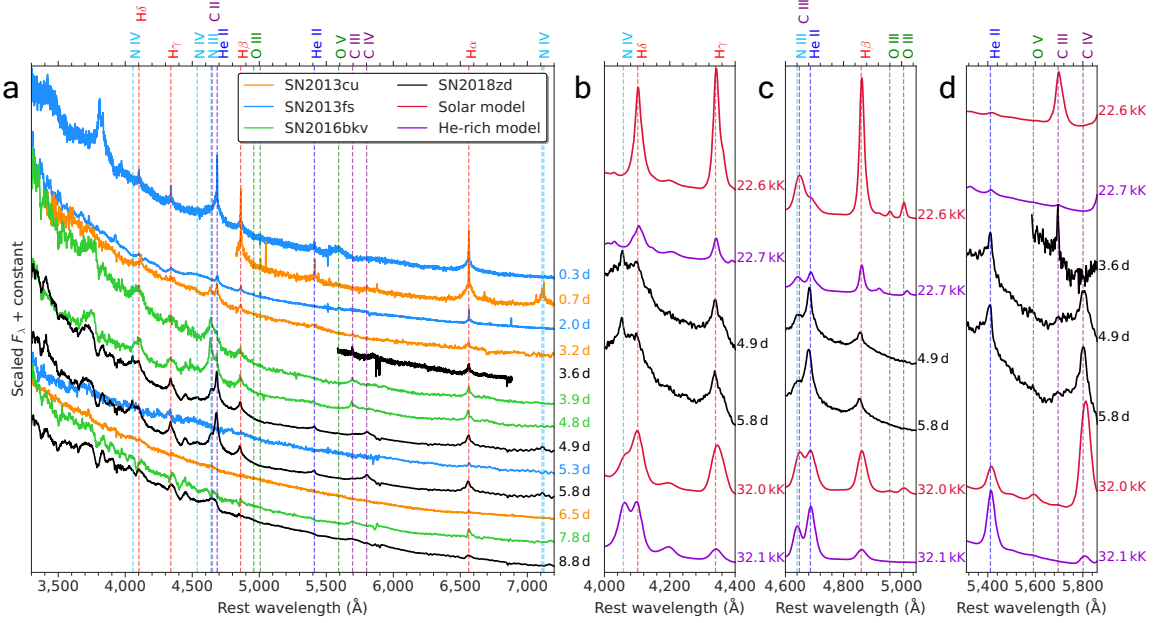
Figure 2.3:   **Flash spectral time series. a,** Comparison of the flash spectral
time series of SN 2018zd with that of well-sampled Type IIP SNe 2013fs (Yaron
et al. 2017) and 2016bkv (Hosseinzadeh et al. 2018), and Type IIb (mostly stripped
H-rich envelope) SN 2013cu (Gal-Yam et al. 2014). SN 2018zd exhibits the persistent
flash features ($\gtrsim$ 9 d), while most of the flash features in the other SNe disappear
within $\sim$ 5 d after the explosion. **b–d,** Comparison of the flash spectral time se-
ries at three different zoomed-in wavelength regions of SN 2018zd with the scaled
and resampled flash spectral models of solar abundance ($X_{\mathrm{H}} = 0.70$, $X_{\mathrm{He}} = 0.28$,
$X_{\mathrm{C}} = 3.02 \times 10^{-3}$, $X_{\mathrm{N}} = 1.18 \times 10^{-3}$, $X_{\mathrm{O}} = 9.63 \times 10^{-3}$) and He-rich ($X_{\mathrm{H}} = 0.18$,
$X_{\mathrm{He}} = 0.80$, $X_{\mathrm{C}} = 5.58 \times 10^{-5}$, $X_{\mathrm{N}} = 8.17 \times 10^{-3}$, $X_{\mathrm{O}} = 1.312 \times 10^{-4}$) atmo-
sphere with $\dot{M}_{\mathrm{mod}} = 3 \times 10^{-3}\,M_{\odot}\,\mathrm{yr}^{-1}$ and $v_{\mathrm{mod}} = 150\,\mathrm{km\,s}^{-1}$ (the densest CSM
with the finest temperature grid spacing; Boian & Groh 2019). The temperatures
are constrained to be within $\sim$ 20,000 K (at 3.6 d) to 30,000 K (at 4.9–5.8 d) from the
`MESA+STELLA` UV-colour models (Fig. 2.2). The observed features are expected to
be narrower and stronger if resolved, as $\rho_{\mathrm{obs}}/\rho_{\mathrm{mod}} = (\dot{M}_{\mathrm{obs}}/v_{\mathrm{obs}})/(\dot{M}_{\mathrm{mod}}/v_{\mathrm{mod}}) = 25$
with $\dot{M}_{\mathrm{obs}} = 0.01\,M_{\odot}\,\mathrm{yr}^{-1}$ from the UV colours and assuming $v_{\mathrm{obs}} = 20\,\mathrm{km\,s}^{-1}$ (the
wind P Cygni components of SN 2018zd are not resolved, only giving an upper-limit
$v_{\mathrm{obs}} < 76.3\,\mathrm{km\,s}^{-1}$ from the highest spectral resolution of C III $\lambda5696$ at 3.6 d). On
the basis of the model comparisons, the line ratios of N IV/Hδ > 1 (**b**) and He II/Hβ
> 1 (**c**), the transition from C III to C IV (**d**), and the lack of O III and O V lines (**c,
d**) observed in SN 2018zd suggest He-, C-, and N-rich, but O-poor CSM composition.

13

low-mass progenitors ($\lesssim 12\,M_\odot$), a low line ratio of [O I]/[Ca II] is expected owing to the low O-core mass (Jerkstrand et al. 2012; Maeda et al. 2007).

True nebular spectral models of ECSNe are difficult to produce, but they can be approximated by removing the He core from an Fe CCSN simulation. Here we use such a model (Jerkstrand et al. 2018), which we call the 'approximate ECSN' model. Comparison of the nebular spectra of SN 2018zd with the $9\,M_\odot$ models (Jerkstrand et al. 2018) favours the approximate ECSN model over the Fe CCSN model, especially through the weak C, O, Mg, and Fe lines (Fig. 2.4). In addition, the low line ratio of [O I] $\lambda\lambda6300$, 6364/[Ca II] $\lambda\lambda7291$, $7323 < 1$ observed in SN 2018zd indicates a low-mass progenitor.

Although quantitative analysis to derive the masses of Ni and Fe requires detailed radiative-transfer simulations, we can obtain a rough estimate of the line ratio expected from ECSNe. For normal Fe CCSNe where Ni and Fe are dominantly produced in the same layer, [Fe II] overwhelms [Ni II] in the emission from the innermost region (Jerkstrand et al. 2012). In ECSN models (Wanajo et al. 2009), however, there is a layer of Ni-rich (neutron-rich) material, emitting predominantly [Ni II], inside the outer mixture of Ni and Fe. In this situation where the Ni-rich and Fe-rich regions are physically separated, [Ni II]/[Fe II] roughly reflects the mass ratio of Ni and Fe in the entire ejecta (Maeda et al. 2007), which is 1.3–3.0 in the ECSN models (Wanajo et al. 2009). The observed [Ni II] $\lambda7378$/[Fe II] $\lambda7155$ ratio of 1.3–1.6 in SN 2018zd (Fig. 2.4) is indeed within the expected range. In principle, clumping, fluorescence, and/or shock excitation could enhance [Ni II] $\lambda7378$ such that [Ni II] $\lambda7378$/[Fe II] $\lambda7155$ overestimates the Ni/Fe mass ratio (Hudgins et al. 1990), but we leave a detailed theoretical study to future works.

SN 2018zd fulfills the expected characteristics and is strong evidence for the existence of ECSNe and their progenitor SAGB stars (see § 2.4.7 and Fig. 2.11 for other previously suggested ECSN candidates). With SN 2018zd, we roughly estimate an ECSN rate of
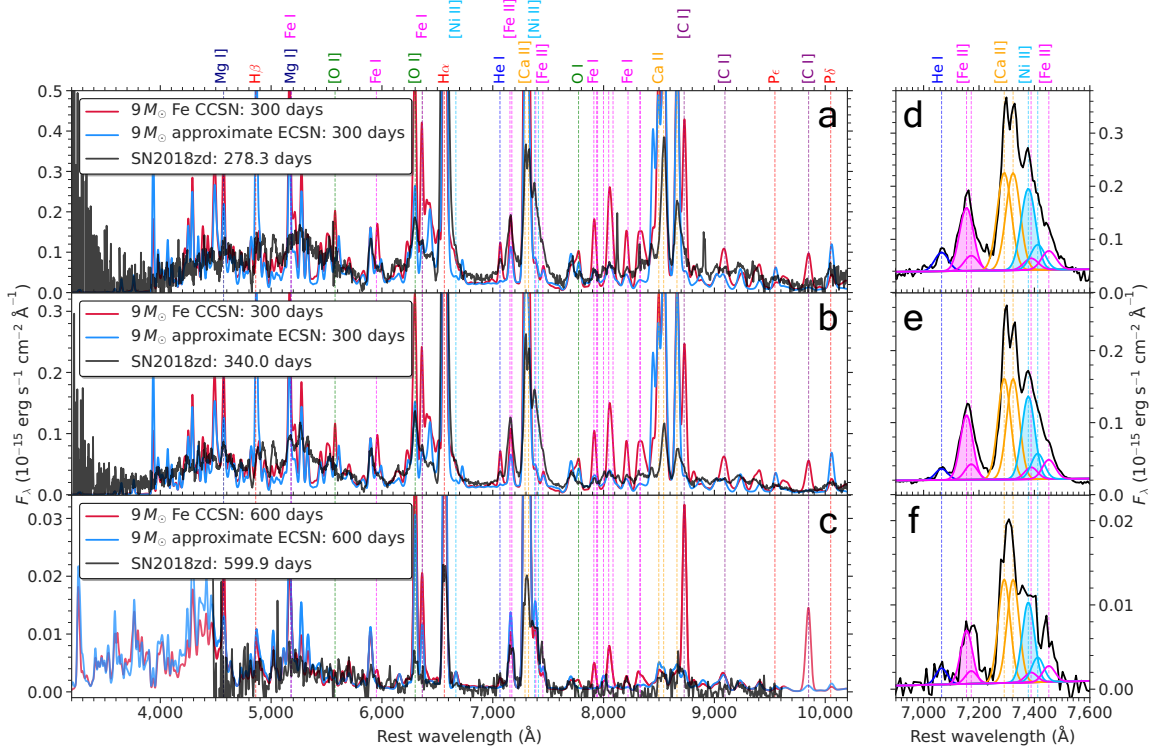
Figure 2.4:   **Nebular spectral time series. a–c,** Comparison of the nebular spectral time series at three different epochs of SN 2018zd with the scaled (by ^{56}Ni mass and phase) and resampled $9\,M_\odot$ Fe CCSN and 'approximate ECSN' (excluding the He-core composition from the Fe CCSN) models (Jerkstrand et al. 2018). The large number of narrow lines at $\lesssim 5500\,\text{Å}$ and strong Ca lines in the models are known issues. The weak [Ni II] lines in the models are from the primordial Ni (solar abundance), as Ni nucleosynthesis is not taken into account. In ascending order of wavelength, note the weak Mg I] $\lambda4571$, Mg I] $\lambda5180$ + Fe I $\lambda5180$, [O I] $\lambda5577$, Fe I $\lambda5950$, [O I] $\lambda\lambda6300, 6364$ + Fe I $\lambda6364$, O I $\lambda7774$, Fe I cluster 7,900–8,500 Å, [C I] $\lambda8727$, [C I] $\lambda9100$, and [C I] $\lambda9850$, as well as the low line ratio of [O I] $\lambda\lambda6300$, 6364/[Ca II] $\lambda\lambda7291, 7323 < 1$ observed in SN 2018zd. He I $\lambda7065$ is weaker in the approximate ECSN model than in the observed spectra; the emission from the dredged-up/out elements (for example, He and N) in the H-rich envelope may be underestimated by the model. **d–f,** Simultaneous Gaussian fits to He I $\lambda7065$, [Fe II] $\lambda7155$, [Fe II] $\lambda7172$, [Ca II] $\lambda7291$, [Ca II] $\lambda7323$, [Ni II] $\lambda7378$, [Fe II] $\lambda7388$, [Ni II] $\lambda7412$, and [Fe II] $\lambda7452$ (§ 2.4.2) at three different epochs. Note the stronger [Ni II] $\lambda7378$ (the blue shaded region) than [Fe II] $\lambda7155$ (the pink shaded region), yielding [Ni II]/[Fe II] = 1.3–1.6. The weak C, O, Mg, and Fe lines combined with the strong Ni lines observed in SN 2018zd are consistent with the ECSN chemical composition and nucleosynthesis.

15

0.6–8.5% of all CCSNe, corresponding to a narrow SAGB progenitor mass window of $\Delta M_{\mathrm{SAGB}} \approx 0.06$–$0.69\,M_\odot$ (§ 2.3.5 and Fig. 2.12). Theoretically, the evolutionary path to SAGB stars is uncertain owing to the high sensitivity of nuclear burning on complex dredge-up/out and mass-loss mechanisms (Doherty et al. 2017; Jones et al. 2013), giving a variety of expected mass windows at different metallicities (for example, $\Delta M_{\mathrm{SAGB}} \approx 0.2$–$1.4\,M_\odot$ at solar metallicity; Poelarends et al. 2008). Their final fate may vary from core-collapse to thermonuclear ECSNe depending on the electron-capture rates and oxygen flame speed in the degenerate core (Zha et al. 2019; Leung et al. 2020), resulting in different nucleosynthetic yields and galactic chemical evolution (Jones et al. 2019). The core-collapse ECSNe are expected to leave low mass, spin, and kick-velocity neutron stars (Gessner & Janka 2018), forming a low-mass peak ($\sim 1.25\,M_\odot$) in neutron star mass distribution (Schwab et al. 2010) and low-eccentricity (~ 0.2) gravitational wave source population (Giacobbo & Mapelli 2019). Therefore, using SN 2018zd as an ECSN template, future statistical studies with homogeneous samples from large surveys will be able to further reveal the evolution of SAGB progenitors and the influence of ECSNe on the kinetic and chemical composition of the Universe.

2.3   Methods

2.3.1   Extinction

We obtained the Milky Way (MW) extinction (Schlafly & Finkbeiner 2011) of $A_{V,\mathrm{MW}} = 0.258\,$mag via the NASA/Infrared Processing and Analysis Center (IPAC) Infrared Science Archive. We measure the total Na I D EW of each host and MW component using the MMT Blue Channel spectra (moderate resolution of $1.45\,\text{Å}$) taken 3.6–53.4 d after the explosion (Fig. 2.8). Since the ratio of the total Na I D EW of the host to MW varies

between 1.07 and 1.25, we estimate $A_{V,\mathrm{host}} \gtrsim A_{V,\mathrm{MW}}$. As a cross-check, we transform the *gri* magnitudes of SN 2018zd to *VRI* magnitudes (Jester et al. 2005) and compare the $V - I$ colour to that of well-observed, low-extinction Type IIP SNe 1999em (Leonard et al. 2002b), 1999gi (Leonard et al. 2002a), and 2017eaw (Van Dyk et al. 2019) by assuming $A_{V,\mathrm{host}} = A_{V,\mathrm{MW}}$ for SN 2018zd. Since the $V - I$ colour of SN 2018zd during the photospheric phase is consistent with the other SNe, we adopt a host extinction of $A_{V,\mathrm{host}} = A_{V,\mathrm{MW}}$ and assume a reddening law (Fitzpatrick 1999) with $R_V = 3.1$. This extinction value is also consistent with the lower limit obtained from the spectropolarimetry (§ 2.4.3). Increasing (or decreasing) the host extinction by more than $0.10\,\mathrm{mag}$ makes the $V - I$ colour inconsistent with that of the other Type IIP SNe. Thus, we adopt a host extinction uncertainty of $\pm 0.10\,\mathrm{mag}$.

2.3.2   Luminosity Distance

We apply the expanding photosphere method (EPM; Leonard et al. 2002a; Dessart & Hillier 2005) and the standard candle method (SCM; Polshaw et al. 2015) using the measured Fe II $\lambda 5169$ velocities and transforming the *gri* to *VRI* magnitudes (Jester et al. 2005), which yields 6.5 ± 0.7 and $9.6 \pm 1.0\,\mathrm{Mpc}$, respectively. The EPM is best used at early times ($\lesssim 30\,\mathrm{d}$) when SN emission can be approximated as a diluted blackbody in free expansion (Dessart & Hillier 2005). However, the early emission from SN 2018zd is dominated by CSM interaction (Figs. 2.2 & 2.9), making the EPM unreliable. On the other hand, the SCM is based on the luminosity–velocity correlation (Hamuy & Pinto 2002; Kasen & Woosley 2009; Goldberg et al. 2019) at day 50 when the CSM interaction is negligible, which is well reproduced by our MESA+STELLA models (§ 2.3.4 and Fig. 2.10). Thus, we favour the SCM over the EPM.

It has been suggested that NGC 2146 may be farther away than the SCM estimate.

There is a claim of a preliminary tip of the red giant branch (TRGB) distance obtained from archival *HST* Wide Field Camera 3 infrared channel (WFC3/IR) data (program GO-12206, principal investigator: M. Westmoquette) that places the galaxy out at $\sim$ 18 Mpc (Adamo et al. 2012). We have independently reduced and analysed these same data and find that the single orbit of observations available (split between F110W and F160W) does not reach the necessary depths to make this conclusion. Even at the closer 10 Mpc distance, the archival data would not allow us to obtain a TRGB measurement owing to the short exposure times and intense levels of crowding. We also find that there are no archival *HST* optical data of sufficient depths to obtain a TRGB measurement.

Future SN-independent distance measurements (for example, Cepheids and TRGB with *HST*) will be necessary to verify the SCM estimate. We discuss the implications if the luminosity distance were larger than the SCM estimate in §2.4.6.

2.3.3   *HST* and *Spitzer* Progenitor Detection and Upper Limits

We were able to locate astrometrically the site of SN 2018zd in existing pre-explosion *HST* archival images, specifically data obtained in bands F814W and F658N with the Advanced Camera for Surveys (ACS)/WFC instrument on 2004 April 10 (program GO-9788, principal investigator L. Ho, with total exposure times of 120 s and 700 s, respectively; the F814W image consists of a single exposure), as well as in F225W with WFC3/UVIS on 2013 March 7 (program GO-13007, principal investigator L. Armus; total exposure time of 1500 s). We identified a potential candidate progenitor precisely by obtaining images of the SN itself on 2019 May 19 in F555W and F814W with WFC3/UVIS, as part of program GO-15151 (principal investigator S. Van Dyk). We were able to astrometrically register the 2019 F814W image mosaic to the 2004 one using 23 stars in common, with a root-mean-square uncertainty of 0.14 ACS/WFC pixel. Furthermore, in a similar fashion

we were able to match precisely the SN image with the F658N and F225W images as well; however, the progenitor candidate was not detected in either of those bands. We show the pre- and post-explosion images in Fig. 2.5.

We extracted photometry from all of the *HST* images using the package Dolphot (Dolphin 2016). We found that Dolphot detected and measured a source at the position of the progenitor candidate with $m_{\mathrm{F814W}} = 25.05 \pm 0.15 \, \mathrm{mag}$. Unfortunately, as noted above, the F814W pre-explosion observation consisted of only a single exposure, so it was not possible for the standard STScI pipeline to reject cosmic-ray hits in the usual way, while constructing an image mosaic from the single frame, as would normally be the case for two or more dithered exposures. In addition, we note that the flux measurement with Dolphot may be affected by the presence of cosmic-ray hits in the image at or around the progenitor site. Nevertheless, the values of both the Dolphot output parameters 'object type' (1) and 'sharpness' (-0.013) appear to point to the source being stellar-like.

To determine whether the peak pixel seen at the candidate location is indeed merely a cosmic-ray hit or is the actual peak of a stellar point-spread function (PSF), we employ a deep-learning model (C.X. et al., manuscript in preparation) based on the results from DeepCR (Zhang & Bloom 2020). We find that no pixels in the vicinity of the candidate progenitor have a model score higher than 5.1×10^{-5}. If we use this score as a threshold, the model has a completeness of 99.93% based on the test data taken with the same instrument. We therefore conclude that progenitor candidate is a real PSF with $> 3\sigma$ confidence. If the object was not actually detected, we find that the upper limit at 3σ to detection in F814W is > 26.3 mag.

Inserting and recovering an artificial star of varying brightness at the exact SN position with Dolphot in both F225W and F658N led to estimates of the upper limits to detection (at 3σ) of > 23.6 and $> 24.1 \, \mathrm{mag}$, respectively. In addition, note that we measured a brightness of the SN itself in the 2019 *HST* observations of $m_{\mathrm{F555W}} = 21.53 \pm 0.01$

and $m_{\mathrm{F814W}} = 20.33 \pm 0.01\,\mathrm{mag}$.

The SN site also can be found in pre-explosion *Spitzer* data both from the cryogenic and so-called warm (post-cryogenic) missions, from $3.6\,\mu$m to $24\,\mu$m. The data are from observations with the Infrared Array Camera (IRAC; Fazio et al. 2004) in channels 1 ($3.6\,\mu$m) and 2 ($4.5\,\mu$m; the SN site sits in a gap of spatial coverage in channels 3 and 4 at $5.8\,\mu$m and $8\,\mu$m, respectively) on 2004 March 8 (program 59, principal investigator G. Rieke) and on 2007 October 16 (program 40410, principal investigator G. Rieke) in channels 2 and 4; from observations with the Multiband Imaging Photometer for Spitzer (MIPS; Rieke et al. 2004) at $24\,\mu$m on 2004 March 16 (program 59, principal investigator G. Rieke; the sensitivity and resolution of the data at $70\,\mu$m and $160\,\mu$m are not sufficient to hope to detect the progenitor and were not considered further); and from observations with IRAC in channels 1 and 2 on 2011 November 15 (program 80089, principal investigator D. Sanders). We show the 2011 November 15 IRAC observation in channel 1 in Fig. 2.5.

Observations with IRAC of the SN itself were obtained on 2019 January 24 (program 14098, principal investigator O. Fox); however, we did not analyse these data, other than to extract an absolute position for the SN of $\alpha = 6^{\mathrm{h}}18^{\mathrm{m}}03.43^{\mathrm{s}}$, $\delta = +78°22'01\rlap{.}''4$ (J2000; $\pm 0\rlap{.}''3$ in each coordinate). Using MOPEX (Makovoz et al. 2006) we constructed mosaics from all of the useful pre-SN imaging data, and with APEX within MOPEX (Makovoz & Marleau 2005) we inserted into the images an artificial star of varying brightness at this absolute position. From this, we estimated upper limits to detection of the progenitor (at 3σ) of > 19.0 and $> 18.1\,\mathrm{mag}$ in channels 1 and 2 (respectively) from the 2004 March 8 data; > 18.1 and $> 14.5\,\mathrm{mag}$ in channels 2 and 4 (respectively) from 2007 October 16; and > 19.0 and $> 18.4\,\mathrm{mag}$ in channels 1 and 2 (respectively) from 2011 November 15 (we have assumed the zeropoints from the IRAC Instrument Handbook). We also estimated $> 10.2\,\mathrm{mag}$ at $24\,\mu$m from the 2004 March 16 observation (we have assumed

the zeropoint from the MIPS Instrument Handbook).

We show the resulting spectral energy distribution (SED), or limits thereon, for the SN 2018zd progenitor in Fig. 2.6. The distance ($9.6 \pm 1.0 \, \mathrm{Mpc}$) and extinction ($A_V = 0.52 \pm 0.10 \, \mathrm{mag}$) to the SN were adopted (§ 2.3.2 & 2.3.1), assuming that the latter also applied to the progenitor as well. We have further assumed a reddening law (Fitzpatrick 1999) with $R_V = 3.1$ and extended it into the MIR (Xue et al. 2016). For comparison, we also show single-star SAGB and RSG (with respective initial masses $M_{\mathrm{init}} = 8$ and $15 \, M_\odot$) models from BPASS v2.2 (Stanway & Eldridge 2018) with metallicities $Z = 0.020$ (solar) and $Z = 0.010$ (subsolar; as discussed in § 2.4.5, the SN site metallicity is probably subsolar). We have further included for comparison the observed SED for the candidate SAGB star MSX SMC 055 (IRAS 00483−7347; Groenewegen & Sloan 2018) as well as the SED for the progenitor of the low-luminosity Type IIP SN 2005cs (Maund et al. 2005; Li et al. 2006).

We note that the SEDs for the BPASS RSG models with $M_{\mathrm{init}} = 15 \, M_\odot$ are probably not realistic, since they are merely bare photospheres, whereas we would expect such a star to possess a dusty CSM, as was the case for the progenitor of SN 2017eaw (Van Dyk et al. 2019). The same could also potentially be said for the SAGB models, given the dusty nature of MSX SMC 055. Again, these BPASS model SEDs are bare photospheres and do not include CSM, for the presence of which we have strong evidence (given here) in the case of the SN 2018zd progenitor; this merits further development of the SED models including the effect of dusty CSM.

It is difficult to infer much about the nature of the SN 2018zd progenitor, based on a probable detection in one band and upper limits in the others. However, its inferred SED does appear to be less consistent with that of an $M_{\mathrm{init}} \gtrsim 8 \, M_\odot$ RSG star, as well as the SN 2005cs progenitor, and more consistent with a potentially dusty SAGB star, such as MSX SMC 055. If there were circumstellar dust around the SN 2018zd progenitor, it

21

was destroyed as the SN shock progressed through.

We should revisit this site either with *HST* or the *James Webb Space Telescope* in a bandpass similar to F814W, when the SN has sufficiently faded, to confirm that the candidate object was indeed the progenitor. Again, we cannot entirely rule out that the source detected in the pre-SN image at the precise SN position is not related to a cosmic-ray hit; however, all of the indications suggest this is a real detected star, which should have vanished when the SN site is observed at a sufficiently late time.

2.3.4   MESA+STELLA **Progenitor and Light-Curve Models**

Recent work (Goldberg et al. 2019; Dessart & Hillier 2019; Bersten et al. 2011; Martinez & Bersten 2019) has highlighted the non-uniqueness of bolometric light-curve modeling for extracting explosion characteristics (ejecta mass M_{ej}, explosion energy E_{exp}, and progenitor radius R) from plateau features (in particular, luminosity at day 50, L_{50}, and plateau duration, t_p) without an independent prior on one of M_{ej}, E_{exp}, or R. Owing to the presumed presence of dense CSM and its potential influence on the early light curves and velocities, shock-cooling modeling and early expansion velocities cannot simply lift this degeneracy.

To allow light-curve analysis to be agnostic to the progenitor mass, three different explosion models were created with equally good by-eye matches to the bolometric light curve and expansion-velocity data on the plateau. The progenitor models were selected from a pre-existing grid (Goldberg & Bildsten 2020) of MESA RSG progenitor models with expected ejecta masses and radii within the family of explosions consistent with the L_{50}, t_p, and M_{Ni} of SN 2018zd (Fig. 2.10; see § 2.4.4 for the model details).

The explosion energies for each model were then chosen and adjusted to match the light curve of SN 2018zd with the respective progenitor model radii using the degeneracy

relations (Goldberg et al. 2019)

$$\log(E_{51}) = -0.728 + 2.148\log(L_{\mathrm{p},42}) - 0.280\log(M_{\mathrm{Ni}}) + 2.091\log(t_{\mathrm{p},2}) - 1.632\log(R_{500}),$$

$$\log(M_{10}) = -0.947 + 1.474\log(L_{\mathrm{p},42}) - 0.518\log(M_{\mathrm{Ni}}) + 3.867\log(t_{\mathrm{p},2}) - 1.120\log(R_{500}),$$

$$(2.1)$$

where $E_{51} = E_{\mathrm{exp}}/10^{51}\,\mathrm{erg}$, $M_{10} = M_{\mathrm{ej}}/10\,M_\odot$, M_{Ni} is in units of $M_\odot$, $L_{\mathrm{p},42} = L_{50}/10^{42}$ $\mathrm{erg\,s}^{-1}$, $t_{\mathrm{p},2} = t_{\mathrm{p}}/100\,\mathrm{d}$, and $R_{500} = R/500\,R_\odot$. Plugging in $L_{50} = 8.6 \times 10^{41}\,\mathrm{erg\,s}^{-1}$ from the bolometric light curve at day 50, $t_{\mathrm{p}} = 125.4\,\mathrm{d}$ determined by fitting the drop from the plateau (Valenti et al. 2016), and observed $M_{\mathrm{Ni}} = 0.0086\,M_\odot$, these relations describe the possible explosion parameter space (Fig. 2.10). They are intended for Ni-rich ($M_{\mathrm{Ni}} > 0.03\,M_\odot$) Type IIP SNe of RSG progenitors with no fallback, but nonetheless provide a heuristic estimate for the degeneracy between explosion energy, progenitor radius, and ejected mass.

This degeneracy motivates the set of progenitor models and explosion energies that we use to reproduce the light-curve properties, and reveals low recovered E_{exp} which overlap substantially with the expected parameter space of ECSNe. The mapping between M_{ej} recovered for Fe CCSNe and ECSNe is less robust, as differences in mixing extent and H/He abundances could account for differences in the recovered M_{ej} from explosions of different stellar progenitors (Kasen & Woosley 2009; Kozyreva et al. 2019; Goldberg et al. 2019). As seen in Fig. 2.10, even though SN 2018zd is not particularly dim, low-energy explosions of radially extended progenitors can match the plateau luminosity. A slightly lower-M_{ej} progenitor with a radius of $1,400\,R_\odot$, for example, could even produce this luminosity with an explosion energy of $\sim 1.5 \times 10^{50}\,\mathrm{erg}$.

The explosions were carried out using `MESA` until near shock breakout. The models were then handed off to `STELLA` to produce synthetic bolometric light curves and expansion velocities (Fig. 2.10; see §2.4.4 for the modeling details). We see good agreement

between all three models and observations (varying by at least 50% in M_{ej}, E_{exp}, and R), with deviations at early times that can be attributed to the extended stellar atmosphere and potential interaction with the circumstellar environment.

To account for the early deviations, we affix a wind-density profile with $\rho_{\mathrm{wind}}(r) = \dot{M}_{\mathrm{wind}}/4\pi r^2 v_{\mathrm{wind}}$, where r is the radial extent, $\dot{M}_{\mathrm{wind}}$ is a constant wind mass-loss rate, and v_{wind} is the wind velocity for time t_{wind} (that is, $M_{\mathrm{wind}} = \dot{M}_{\mathrm{wind}} t_{\mathrm{wind}}$), onto the MESA model at handoff to STELLA. We construct a grid of CSM models by varying the following parameters: $\dot{M}_{\mathrm{wind}} = \{10^{-4}, 3 \times 10^{-4}, 10^{-3}, 3 \times 10^{-3}, 10^{-2}, 3 \times 10^{-2}, 10^{-1}, 3 \times 10^{-1}\}\, M_\odot\,\mathrm{yr}^{-1}$ and $t_{\mathrm{wind}} = \{1, 3, 10, 30\}\,\mathrm{yr}$ for each MESA model, assuming a typical wind velocity $v_{\mathrm{wind}} = 20\,\mathrm{km\,s}^{-1}$ (Moriya et al. 2014). Then we perform χ^2 fitting on the observed bolometric light curve over the full temporal evolution and find the best-fit parameters $\dot{M}_{\mathrm{wind}} = 0.01\, M_\odot\,\mathrm{yr}^{-1}$ and $t_{\mathrm{wind}} = 10\,\mathrm{yr}$.

Remarkably, the best-fit parameters are the same for all three degenerate models, and also reproduce the early blueward UV-colour evolution (Fig. 2.10). Thus, we choose model M8.3_R1035_E0.23 (§ 2.4.4) as being representative and present it for the UV-colour plot in Fig. 2.2. In addition to matching the early-time luminosity excess, a dense wind profile suppresses the early photospheric and Fe line velocities (Moriya et al. 2018 a). The kink seen in the modelled Fe line velocity with Sobolev optical depth $\tau_{\mathrm{Sob}} = 1$ in the STELLA models can be attributed to numerics at the boundary between the CSM profile and the surface of the stellar ejecta (Fig. 2.10). Overall, the models still yield general agreement between the calculated velocity evolution and the data.

We note that at 3–10 d after the explosion, the blackbody temperatures ($\sim$ 20,000–25,000 K) may be underestimated (§ 2.4.1), which could affect the luminosity around the peak, and so the CSM models as well. For the flash spectral model comparisons in Fig. 2.3, we use a conservative temperature constraint of $\sim$ 20,000–30,000 K.

2.3.5 The Rate of ECSNe

Among other previously suggested ECSN candidates (§ 2.4.7 and Fig. 2.11), Type IIn-P SNe share similar properties to SN 2018zd. Thus, the Type IIn-P SN rate may be related to the ECSN rate. As there is no rate estimation for Type IIn-P SNe in the literature to our knowledge, we put a rough lower limit using publicly announced Type IIn SNe on the Weizmann Interactive Supernova Data Repository (WISeREP; Yaron & Gal-Yam 2012) and/or the Transient Name Server (TNS) by cross-checking with the literature and the Open Supernova Catalog (Guillochon et al. 2017), and also cross-correlating the public spectra to SN spectral libraries Superfit (Howell et al. 2005) and SNID (Blondin & Tonry 2007) when available. There are 528 objects classified as Type IIn SNe on WISeREP and/or TNS (as of 2020 March 11). We exclude 73 objects as misclassified early-flash Type II SNe, Type Ia-CSM SNe, Type Ibn SNe, SN imposters, or active galactic nuclei. Although 241 objects do not have enough public and/or published spectra and/or light curves to secure the Type IIn classifications and/or to be identified as Type IIn-P SNe, we include them in the further analysis so as not to overestimate the lower limit when taking a number ratio of Type IIn-P to Type IIn SNe (see below and Fig. 2.13).

To identify Type IIn-P SN candidates from the 455 objects, we apply two light-curve criteria based on the known Type IIn-P SN characteristics: (1) the V, r/R, or i/I-band decline of less than 2 mag in the first 50 d after the explosion; and (2) the V, r/R, or i/I-band drop of more than 2 mag in 30 d within 100–150 d after the explosion. This yields four Type IIn-P SN candidates: SNe 2005cl ($z = 0.025878$; Kiewe et al. 2012), 2005db ($z = 0.015124$: Kiewe et al. 2012), 2006bo ($z = 0.0153$; Taddia et al. 2013), and 2011A ($z = 0.008916$; de Jaeger et al. 2015). In addition, there are three known Type IIn-P SNe: 1994W ($z = 0.004116$; Sollerman et al. 1998), 2009kn ($z = 0.015798$;

Kankare et al. 2012), and 2011ht ($z = 0.003646$; Mauerhan et al. 2013) (Fig. 2.13).

To compare with the volume-limited ($\leq 60\,\mathrm{Mpc}$) Lick Observatory Supernova Search (LOSS) sample (Smith et al. 2011a), we apply the same distance cut, leaving 42 Type IIn SNe (17 and 25 with sufficient and insufficient data, respectively) and 3 Type IIn-P SNe (SNe 1994W, 2011A, and 2011ht). As these SNe were discovered by different surveys with different strategies, we have no handle on the incompleteness (but also see Fig. 2.13). Thus, we neglect the incompleteness and take the number ratio of Type IIn-P to Type IIn SNe within $60\,\mathrm{Mpc}$ multiplied by the LOSS Type IIn SN rate (Smith et al. 2011a), $3/42 \times 8.8\% = 0.63\%$ of all CCSNe, as a rough lower limit of the Type IIn-P SN rate.

The identification of SN 2018zd-like SNe from Type IIP SNe (48.2% of all CCSNe) requires not only the light-curve morphology, but also the early UV colours and the flash and nebular spectroscopy, all of which combined are rarely available on WISeREP, TNS, and/or the Open Supernova Catalog. This current sample limitation may indicate that many SN 2018zd-like SNe have been overlooked as normal Type IIP SNe. Given the limitation, we simply take the lowest possible limit of $> 0\%$ with the one identification of SN 2018zd as an ECSN.

By combining the estimated Type IIn-P and SN 2018zd-like lower limits, we obtain a Type IIn-P + SN 2018zd-like lower limit of $> 0.6\%$ of all CCSNe. From the nucleosynthetic point of view, ECSNe are expected to constitute $\lesssim 8.5\%$ of all CCSNe (Wanajo et al. 2018). With the above estimates, the ECSN rate can be roughly constrained within 0.6–8.5% of all CCSNe, which corresponds to a narrow SAGB progenitor mass window of $\Delta M_{\mathrm{SAGB}} \approx 0.06$–$0.69\,M_\odot$ assuming maximum and minimum SAGB masses of $9.25\,M_\odot$ and $9.25\,M_\odot - \Delta M_{\mathrm{SAGB}}$ (respectively) at solar metallicity (Poelarends et al. 2008; Fig. 2.12). We note that the Type IIn-P and SN 2018zd-like rates are probably metallicity dependent (as is the SAGB mass window), but we defer more detailed analysis with a homogeneous sample in the future when one becomes publicly available.
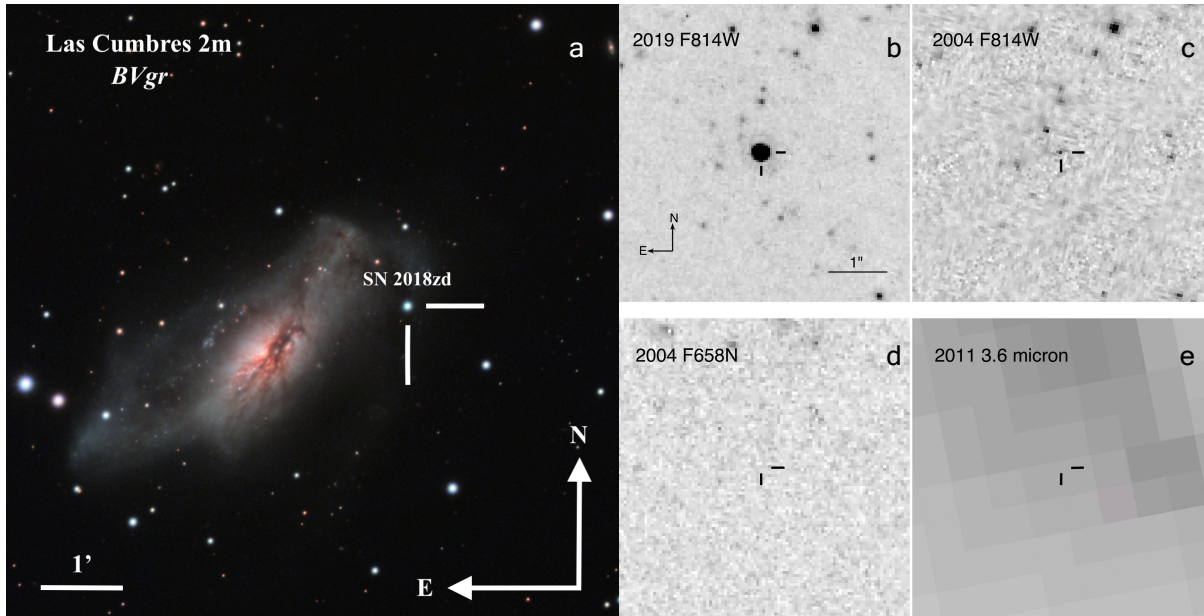
Figure 2.5:   **The host galaxy and post- and pre-explosion images of SN 2018zd. a,** LCO 2 m *BVgr*-composite image of SN 2018zd and the host starburst galaxy NGC 2146 (§ 2.4.5), courtesy of Peter Iláš. At the assumed luminosity distance of 9.6 Mpc, $1'$ corresponds to 2.8 kpc. SN 2018zd is on a tidal stream which was probably ejected during a galaxy merger event. **b,** Portion of an *HST* WFC3/UVIS F814W mosaic obtained on 2019 May 19, 443.7 d after the explosion of SN 2018zd (indicated by the tick marks). **c,** Portion of an *HST* ACS/WFC F814W mosaic from 2004 April 10; the SN site is similarly indicated by tick marks. This mosaic consists of a single exposure, so to remove a number of cosmic-ray hits in the image, we use a masked mean filter to smooth any pixels that have a score of 0.001 or higher from our deep-learning model (§ 2.3.3). The pixels associated with the progenitor candidate had scores $< 4 \times 10^{-5}$, so are not affected. **d,** Same as panel (**c**), but with F658N on the same epoch. **e,** Portion of a *Spitzer* IRAC 3.6 μm mosaic obtained on 2011 November 15, with the SN site again indicated by tick marks. All panels (**b**)–(**e**) are shown to the same scale and orientation, with north up and east to the left. The progenitor candidate is identified only in the single *HST* ACS/WFC F814W image (**c**).
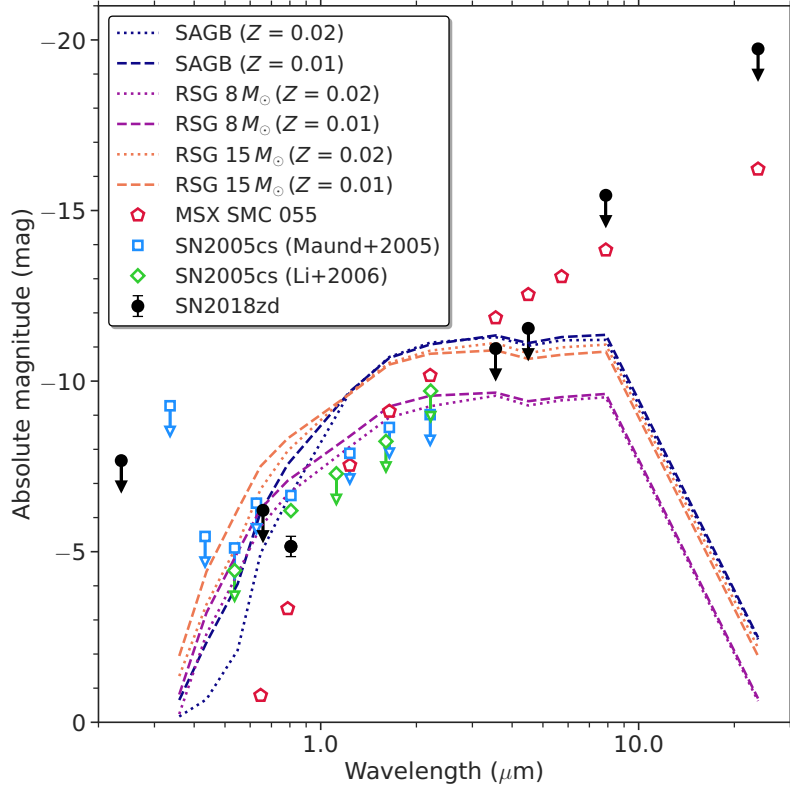
Figure 2.6:   **SN progenitor and SAGB candidate SEDs.**   The SED for the SN 2018zd progenitor candidate resulting from pre-explosion *HST* and *Spitzer* archival data (§ 2.3.3; black solid circles). For comparison we show model SEDs from BPASS v2.2 (Stanway & Eldridge 2018) for SAGB stars (in the initial mass range $M_{init} = 6–8\,M_\odot$ with bolometric luminosities $L \approx 10^5\,L_\odot$ in the last model timestep; navy curves) and RSG stars at $M_{init} = 8\,M_\odot$ (purple curves) and $M_{init} = 15\,M_\odot$ (orange curves), at metallicities $Z = 0.02$ (solar; short-dashed line) and $Z = 0.01$ (subsolar; long-dashed line). The SEDs of the BPASS models are extrapolated into the MIR via MARCS (Gustafsson et al. 2008) model stellar atmospheres of similar temperatures as the last BPASS model timesteps, deriving synthetic photometry from those atmosphere models using the bandpass throughputs provided in the *Spitzer* IRAC and MIPS Instrument Handbooks. Also shown for comparison are the SEDs for the SAGB candidate MSX SMC 055 (assuming Galactic foreground extinction and adjusted to a Small Magellanic Cloud distance modulus of $\mu = 18.90\,\mathrm{mag}$ from the Extragalactic Distance Database (Tully et al. 2009); red open pentagons (Groenewegen & Sloan 2018)) and for the progenitor of the low-luminosity Type IIP SN 2005cs (assuming the total reddening from the two studies (Maund et al. 2005; Li et al. 2006) and adjusted to a recent accurate distance for M51 (McQuinn et al. 2016); blue open squares (Maund et al. 2005), green open diamonds (Li et al. 2006)). The luminosity of the *HST* ACS/WFC F814W detection of the SN 2018zd progenitor candidate lies between MSX SMC 055 and the SN 2005cs progenitor.
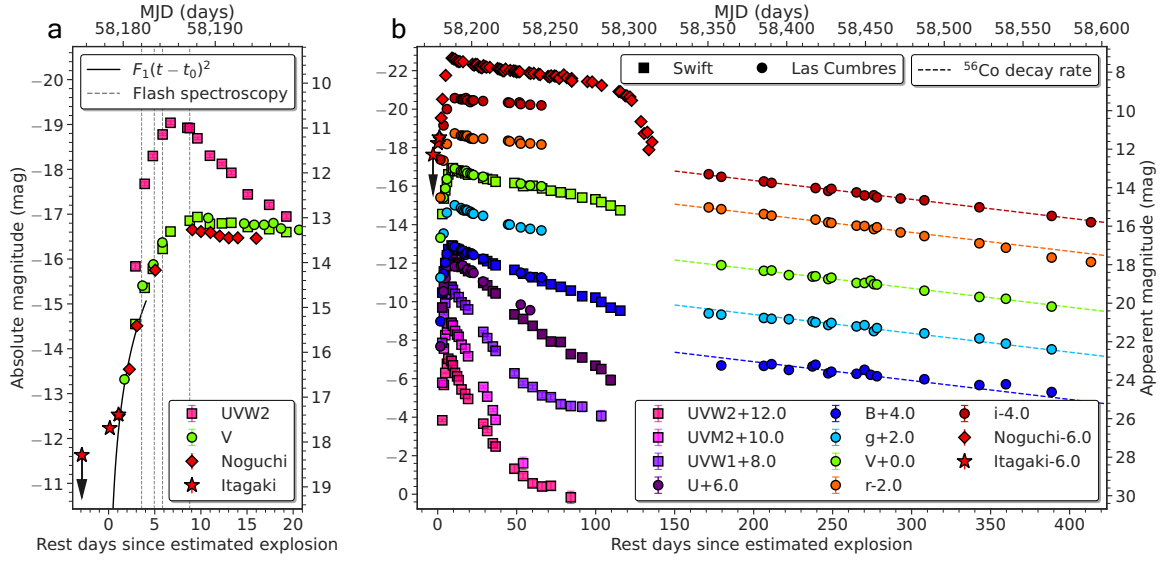
28

Figure 2.7: **Multiband light curve of SN 2018zd. a,** Multiband light curve of SN 2018zd focusing on the early rise. A quadratic function $F_1(t - t_0)^2$ is fitted to the unfiltered optical Itagaki and the first three Noguchi points to estimate an explosion epoch $t_0 = \mathrm{MJD}\,58178.4 \pm 0.1$ (§ 2.4.1). The observed flash-spectroscopy epochs (Fig. 2.8) are marked by the vertical dashed lines. Note the sharper rise in the *Swift UVW*2 than in the *V* and unfiltered photometry during the flash-spectroscopy epochs. **b,** Multiband light curve of SN 2018zd up to the ^{56}Co decay tail. The data gap is due to the Sun constraint. Error bars denote 1σ uncertainties and are sometimes smaller than the marker size. The light-curve shape resembles that of a typical Type IIP SN. Comparing the luminosity on the tail to that of SN 1987A (Hamuy 2003), we estimate a ^{56}Ni mass of $(8.6 \pm 0.5) \times 10^{-3}\,M_\odot$ at the assumed luminosity distance of 9.6 Mpc.
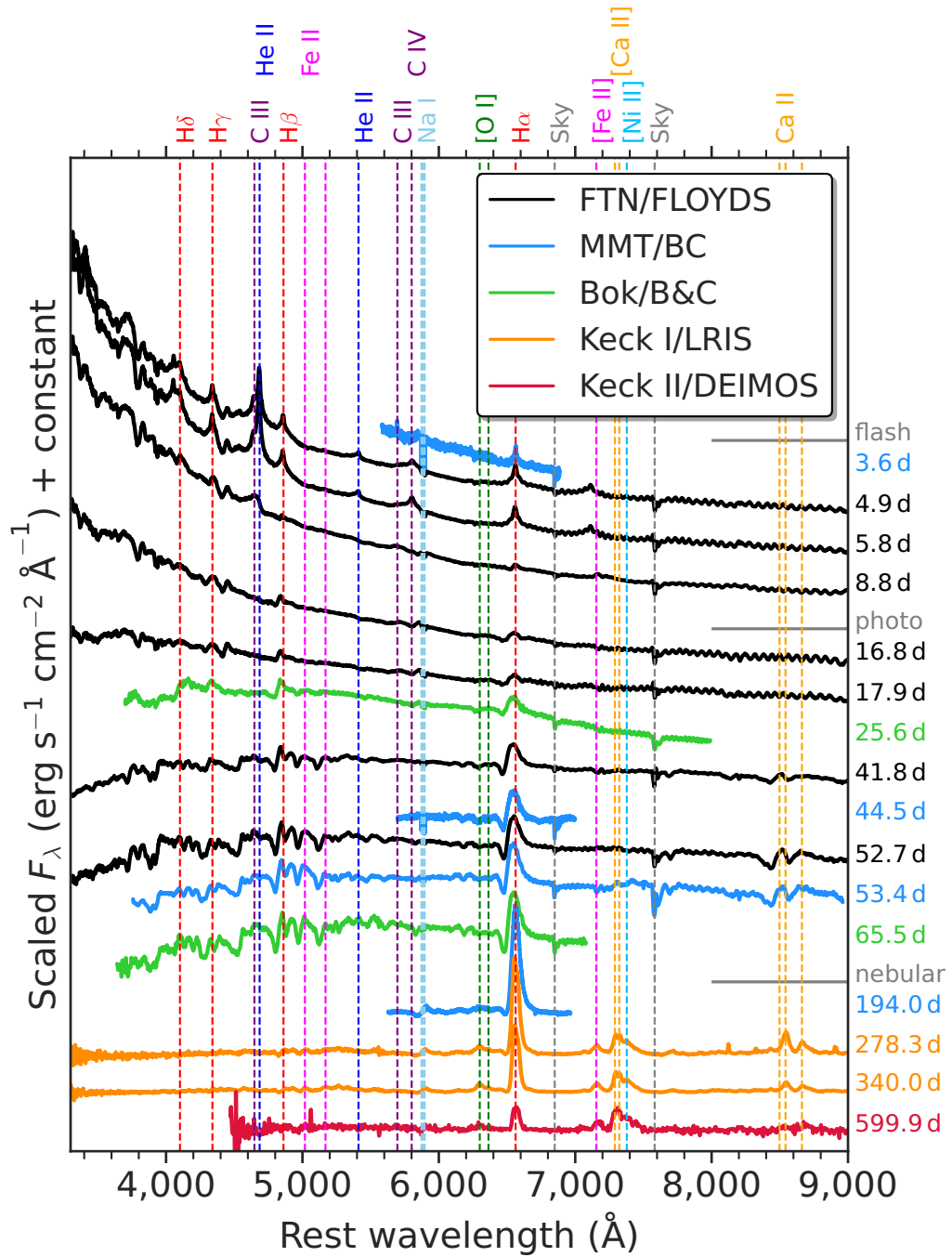
Figure 2.8: **Optical spectral time series of SN 2018zd.** The flash features (for example, He II, C III, and C IV) persist up to > 8.8 d and disappear before 16.8 d. Then the broad Balmer-series P Cygni lines appear, typical of the photospheric phase of a Type IIP SN. After ~ 200 d, the nebular emission lines (for example, Hα, [Ca II], and [Ni II]) dominate over the relatively flat continuum.
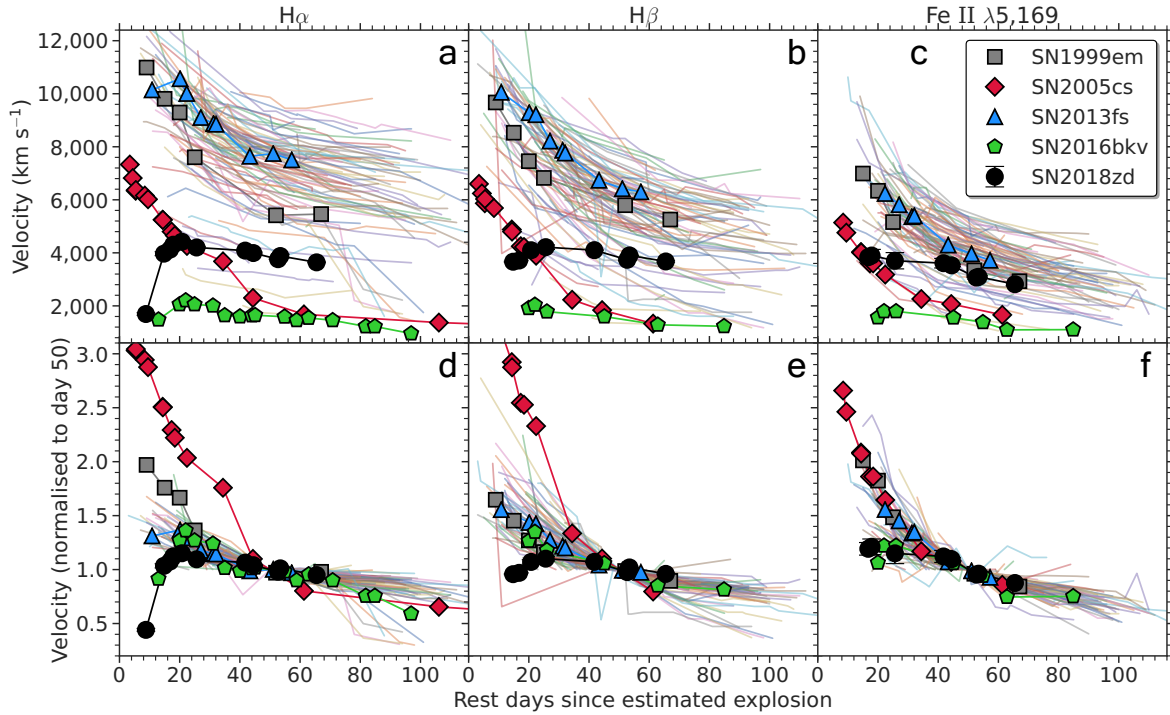
Figure 2.9: **Expansion velocities as a function of time.** Comparison of the unnormalised (**a, b, c**) and normalised (to day 50; **d, e, f**) Hα, Hβ, and Fe II λ5169 expansion velocities of SN 2018zd (§ 2.4.2) with a Type II SN sample (Gutiérrez et al. 2017a; transparent lines), including archetypal SN 1999em, along with low-luminosity SN 2005cs (Pastorello et al. 2009), early-flash SN 2013fs (Yaron et al. 2017), and low-luminosity and early-flash SN 2016bkv (Hosseinzadeh et al. 2018; Nakaoka et al. 2018). Error bars denote 1σ uncertainties and are sometimes smaller than the marker size. Note the pronounced early Hα and Hβ rises and the relatively flat velocity evolution (up to $\sim$ 30 d) of SN 2018zd, indicating shock propagation inside the dense, optically-thick CSM.
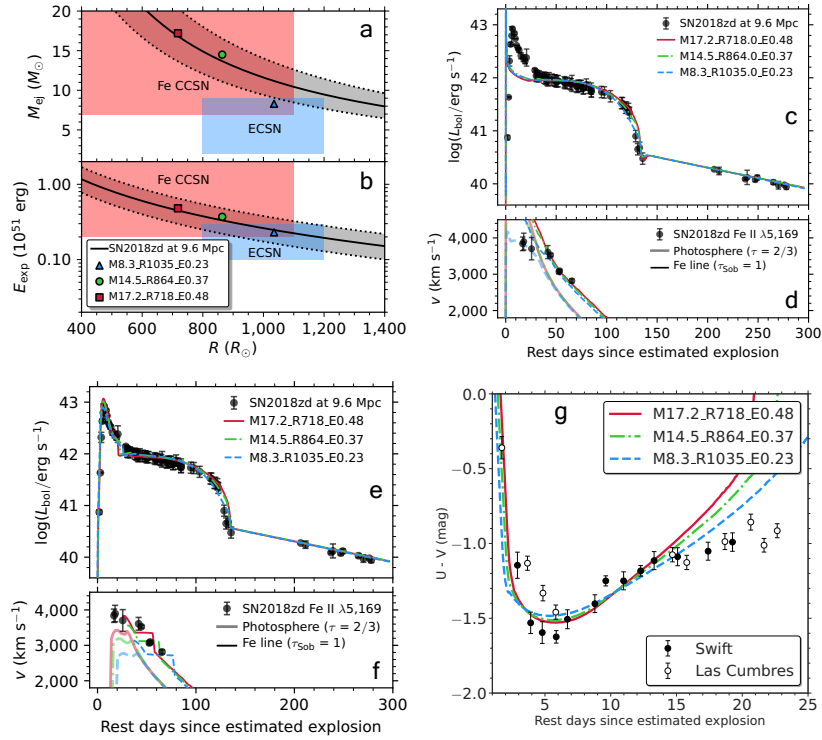
Figure 2.10: `MESA+STELLA` **progenitor and degenerate light-curve models. a,
b,** Ejecta mass M_{ej} and explosion energy E_{exp} inferred from Eq. (2.1) in §2.3.4 as a
function of progenitor radius R consistent with the bolometric light curve of SN 2018zd
at the assumed luminosity distance of 9.6 ± 1.0 Mpc, along with the properties of the
three degenerate explosion models. The blue and red shaded regions show explosion
parameters expected for ECSNe (Tominaga et al. 2013; Jones et al. 2013; Doherty
et al. 2017) and typical of Fe CCSNe (Sukhbold et al. 2016), respectively. **c, d,** Three
degenerate `MESA+STELLA` explosion models providing good fits to the light curve and
velocities inferred from the Fe II $\lambda 5169$ line during the plateau phase. Models are
labeled by $M[M_{ej,\odot}]\_R[R_\odot]\_E[E_{exp,51}]$. Error bars denote 1σ uncertainties. Note the
observed early-time excess luminosity and suppressed velocity of SN 2018zd. This
light-curve degeneracy highlights the inability to distinguish ECSNe from Fe CCSNe
solely based on their light curves, suggesting that many ECSNe might have been
overlooked owing to the lack of additional observations. **e, f,** Same as panels (**c,
d**), but adding a dense wind profile ($\dot{M}_{wind} = 0.01\, M_\odot\, yr^{-1}$, $v_{wind} = 20\, km\, s^{-1}$, and
$t_{wind} = 10$ yr) to the three degenerate `MESA` models before handoff to `STELLA`. **g,**
Comparison of the UV-colour models with the same wind CSM parameters as in panels
(**e, f**). Error bars denote 1σ uncertainties. All three models with the same wind CSM
parameters are able to reproduce the early-time luminosity excess and blueward UV
colour evolution almost identically, suggesting the insensitivity of a particular model
choice. Despite a possible artificial velocity kink when the Fe line-forming region
transitions from the CSM to the stellar ejecta, the velocity evolution with the early
suppression is also reproduced.

ECSN	Progenitor			Explosion		
Candidate	Identification	CSM	Chemical Composition	Energy	Light Curve	Nucleosynthesis
SN 2018zd	✓?	✓	✓	✓?	✓	✓
SN 1054 (Crab)	–	✓?	✓	✓	✓?	✓
ILRT	✓?	✓	?	×	×	?
Low-Lum. II-P	×	?	×	✓?	✓	×
IIn-P	?	✓	?	✓?	✓	✓?

Figure 2.11:   **ECSN candidate checklist.** Check marks, check+question marks, and cross marks (respectively) indicate observations consistent, perhaps consistent, and inconsistent with theoretical expectations. Dashed lines indicate the lack of observational constraints, and lone question marks indicate unknowns (§ 2.4.7). For SN 2018zd, we identify a faint progenitor candidate that may be consistent with an SAGB star (Figs. 2.5 & 2.6), and the explosion energy is consistent within the light-curve degeneracy (Fig. 2.10).
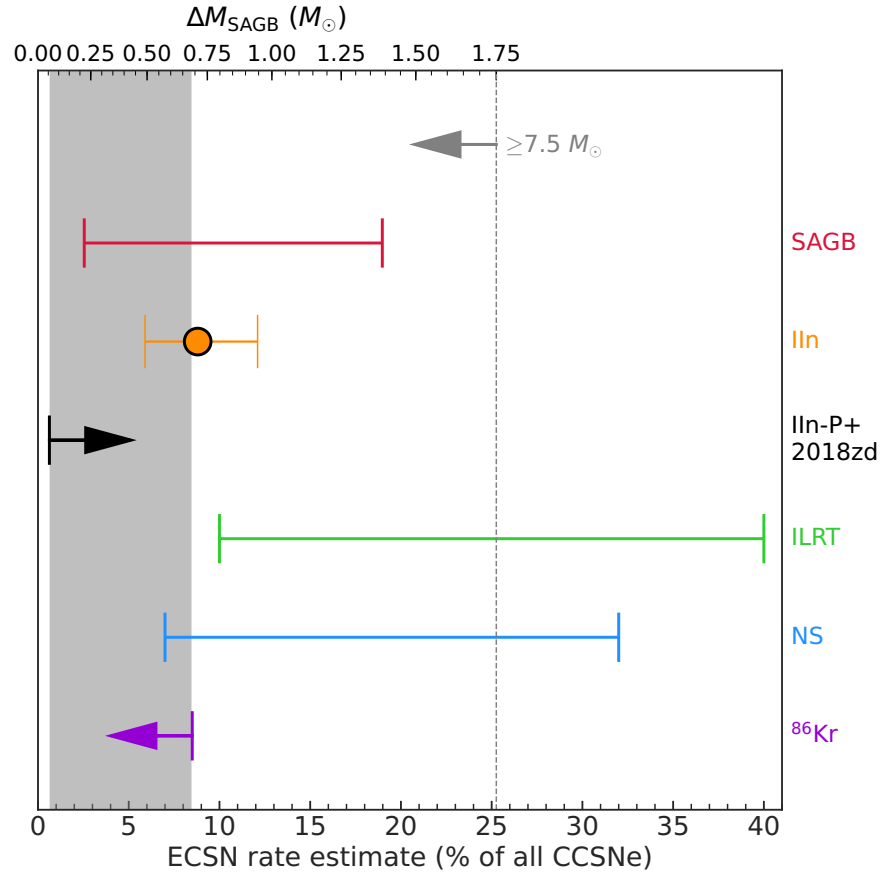
Figure 2.12:   **ECSN rate estimators.** Comparison of the ECSN rate estimates:
'SAGB' is the SAGB mass window from stellar evolutionary calculations at solar
metallicity (Poelarends et al. 2008); 'IIn' is the observed Type IIn SN rate from a vol-
ume-limited (≤ 60 Mpc) sample (Smith et al. 2011a); 'IIn-P+2018zd' is a rough lower
limit of the Type IIn-P SN rate within 60 Mpc combined with SN 2018zd (§ 2.3.5);
'ILRT' is a rough estimate from ILRTs within 30 Mpc (Thompson et al. 2009); 'NS' is
an estimated rate from the bimodality in the neutron star mass distribution (Schwab
et al. 2010) assuming that the low-mass and high-mass peaks originate from ECSNe
and Fe CCSNe, respectively; and '^{86}Kr' is an upper limit from the ECSN nucle-
osynthesis calculation (Wanajo et al. 2018) assuming that ECSNe are the dominant
production source of ^{86}Kr. The conversion between the fraction of all CCSNe and the
SAGB mass window is performed assuming the Salpeter initial mass function with
lower and upper CCSN mass limits of $7.5\,M_\odot$ and $120\,M_\odot$ (respectively) and maxi-
mum and minimum SAGB masses of $9.25\,M_\odot$ and $9.25\,M_\odot - \Delta M_{\mathrm{SAGB}}$ (respectively)
at solar metallicity (Poelarends et al. 2008). The grey vertical dotted line is where
the minimum SAGB mass equals the assumed lower CCSN mass limit of $7.5\,M_\odot$. The
grey shaded region shows a rough ECSN rate constraint by the IIn-P+2018zd lower
limit and the nucleosynthesis upper limit.

34

2.4   Supplementary Information

2.4.1   Follow-up Imaging

Follow-up imaging was obtained with the LCO network of $0.4\,\mathrm{m}$, $1\,\mathrm{m}$, and $2\,\mathrm{m}$ telescopes through GSP, the Neil Gehrels *Swift* Observatory Ultraviolet/Optical Telescope (UVOT), the Noguchi Astronomical Observatory (Chiba, Japan) $0.26\,\mathrm{m}$ telescope, and the Itagaki Astronomical Observatory (Okayama and Tochigi, Japan) $0.35\,\mathrm{m}$ and $0.5\,\mathrm{m}$ telescopes. For the LCO photometry, PSF fitting was performed using `lcogtsnpipe` (Valenti et al. 2016), a PyRAF-based photometric reduction pipeline. *UBV*- and *gri*-band data were calibrated to Vega (Stetson 2000) and AB (Albareti et al. 2017) magnitudes, respectively, using standard fields observed on the same night by the same telescope as the SN. The *Swift* UVOT photometry was conducted using the pipeline for the *Swift* Optical Ultraviolet Supernova Archive (SOUSA; Brown et al. 2014), including the updated sensitivity corrections and zeropoints (Breeveld et al. 2011) and the subtraction of the underlying host-galaxy count rates using images from October/November 2019. The unfiltered optical Itagaki (KAF-1001E CCD) and Noguchi (ML0261E CCD) photometry was extracted using `Astrometrica` (Raab 2012) and calibrated to the Fourth US Naval Observatory CCD Astrograph Catalog (UCAC4; Zacharias et al. 2013). All photometry will be available for download via WISeREP and the Open Supernova Catalog. We correct all photometry for the Milky Way (MW) and host-galaxy extinction (Fig. 2.7).

We estimate an explosion epoch by fitting a quadratic function $F_1(t - t_0)^2$ to the unfiltered Itagaki and first three Noguchi points with similar CCD spectral responses ($\lambda_{\mathrm{eff}} = 6500\text{--}6700\,\text{Å}$), where the effect of CSM interaction is less prominent than in the UV bands (Fig. 2.7). This yields an explosion epoch $t_0 = \mathrm{MJD}\,58178.4 \pm 0.1$, where the uncertainty is estimated from the difference between the explosion epoch and the first Itagaki detection. Even if we use the most conservative explosion epoch of the last

nondetection on MJD 58175.5, the difference is only 2.9 rest-frame days, not affecting the main results of this paper.

We fit a blackbody SED to every epoch of the LCO and *Swift* photometry containing at least three filters (excluding the r band owing to strong Hα contamination) obtained within 0.3 d of each other to estimate the blackbody temperature and radius at the assumed luminosity distance (note that the observed SED peaks are bluer than the *Swift* wavelength coverage 3–10 d after the explosion, potentially underestimating the blackbody temperatures; Valenti et al. 2016). Then we integrate the fitted blackbody SED to obtain bolometric (and pseudobolometric) luminosity at each epoch. Since we only have the unfiltered Noguchi photometry during the plateau drop owing to the Sun constraint, we estimate a bolometric (and pseudobolometric) correction by finding the offset of the Noguchi photometry to the LCO and *Swift* integrated bolometric (and pseudobolometric) luminosity during the plateau phase (50–80 d) where most of the SED ($\sim 80\%$) is in the spectral response range of the unfiltered CCD. Then we apply the bolometric (and pseudobolometric) correction to the Noguchi photometry and include it in the bolometric (and pseudobolometric) light curve during the plateau drop (Fig. 2.1). This procedure is also justified by the good agreement with the tail bolometric (and pseudobolometric) luminosity obtained from the LCO multiband photometry after the Sun constraint.

2.4.2   Follow-up Spectroscopy

Follow-up spectra were obtained with the FLOYDS spectrograph mounted on the LCO 2 m Faulkes Telescope North (FTN) through GSP, the Boller & Chivens (B&C) spectrograph mounted on the 2.3 m Bok telescope, the Blue Channel (BC) spectrograph mounted on the 6.5 m MMT, and the Low Resolution Imaging Spectrometer (LRIS; Oke

et al. 1995; McCarthy et al. 1998; Rockosi et al. 2010) and the DEep Imaging Multi-Object Spectrograph (DEIMOS; Faber et al. 2003) mounted on the 10 m Keck-I and Keck-II telescopes, respectively. For the FLOYDS observations, a 2″-wide slit was placed on the target at the parallactic angle (to minimise the effects of atmospheric dispersion; Filippenko 1982). One-dimensional spectra were extracted, reduced, and calibrated following standard procedures using `floyds_pipeline` (Valenti et al. 2014). The Bok low-resolution optical spectra were taken with the 300 lines mm^{-1} grating using a 1.5″-wide slit, and the MMT moderate-resolution spectra were obtained using a 1.0″-wide slit. The spectra were reduced using standard techniques in IRAF, including bias subtraction, flat-fielding, and sky subtraction. Flux calibration was done with spectrophotometric standard star observations taken on the same night at similar airmass. The Keck LRIS spectra were reduced using the `Lpipe` pipeline (Perley 2019) with the default parameters and standard spectroscopic reduction techniques. The Keck DEIMOS spectrum was reduced with a custom-made Python pipeline that performs flat-field correction, sky subtraction, optimal extraction (Horne 1986), and flux calibration using a standard star observed on the same night as the SN. All spectra will be available for download via WISeREP and the Open Supernova Catalog. We correct all spectra for the MW and host-galaxy extinction and calibrate the flux using the photometry (Fig. 2.8).

We measure expansion velocities of Hα, Hβ, and Fe II λ5169 from the absorption minimum by fitting a P Cygni profile to each line in the spectra (Fig. 2.8). Then we translate the difference between the observed minimum and the rest wavelength of the line to an expansion velocity using the relativistic Doppler formula (Fig. 2.9). We estimate the velocity uncertainties by randomly varying the background region by ± 5 Å.

We simultaneously fit Gaussian functions to He I λ7065, [Fe II] λ7155, [Fe II] λ7172, [Ca II] λ7291, [Ca II] λ7323, [Ni II] λ7378, [Fe II] λ7388, [Ni II] λ7412, and [Fe II] λ7452 in the nebular spectra assuming a single full width at half-maximum intensity (FWHM)

velocity for all lines and the theoretically expected line ratios for the [Ca II], [Fe II], and [Ni II] lines (Jerkstrand et al. 2015; Fig. 2.4). The resultant [Ni II] $\lambda7378$/[Fe II] $\lambda7155$ intensity ratios and FWHM velocities are 1.3–1.6 and 2,500–2,100 km s^{-1}, respectively, from 278 to 600 d after the explosion.

2.4.3   Follow-up Spectropolarimetry

Follow-up spectropolarimetric observations of SN 2018zd were obtained using the CCD Imaging/Spectropolarimeter (SPOL; Schmidt et al. 1992) on the 6.5 m MMT telescope using a 2.8″ slit on 2018 April 23 (53 d after the explosion). We used a 964 lines mm^{-1} grating with a typical wavelength coverage of 4,050–7,200 Å and a resolution of ~ 29 Å. We used a rotatable semi-achromatic half-wave plate to modulate incident polarization and a Wollaston prism in the collimated beam to separate the orthogonally polarized spectra onto a thinned, anti-reflection-coated 800×1200 pixel SITe CCD. The efficiency of the wave plate as a function of wavelength was measured and corrected for by inserting a fully-polarizing Nicol prism into the beam above the slit. A series of four separate exposures that sample 16 orientations of the wave plate yield two independent, background-subtracted measures of each of the linear Stokes parameters, Q and U. Two such sequences were acquired and combined to increase the signal-to-noise ratio.

Our spectropolarimetric analysis is performed primarily using the normalised linear Stokes parameters, $q = Q/I$ and $u = U/I$, which are rotated with respect to each other, allowing us to decompose the polarization signal into orthogonal components in position-angle space. We use the debiased polarization level, $p_{\rm db} = \sqrt{|(q^2 + u^2) - \frac{1}{2}(\sigma_q^2 + \sigma_u^2)|}$, in favour of the standard polarization level, $p = \sqrt{q^2 + u^2}$, because the standard polarization level is a positive-definite quantity that measures the distance from the origin in a q vs. u plane. When the signal-to-noise ratio is low, this positive-definite quantity can

be misleading, whereas the debiased polarization value accounts for large uncertainty in measurements of q and u.

SN 2018zd exhibits a mean polarization of 0.9% across the continuum at 5,100–5,700 Å and 0.8% across the continuum at 6,000–6,300 Å. However, the polarization does not vary much across the entire spectrum, even across absorption and emission-line features. Typically, a polarized continuum would become depolarized across emission-line features owing to dilution with unpolarized light from the emission line. Since SN 2018zd does not exhibit any such changes across any of its emission-line features, we suggest that the majority of the polarization signal arises in the interstellar medium rather than in the SN itself. The Serkowski relation (Serkowski et al. 1975) suggests that $p_{\max} < 9\,E(B-V)$. If all 0.9% of the continuum peak polarization in SN 2018zd were due to the interstellar medium, then we could estimate the extinction to be $E(B-V) > p_{\max}/9 = 0.1\,\mathrm{mag}$ and a reddening of at least $A_V = 3.1\,E(B-V) = 0.31\,\mathrm{mag}$.

2.4.4   Extra `MESA+STELLA` Modeling Description

All progenitor models began at solar metallicity ($Z = 0.02$), and the naming scheme gives progenitor and explosion properties: $(\mathrm{M}[M_{\mathrm{ej}}/M_\odot]\_\mathrm{R}[R/R_\odot]\_\mathrm{E}[E_{\mathrm{exp}}/10^{51}\,\mathrm{erg}])$. The high-ejecta-mass model, M17.2_R718_E0.48, is $18.8\,M_\odot$ at core collapse ($20\,M_\odot$ at ZAMS) with no rotation, no exponential overshooting ($f_{\mathrm{ov}} = f_{0,\mathrm{ov}} = 0.0$), mixing length $\alpha_{\mathrm{env}} = 2.0$ in the H-rich envelope, and a wind efficiency factor $\eta_{\mathrm{wind}} = 0.4$. The moderate model, M14.5_R864_E0.37, is $16.3\,M_\odot$ at core collapse ($17\,M_\odot$ at ZAMS) with modest initial rotation $\Omega/\Omega_{\mathrm{crit}} = 0.2$, no exponential overshooting, $\alpha_{\mathrm{env}} = 2.0$, and $\eta_{\mathrm{wind}} = 0.2$. The low-ejecta-mass and large-radius model, M8.3_R1035_E0.23, is $11.8\,M_\odot$ at core collapse ($15\,M_\odot$ at ZAMS) with modest rotation $\Omega/\Omega_{\mathrm{crit}} = 0.2$, moderately high exponential overshooting ($f_{\mathrm{ov}} = 0.018$, $f_{0,\mathrm{ov}} = 0.006$), $\alpha_{\mathrm{env}} = 2.0$, and $\eta_{\mathrm{wind}} = 0.9$. Despite the ZAMS

mass typical of an RSG, this model sufficiently captures the relevant explosion properties for the SAGB explosion scenario, as the mass of the H-rich ejecta, explosion energy, and progenitor radius determine the plateau properties of Type IIP SNe, not the ZAMS mass.

In MESA revision 12115, a thermal bomb was injected in the innermost $0.1\,M_\odot$ of each model, heating the star to the desired total final energy $E_{\rm exp}$, with the updated prescription for removing material falling back onto the inner boundary (Paxton et al. 2019; Goldberg et al. 2019), which can be relevant at the low explosion energies required here. Of the three explosions, only M8.3_R1035_E0.23 undergoes substantial late-time fallback, totaling $2\,M_\odot$, which is excised from the model with no extra heating and negligible change in the total explosion energy. The evolution of the shock was modelled in MESA with the 'Duffell RTI' prescription for mixing via the Rayleigh-Taylor instability (Duffell 2016; Paxton et al. 2018), terminating near shock breakout, when the shock reaches a mass coordinate of $0.04\,M_\odot$ below the outer boundary of each model. The ^{56}Ni distribution in each model was then scaled to match the observed value of $0.0086\,M_\odot$. Then in STELLA, bolometric light curves and expansion velocities were produced using 600 spatial zones and 100 frequency bins, without any additional material outside the stellar photosphere. For models with CSM, 600 zones are used in STELLA, including 400 zones for the original ejecta, and 200 additional zones for the wind model.

2.4.5 Host Galaxy

NGC 2146 is an edge-on spiral galaxy with several tidal streams that were probably ejected during a galaxy merger event $\sim 800\,{\rm Myr}$ ago (Taramopoulos et al. 2001; Fig. 2.5). The presence of a starburst-driven superwind from the bulge is revealed across the electromagnetic spectrum from γ-rays to IR (Tang et al. 2014; Armus et al. 1995; Taramopoulos et al. 2001; Kreckel et al. 2014), indicating an ongoing high star-formation

rate (SFR $\approx 10\,M_\odot\,\mathrm{yr}^{-1}$; Skibba et al. 2011). On the basis of radio observations of the bulge (Tarchi et al. 2000), there are many more dense H II regions (each containing up to 1000 type O6 stars) than supernova remnants, suggesting a relatively young phase of the starburst. The bulge has a high dust content and roughly solar metallicity $(12 + \log_{10}[\mathrm{O/H}] = 8.68 \pm 0.10$; Skibba et al. 2011; Aniano et al. 2020). Since SN 2018zd is at a relatively large separation from the nucleus of $1'.83$ northwest ($36''.1$ north, $103''.7$ west; Fig. 2.5), and the galactic radius parameter $R_{25} = 1'.78$ (via the NASA/IPAC Extragalactic Database), if we reasonably assume that there is an abundance gradient for the galaxy, the metallicity at the SN site is probably subsolar; this merits future investigations once the SN fades.

2.4.6   Alternative Scenarios

A low-mass ($\lesssim 9.6\,M_\odot$) Fe CCSN is a possible alternative for SN 2018zd, as similar explosion energy ($\sim 10^{50}\,\mathrm{erg}$; Müller et al. 2019) and nucleosynthesis (Wanajo et al. 2018) to ECSNe may be expected because of a similar steep density gradient outside the degenerate core. For a low-mass RSG star, however, no high constant ($\gtrsim 10^{-5}\,M_\odot\,\mathrm{yr}^{-1}$; Mauron & Josselin 2011; Goldman et al. 2017; Beasor et al. 2020) and/or eruptive (Smartt 2009; Fuller 2017) mass loss is expected to produce dense confined He-, C-, and N-rich, but O-poor CSM (but note that the mass loss is quite sensitive to the model treatments of, for example, convection and off-center nuclear burning; Woosley & Heger 2015). In addition, a low-mass RSG has Si-, O-, and He-rich layers (Jones et al. 2013) which are expected to produce additional Si, S, Ca, Mg, O, C, and He lines in nebular spectra (Jerkstrand et al. 2018). Thus, a low-mass Fe CCSN may be able to explain the light-curve morphology, but probably not the early-time CSM interaction and nebular spectra observed for SN 2018zd.

On the other side of the progenitor mass spectrum, another possible alternative for SN 2018zd is a high-mass ($\gtrsim 25\,M_\odot$) Fe CCSN, as small kinetic energy ($\sim 10^{50}\,\mathrm{erg}$) and ejected radioactive ^{56}Ni mass ($\lesssim 10^{-3}\,M_\odot$) may be expected owing to fallback accretion onto the central remnant (Lisakov et al. 2018; Chan et al. 2018). For such high fallback accretion, however, extra luminosity ($L \propto t^{-5/3}$) at late times ($t \gtrsim 200\,\mathrm{d}$) is expected (Dexter & Kasen 2013; Moriya et al. 2019). Also, no ejected stable ^{58}Ni should be observed, as it is produced in the innermost neutron-rich layer (Wanajo et al. 2009). Thus, a high-mass Fe CCSN may be able to explain the photospheric light curve, but not the late-time exponential tail and nebular spectra of SN 2018zd.

If the luminosity distance to NGC 2146 were larger than 12 Mpc, it would be quite unlikely that SN 2018zd is an ECSN, since $M_{\mathrm{Ni}} > 0.01\,M_\odot$, $E_{\mathrm{exp}} > 4 \times 10^{50}\,\mathrm{erg}$, and $M_{\mathrm{ej}} > 10\,M_\odot$ in a reasonable progenitor radius range of 400–1400 $R_\odot$ according to the light-curve scaling (Eq. 2.1 in §2.3.4). Then SN 2018zd would become a real challenge to stellar evolution and SN explosion theories to reconcile all of the observational ECSN indicators with a higher M_{Ni}, E_{exp}, M_{ej}, and M_{ZAMS} for the progenitor. If the luminosity distance were 18 Mpc, the progenitor candidate detection of SN 2018zd in *HST* F814W would become as bright as that of the SN 2005cs progenitor (Fig. 2.6), but still on the faint end of Type II SN progenitors (Smartt 2009, 2015) despite the expected higher M_{ej} and M_{ZAMS} from the light-curve scaling.

We note that Zhang et al. (2020) also discusses a possible ECSN origin for SN 2018zd based on the small radioactive ^{56}Ni yield, dense CSM, and faint X-ray radiation. Owing to their adopted larger luminosity distance ($18.4 \pm 4.5\,\mathrm{Mpc}$; §2.3.2), however, they suggest that SN 2018zd is a member of the class of luminous Type II SNe with low expansion velocities (Rodríguez et al. 2020), which probably arise from extended CSM interaction (4–11 weeks after the explosion). In this work, we perform numerical light-curve modeling and demonstrate that ECSN-parameter explosions with the early CSM interaction

(~ 30 days after the explosion) can reproduce both the light-curve and velocity evolution (Figs. 2.2 & 2.10). Furthermore, we present the progenitor candidate identification (Figs. 2.5 & 2.6) and more detailed spectral analyses (Figs. 2.3 & 2.4), showing that the chemical composition and nucleosynthesis are consistent with those expected for ECSNe.

2.4.7   Other ECSN Candidates.

SN 1054, whose remnant is the Crab Nebula, has been suggested as an ECSN candidate (Nomoto et al. 1982; Nomoto 1984, 1987; Smith 2013; Tominaga et al. 2013; Moriya et al. 2014). It shows He-, C-, and Ni-rich ejecta, but O- and Fe-poor abundances (Hudgins et al. 1990; Satterfield et al. 2012), small ejecta mass ($4.6 \pm 1.8 \, M_\odot$; Fesen et al. 1997), and low kinetic energy ($\sim 10^{49}$ erg; Smith 2013). The slowly expanding filaments ($\sim 1200 \, \mathrm{km \, s^{-1}}$) without a blast wave outside probably indicate the presence of CSM decelerating the SN ejecta (Fesen et al. 1997; Smith 2013), and the historical light curve of SN 1054 may be similar to that of ECSNe (Smith 2013; Tominaga et al. 2013; Moriya et al. 2014). However, the observed relatively high neutron star kick velocity ($\sim 160 \, \mathrm{km \, s^{-1}}$) is at odds with those theoretically predicted for ECSNe ($< 10 \, \mathrm{km \, s^{-1}}$; Gessner & Janka 2018). On the other hand, the pre-collapse O+Ne+Mg core of an SAGB star could have large rotation and even 'super-Chandrasekhar' mass if the angular momentum transport from the rotating core to the very extended SAGB envelope is small during contraction (Uenishi et al. 2003; Benvenuto et al. 2015; Hachisu et al. 2012). The collapse of such an unstable core could in principle yield a large spin and kick.

In addition to SN 1054, other previously suggested ECSN candidates can be divided into three main types: intermediate-luminosity red transients (ILRTs; for example, SN 2008S and AT 2017be; Prieto et al. 2008; Botticella et al. 2009; Thompson et al. 2009; Adams et al. 2016; Cai et al. 2018; Stritzinger et al. 2020), low-luminosity Type IIP SNe

(Kitaura et al. 2006; Janka et al. 2008; Spiro et al. 2014; Hosseinzadeh et al. 2018), and Type IIn-P SNe (Fig. 2.11; for example, SNe 2009kn and 2011ht; Kankare et al. 2012; Mauerhan et al. 2013; Moriya et al. 2014; Smith 2013).

ILRTs are the luminosity gap transients between novae and SNe, whose origin has been debated as either a massive-star outburst (Bond et al. 2009; Berger et al. 2009; Smith et al. 2009, 2011b) or a terminal ECSN explosion (Prieto et al. 2008; Botticella et al. 2009; Thompson et al. 2009; Adams et al. 2016; Cai et al. 2018; Stritzinger et al. 2020). Their progenitors are surrounded by dusty, optically thick shells, resulting in CSM-dominated transients (Prieto et al. 2008; Botticella et al. 2009; Thompson et al. 2009; Bond et al. 2009; Berger et al. 2009; Adams et al. 2016). However, their faint light-curve morphology with CSM interaction requires extremely low explosion energy ($\lesssim 10^{48}$ erg) that is unexpected for ECSNe (Tominaga et al. 2013; Moriya et al. 2014; Moriya & Eldridge 2016), and their chemical composition and nucleosynthesis are unclear owing to the lack of nebular-phase spectra.

Low-luminosity Type IIP SNe typically yield low ^{56}Ni mass ($\lesssim 10^{-2} M_{\odot}$; Spiro et al. 2014) with ECSN-like light-curve morphology (Fig. 2.1). However, their chemical composition and nucleosynthesis are inconsistent with ECSNe (Jerkstrand et al. 2018) (Fig. 2.14), and their CSM density is generally low compared with that expected from ECSNe (Poelarends et al. 2008; Moriya et al. 2014, except for SN 2016bkv; Hosseinzadeh et al. 2018). Low-mass RSG progenitors have been directly identified for SNe 2003gd (Maund et al. 2014b), 2005cs (Eldridge et al. 2007; Maund et al. 2014b), and 2008bk (Maund et al. 2014a), excluding SAGB stars – the progenitors of ECSNe.

Type IIn-P SNe show Type IIn-like narrow CSM emission lines in spectra and Type IIP-like light-curve morphology with large plateau drops similar to ECSNe (Kankare et al. 2012; Mauerhan et al. 2013; Smith 2013; Moriya et al. 2014; Fig. 2.13). The SN signatures (for example, chemical abundance) are mostly hidden below the CSM interaction,

in general. For Type IIn-P SN 2011ht (Humphreys et al. 2012), however, we measure [Ni II] $\lambda7378$/[Fe II] $\lambda7155 = 3.8$ at 155 d after the explosion (using a public spectrum on WISeREP), which may indicate ECSN-like nucleosynthesis, although the spectrum may not be fully nebular given the relatively early phase. While no SN IIn-P progenitors have been directly identified, a pre-explosion outburst has been observed for SN 2011ht (Fraser et al. 2013). The true nature of Type IIn-P SNe is yet to be revealed.

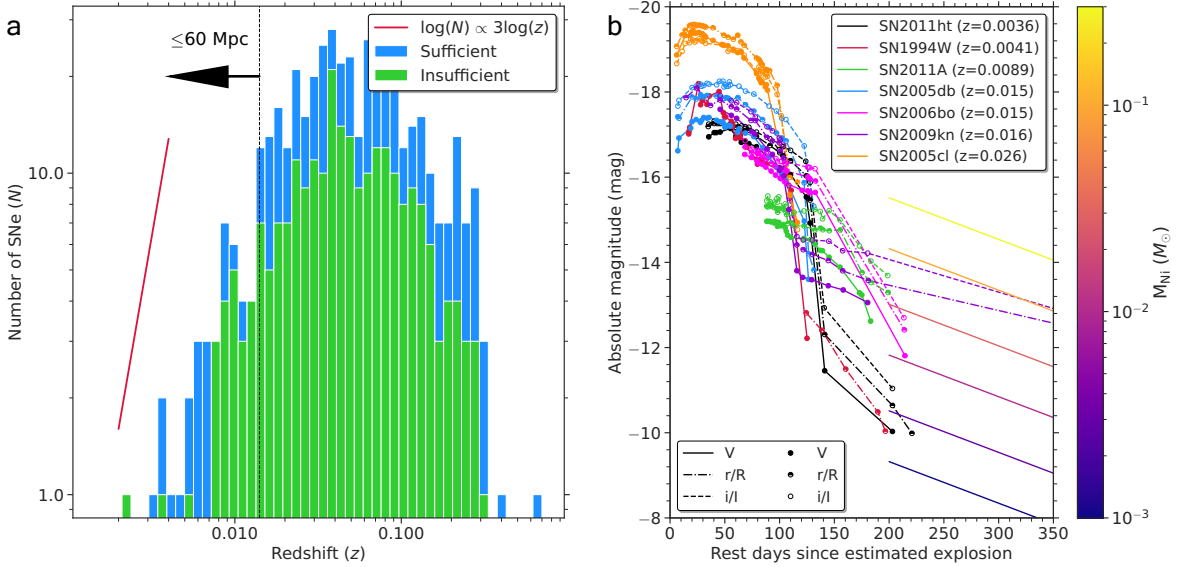Figure 2.13: **Public Type IIn and IIn-P SN samples. a,** Redshift distribution of the 455 public Type IIn SNe retrieved from WISeREP and/or TNS. 241 objects have insufficient public spectra and/or light curves to secure the Type IIn classifications and/or to be identified as Type IIn-P SNe, but are included in the sample so as not to overestimate the lower limit. The red line is the number-density slope by assuming the volume term with the standard cosmology ($H_0 = 71.0 \text{ km s}^{-1} \text{ Mpc}^{-1}$, $\Omega_{\Lambda_0} = 0.7$, and $\Omega_{m_0} = 0.3$, giving $d_L \propto z$ for $z < 0.1$). The black dotted line is the distance cut ($\leq 60 \text{ Mpc}$) we apply to compare with the LOSS sample (Smith et al. 2011 a). By comparing the number-density slope to the sample histogram as a first-order estimation, the sample does not seem to suffer substantially from incompleteness within 60 Mpc. **b,** Comparison of the identified Type IIn-P SN candidates by applying the two light-curve criteria. The explosion epochs of SNe 2006bo and 2011A are not well constrained and can shift up to $\pm 64 \text{ d}$ and $\pm 85 \text{ d}$, respectively (Taddia et al. 2013; de Jaeger et al. 2015). The colour-coded tails at 200–350 d are the expected V-band tails from the fully trapped radioactive heating for a given ^{56}Ni mass (Hamuy 2003). The observed Ni-mass upper limits are within 10^{-3} to $3 \times 10^{-2} \, M_\odot$, assuming that the tails are purely powered by the radioactive heating.
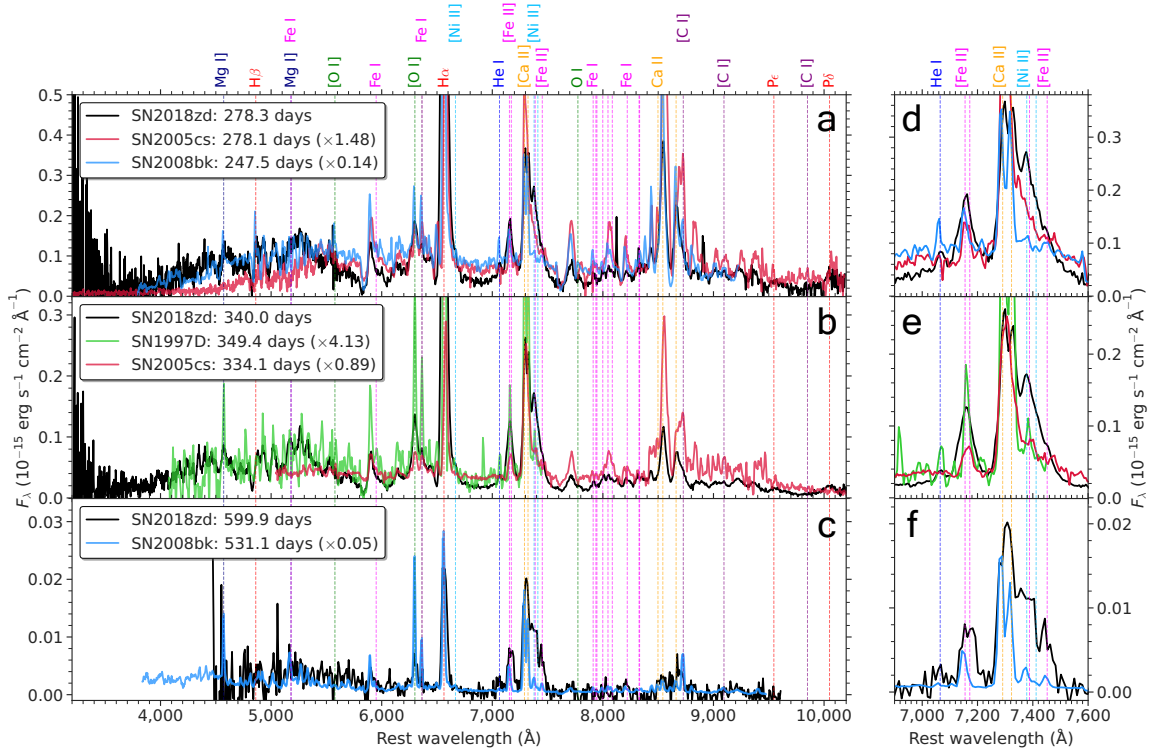
Figure 2.14: **Nebular spectral time series of low-luminosity Type IIP SNe.**
a–c, Comparison of the nebular spectral time series of SN 2018zd with the scaled (by
integrated flux as in the legend) and resampled low-luminosity Type IIP SNe 1997D
(Benetti et al. 2001), 2005cs (Pastorello et al. 2009), and 2008bk (Van Dyk et al. 2012;
Maguire et al. 2012; Gutiérrez et al. 2017a). In ascending order of wavelength, note the
distinct Mg I] λ4571 and [O I] $\lambda\lambda$6300, 6364 + Fe I λ6364 observed in SN 1997D; Fe I
cluster 7,900–8,500 Å, [C I] λ8727, and [C I] λ9100 observed in SN 2005cs; and Mg I]
λ4571, [O I] $\lambda\lambda$6300, 6364 + Fe I λ6364, Fe I cluster 7,900–8,500 Å, and [C I] λ8727
observed in SN 2008bk. **d–f,** Same as panels (**a**)–(**c**), but zoomed into the wavelength
range of interest (as in Fig. 2.4). Note the line-intensity ratios of [Ni II] λ7378/[Fe II]
λ7155 < 1 observed in SNe 1997D, 2005cs, and 2008bk. The strong C, O, Mg, and/or
Fe lines combined with the weak Ni lines observed in SNe 1997D, 2005cs, and 2008bk
are inconsistent with the ECSN chemical composition and nucleosynthesis.

47

Chapter 3

Luminous Type II Short-Plateau Supernovae

This chapter is reproduced from Hiramatsu et al. (2021a) by permission of the American Astronomical Society. I would like to thank my coauthors, without whom this work would not have been possible: D. Andrew Howell, Takashi J. Moriya, Jared A. Goldberg, Griffin Hosseinzadeh, Iair Arcavi, Joseph P. Anderson, Claudia P. Gutiérrez, Jamison Burke, Curtis McCully, Stefano Valenti, Lluís Galbany, Qiliang Fang, Keiichi Maeda, Gastón Folatelli, Eric Y. Hsiao, Nidia I. Morrell, Mark M. Phillips, Maximilian D. Stritzinger, Nicholas B. Suntzeff, Mariusz Gromadzki, Kate Maguire, Tomás E. Müller-Bravo, and David R. Young.

3.1   Introduction

The majority of massive stars ($M_{\mathrm{ZAMS}} \gtrsim 9\,M_\odot$) end their lives when their Fe cores collapse and explode as SNe II (Smartt 2009, 2015). The difference in progenitor's H-rich envelope mass at the moment of core collapse likely results in different SN II subtypes (e.g., Nomoto et al. 1995; Heger et al. 2003; Dessart et al. 2011, 2016b; Eldridge et al. 2017, 2018): SNe IIP (light-curve plateau of ~ 100 days); SNe IIL (linear decline light curve); and SNe IIb (spectrum dominated initially by H and then by He), in descending

order (see Arcavi 2017 for a review). SNe IIn show narrow H emission lines, indicating strong CSM interaction (see Smith 2017 for a review). Based on the direct progenitor identifications in pre-explosion images, the current consensus is that the progenitors are RSGs for SNe IIP; yellow supergiants in a binary system for SNe IIb; luminous blue variables and RSGs/SAGB stars for SNe IIn; and RSGs and/or yellow supergiants for SNe IIL, in descending order of confidence (see Van Dyk 2016 for a review).

The division between SNe IIP and IIL is both arbitrary and controversial because it is solely based on the shape of their photospheric-phase optical light curves (Barbon et al. 1979), while SNe IIb and IIn are spectroscopically distinct. There have been claims of distinct light-curve populations of SNe IIP and IIL (e.g., Arcavi et al. 2012; Faran et al. 2014), but larger light-curve samples have increased the support for a more continuous population (e.g., Anderson et al. 2014; Sanders et al. 2015; Galbany et al. 2016 b; Valenti et al. 2016). While SNe IIP and IIL show a continuous range of spectroscopic properties in optical (e.g., Gutiérrez et al. 2017b,c), Davis et al. (2019) recently find a strong dichotomy of NIR spectroscopic properties between SNe IIP and IIL, which may point to differences in the immediate environment.

In terms of the photospheric plateau duration, it is puzzling that SNe II with short plateaus (tens of days) are rarely observed (see e.g., Nakaoka et al. 2019 and Bostroem et al. 2020 for peculiar SNe IIb and IIL), despite analytical and numerical predictions that the plateau duration scales continuously with progenitor and explosion properties (Popov 1993; Kasen & Woosley 2009; Sukhbold et al. 2016; Goldberg et al. 2019). In a broader context of SN II population, it is also an outstanding question whether SNe IIP/L and IIb form a continuum or not (e.g., Arcavi et al. 2012; Faran et al. 2014; Pessi et al. 2019).

The increasing sample size of SNe IIP/L suggests that CSM interaction, resulting from violent pre-explosion mass loss, plays a key role even when their spectra do not

show IIn-like Balmer emission lines. By fitting numerical models to the Valenti et al. (2015, 2016) light-curve sample, Morozova et al. (2017, 2018) show that SNe IIP from RSG progenitors with CSM interaction can reproduce SNe IIL. They also show that CSM interaction is required in even normal SNe IIP to reproduce the rapid UV-optical rise in the models (see also Moriya et al. 2011, 2017, 2018a; Förster et al. 2018).

The observed RSG population (in MW, Magellanic Clouds, M31, and M33) lies in a luminosity range of $4.5 \lesssim \log_{10}(L/L_\odot) \lesssim 5.5$, implying their ZAMS mass range of ~ 9–$25\,M_\odot$ based on theoretical stellar tracks (e.g., Levesque et al. 2005, 2006; Massey et al. 2009; Drout et al. 2012; Gordon et al. 2016). However, Smartt (2009, 2015) show that the best-fit cumulative Salpeter initial mass function (IMF; Salpeter 1955) on 26 pre-explosion detections/limits of SNe IIP/L progenitors truncates below the high-luminosity end of RSGs, translating to a ZAMS mass upper limit of $\lesssim 18\,M_\odot$. This is referred to as the *red supergiant problem*, since there seems to be a lack of SNe II with identified progenitors in the range ~ 18–$25\,M_\odot$. Due to the complicated evolution of terminal massive stars and observational uncertainties in dust extinction and bolometric correction, the statistical significance and robustness of the RSG problem has been a highly debated topic (e.g., Walmswell & Eldridge 2012; Eldridge et al. 2013; Kochanek 2014; Meynet et al. 2015; Sukhbold et al. 2016; Adams et al. 2017; Davies & Beasor 2018).

Here, we report optical/NIR photometry and spectroscopy of Type II SNe 2006Y, 2006ai, and 2016egz. In §3.2 & 3.3, we summarize their discoveries, follow-up observations, and data reduction. In §3.4, we analyze their host galaxies, light curves, and spectra, in addition to producing a large single-star model grid by varying different progenitor and explosion properties. This reveals their transitional nature between SNe IIL and IIb with small H-rich envelope mass, high progenitor ZAMS mass, and dense CSM estimates. As such, we discuss their formation channel and implications for the RSG problem in §3.5. Finally, we summarize our findings and draw conclusions in §3.6.

3.2   Discoveries

Luckas et al. (2006b) discovered SN 2006Y on 2006 February 3.58 (UT dates are used throughout) at 17.7 mag at R.A. $= 07^{\mathrm{h}}13^{\mathrm{m}}17^{\mathrm{s}}.17$ and Dec. $= -51°41'18".8$ with a subsequent detection on 2006 February 7.60 at 17.3 mag and last non-detection limit on 2006 January 27.59 at 18.5 mag, using the unfiltered 35 cm Tenagra telescope at Perth, Australia. With the same instrumental setup, Luckas et al. (2006a) discovered SN 2006ai on 2006 February 17.54 at 16.2 mag at R.A. $= 07^{\mathrm{h}}29^{\mathrm{m}}52^{\mathrm{s}}.16$ and Dec. $= -84°02'20".5$ with a subsequent detection on 2006 February 19.52 at 16.0 mag and last non-detection limit on 2005 December 16.79 at 18.5 mag. Morrell & Folatelli (2006) obtained optical spectra of SNe 2006Y and 2006ai on February 27.14 and March 5.12, respectively, with the Las Campanas 2.5 m du Pont telescope through the Carnegie Supernova Project-I (CSP-I; Hamuy et al. 2006), classifying them as SNe II. CSP-I also obtained optical spectra of the host galaxies of SNe 2006Y and 2006ai and measured redshifts of $z = 0.0336 \pm 0.0001$ and 0.0158 ± 0.0001, respectively.

The All-Sky Automated Survey for Supernovae (ASAS-SN; Shappee et al. 2014) discovered SN 2016egz (ASASSN-16hn) on 2016 July 24.32 at 16.1 mag at R.A. $= 00^{\mathrm{h}}04^{\mathrm{m}}03^{\mathrm{s}}.854$ and Dec. $= -34°48'51".87$ with a last non-detection limit on 2016 July 17.23 at 17.4 mag, using the V-band 14 cm ASAS-SN Cassius telescope at Cerro Tololo, Chile (Brown 2016). A prediscovery detection on 2016 July 21.26 at 15.5 mag with the same instrumental setup was retrieved via the ASAS-SN light-curve server (Shappee et al. 2014; Kochanek et al. 2017). Fraser et al. (2016) obtained an optical spectrum of SN 2016egz on 2016 July 26.25 with the ESO 3.58 m NTT through PESSTO (Smartt et al. 2015), classifying it as a young SN II at $z = 0.0232 \pm 0.0003$ of the host galaxy, GALEXASC J000403.88-344851.6 (Colless et al. 2003).[1]

---

[1]Via the NASA/IPAC Extragalactic Database (NED)

Given the tight last non-detection limits, we estimate the explosion epochs of SNe 2006Y and 2016egz by simply taking the midpoint of the last non-detection and the first detection with the error being the estimated explosion epoch minus the last non-detection. This yields $MJD_0 = 53766.1 \pm 3.4$ and 57588.2 ± 2.0 for SNe 2006Y and 2016egz, respectively. As there is no constraining last non-detection limit for SN 2006ai, we adopt the explosion epoch estimate $MJD_0 = 53781.6 \pm 5.0$ (~ 1.9 days before the discovery) from the spectral matching technique of Anderson et al. (2014) and Gutiérrez et al. (2017 b). This is reasonable given the early rising light curves (see §3.3). For each SN, we use the explosion epoch as a reference epoch for all phases. We assume a standard Lambda cold dark matter cosmology with $H_0 = 71.0$ km s^{-1} Mpc^{-1}, $\Omega_\Lambda = 0.7$, and $\Omega_m = 0.3$, and convert the redshifts to luminosity distances: $d_L = 146$ Mpc ($\mu = 35.8$ mag), 67.5 Mpc (34.1 mag), and 100 Mpc (35.0 mag), respectively, for SNe 2006Y, 2006ai, and 2016egz.

3.3   Observations and Data Reduction

For SNe 2006Y and 2006ai, *uBgVri* optical and *YJH* NIR photometry were obtained through CSP-I. Standard reduction techniques were applied to all images (e.g., Stritzinger et al. 2011). Then deep template observations obtained once the SN had sufficiently faded from detection were used to subtract the underlying host galaxy emission. Photometry of the SN was computed differentially with respect to a local sequence of stars, together with definitive photometry in the standard *ugri* (Smith et al. 2002), *BV* (Landolt 1992), and *YJH* (Persson et al. 1998) photometric systems, and calibrated to standard star fields observed on photometric nights (see Krisciunas et al. 2017 for a detailed description of the above). The *V*-band light curves presented here are an updated version to those included in the Anderson et al. (2014) sample. CSP-I spectroscopy of SNe 2006Y and 2006ai has already been published in Gutiérrez et al. (2017b), and the reader is referred

to that publication for more details.

For SN 2016egz, LCO *BgVri*-band data were obtained with the SBIG and Sinistro cameras on the network of 1-m telescopes at Sutherland (South Africa), the Cerro Tololo Inter-American Observatory (Chile), and Siding Spring (Australia), through the Supernova Key Project (Howell 2017) and GSP. Using `lcogtsnpipe`, PSF fitting was performed. Reference images were obtained with a Sinistro camera after the SN faded, and image subtraction was performed using `PyZOGY` (Guevel & Hosseinzadeh 2017), an implementation in Python of the subtraction algorithm described in Zackay et al. (2016). *BV*- and *gri*-band data were calibrated to Vega (Stetson 2000) and AB (Albareti et al. 2017) magnitudes, respectively, using standard fields observed on the same night by the same telescope as the SN.

LCO optical spectra for SN 2016egz were taken with the FLOYDS spectrographs mounted on the 2m Faulkes Telescope North (FTN) and South (FTS) at Haleakala (USA) and Siding Spring (Australia), respectively, through the Supernova Key Project and GSP. A 2″0 slit was placed on the target along the parallactic angle. One-dimensional spectra were extracted, reduced, and calibrated following standard procedures using `floyds_pipeline`. Additional optical spectra of the SN and host galaxy were obtained by PESSTO and extended PESSTO (ePESSTO) with NTT (+EFOSC2). EFOSC2 spectra were reduced and calibrated in a standard manner using a custom built pipeline for the PESSTO project (Smartt et al. 2015).

All photometry and spectroscopy of SNe 2006Y, 2006ai, and 2016egz are presented in Figs. 3.1 & 3.2, respectively, and will be available for download via the Open Supernova Catalog and WISeREP. For SNe 2006Y, 2006ai, and 2016egz, no Na I D absorption is seen at the host redshift (Fig. 3.2), indicating low host extinction at the SN position. Thus, we correct all photometry and spectroscopy only for the MW extinction (Schlafly
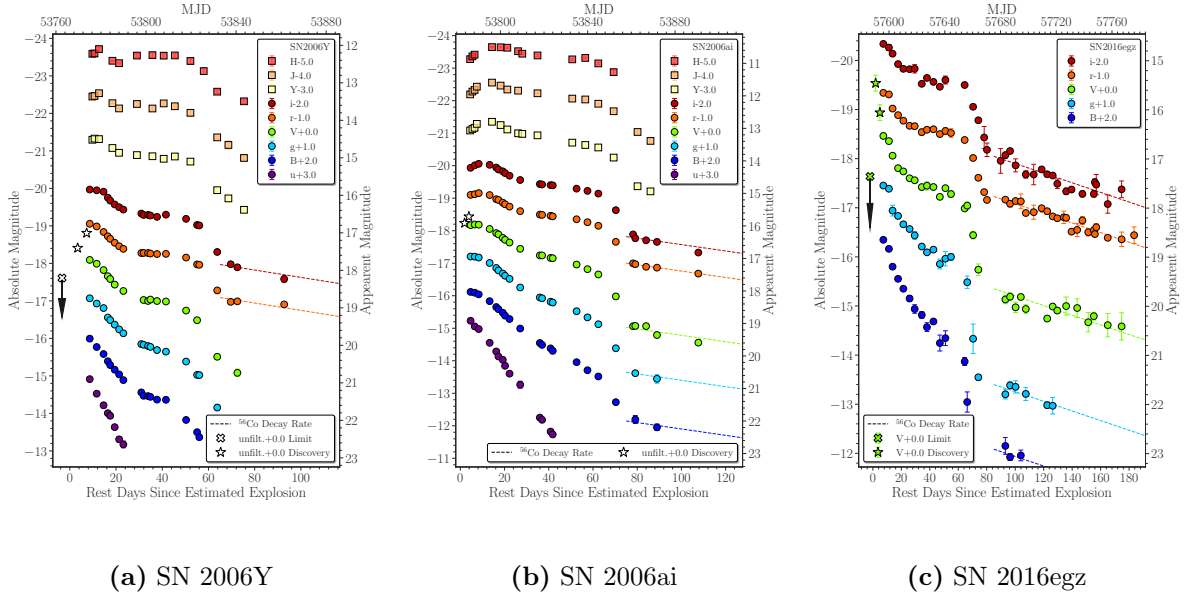
(a) SN 2006Y   **(b)** SN 2006ai   **(c)** SN 2016egz

Figure 3.1: Host-subtracted and extinction-corrected light curves of SNe 2006Y, 2006ai, and 2016egz. Error bars denote 1σ uncertainties and are sometimes smaller than the marker size. Note the similar luminous V-band peaks ($\lesssim -18.2$ mag) and short V-band plateaus (~ 50–70 days). The tail of SN 2006Y is not well sampled, while those of SNe 2006ai and 2016egz are roughly consistent with ^{56}Co decay.

& Finkbeiner 2011)[2] of $A_V = 0.347$, 0.337, and 0.042 mag for SNe 2006Y, 2006ai, and 2016egz, respectively, assuming the Fitzpatrick (1999) reddening law with $R_V = 3.1$.

3.4   Analysis

3.4.1   Host Galaxies

We measure host galaxy line fluxes by fitting a Gaussian profile to each line. In Fig. 3.3, we place the host galaxies in the Baldwin-Phillips-Terlevich (BPT) diagrams (Baldwin et al. 1981) based on the line ratios of [O III] $\lambda5007$/Hβ, [N II] $\lambda6583$/Hα, and [S II] $\lambda6717$/Hα. According to the Kewley et al. (2006) classification scheme, the

---

[2]Via the NASA/IPAC Infrared Science Archive (IRSA)

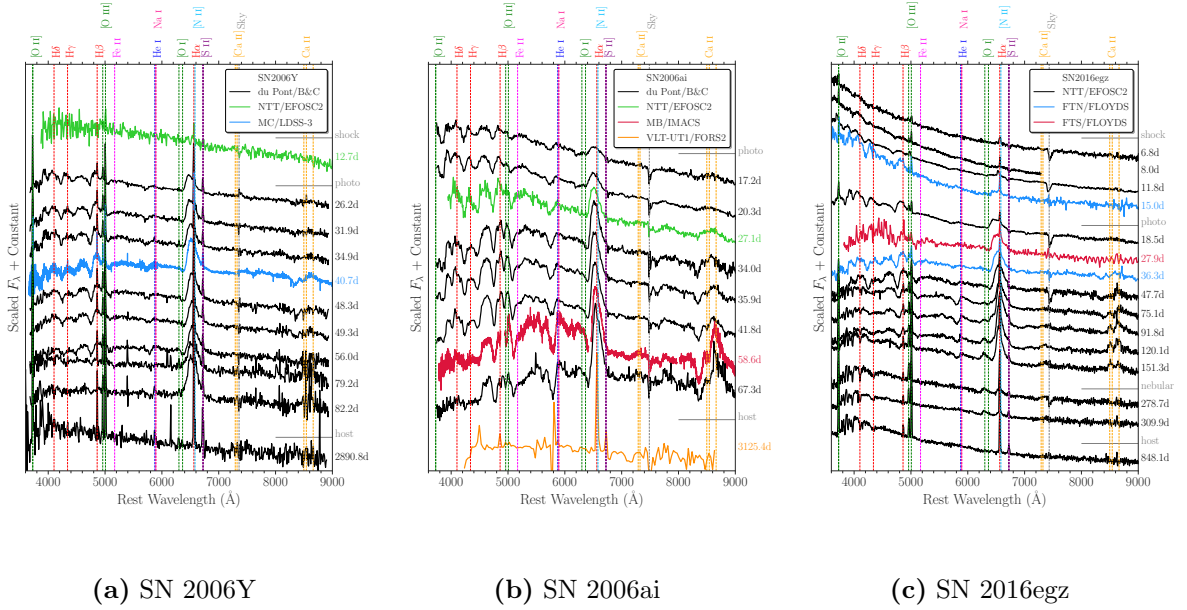**(a)** SN 2006Y   **(b)** SN 2006ai   **(c)** SN 2016egz

Figure 3.2: Extinction-corrected spectral series of SNe 2006Y, 2006ai, and 2016egz. Approximate evolutionary phases are given as: *shock* for shock-cooling phase with a mostly blue featureless continuum; *photo* for optically thick photospheric phase with prominent hydrogen P Cygni features; and *nebular* for optically thin nebular phase with forbidden emission lines (e.g., [O I] $\lambda\lambda6300, 6364$). Note that the narrow emission lines (e.g., Hα and Hβ) and the late-time ($\gtrsim 70\,$d) blue continuum with the 4000 Å break are host contaminants, as seen in the host (i.e., the last) spectra.

host galaxies of SNe 2006Y, 2006ai, and 2016egz lie in the star-forming region in the BPT diagrams. Thus, we estimate SFRs from the Hα and [O II] $\lambda3727$ fluxes using the calibrations summarized in Kennicutt (1998) and from the Galaxy Evolution Explorer (GALEX) photometry (Seibert et al. 2012, retrieved via NED) using the Salim et al. (2007) calibration where the measurements are available. These SFR estimates yield a range of 0.04–0.8 $M_\odot\,\mathrm{yr}^{-1}$. We also estimate host galaxy metallicities from the measured line ratios and various estimates using `PyMCZ` (Bianco et al. 2016). The weighted averages of $12 + \log_{10}(\mathrm{O/H}) = 8.20$–8.71 roughly correspond to 0.3–0.9 $Z_\odot$ (Asplund et al. 2009).

The host galaxies of SNe 2006Y, 2006ai, and 2016egz are star-forming galaxies at subsolar metallicities. They show relatively low [N II]/Hα, [S II]/Hα, and moderate-
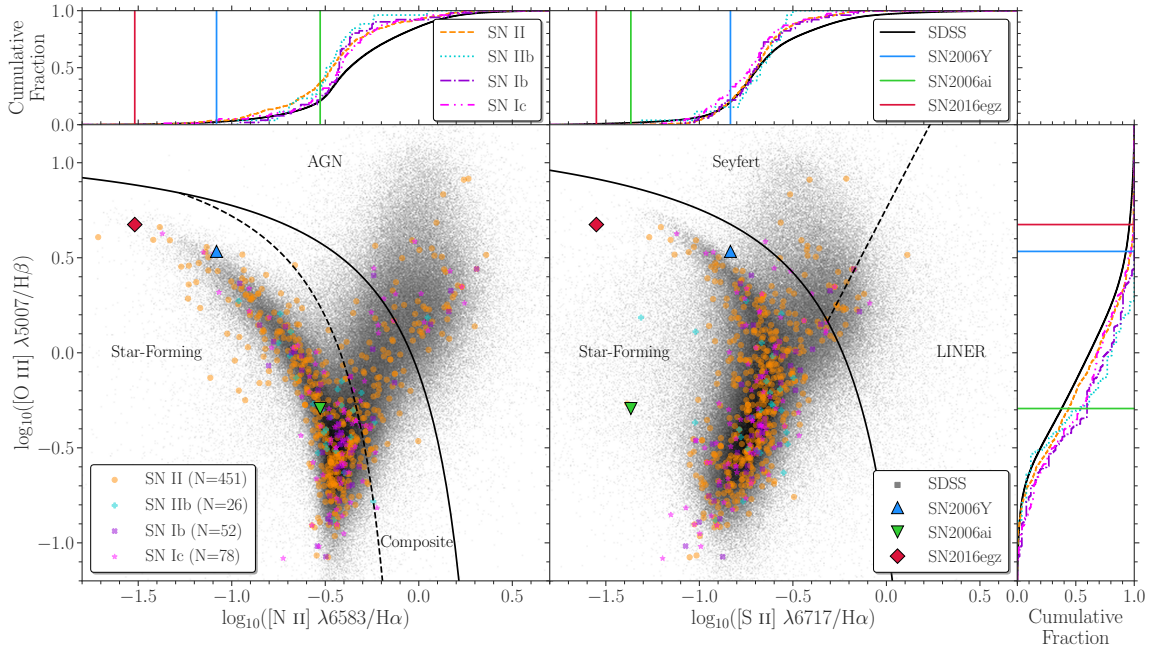
55

Figure 3.3: Comparison of the host galaxy BPT diagrams and cumulative fractions with respect to each axis of SNe 2006Y, 2006ai, and 2016egz with the SN sample of Graham (2019) and the Eighth Data Release of the Sloan Digital Sky Survey (SDSS DR8; Eisenstein et al. 2011; Aihara et al. 2011). The galaxy classification scheme is adopted from Kewley et al. (2006). Note that the host galaxies of SNe 2006Y, 2006ai, and 2016egz lie in the star-forming region with relatively low [N II]/Hα ($\lesssim 21\%$ and $\lesssim 37\%$ of SDSS and SN II host galaxies, respectively), [S II]/Hα ($\lesssim 21\%$ of SDSS and SN II host galaxies), and moderate-to-high [O III]/Hβ ($\lesssim 62\%$ and $\lesssim 56\%$ of SDSS and SN II host galaxies, respectively).

to-high [O III]/Hβ in the BPT comparisons with the SDSS and CCSN host galaxies (Fig. 3.3). Compared to CCSN host galaxy samples, the host SFRs are relatively low ($\lesssim 25\%$ of CCSNe; Galbany et al. 2014), while the host metallicities span a wide range ($\sim 90\%$–100% of CCSNe; Anderson et al. 2016; Galbany et al. 2016a). SNe 2006Y, 2006ai, and 2016egz are also included in the Gutiérrez et al. (2018) SN II sample in low-luminosity host galaxies, in which they find that low-luminosity galaxies generally host SNe II with slower declining light curves and weaker absorption lines, but did not find strong correlations with plateau lengths or expansion velocities. Thus, short-plateau SNe, like 2006Y, 2006ai, and 2016egz, do not seem to have strong environmental preferences,

although this merits future investigations with bigger samples given the rarity of these short-plateau SNe.

3.4.2 V-band and Bolometric Light Curves

We fit a blackbody SED to every epoch of photometry containing at least three filters (excluding the r band owing to strong Hα contamination) obtained within 0.3 days of each other to estimate blackbody temperature and radius.[3] Then we integrate the fitted blackbody SED over the full (and $UBVRI$: 3250–8900Å) wavelength range to obtain bolometric (and pseudobolometric) luminosity at each epoch. Comparing the luminosity on the ^{56}Co tail to that of SN 1987A (Hamuy 2003), we estimate ^{56}Ni masses of $0.062 \pm 0.002\,M_\odot$ and $0.090 \pm 0.005\,M_\odot$ for SNe 2006ai and 2016egz, respectively. Although the tail of SN 2006Y is not well sampled, we put a rough ^{56}Ni mass constraint of 0.06–0.09 $M_\odot$ based on the last V-band point and r- and i-band tail luminosity in between those of SNe 2006ai and 2016egz (Fig. 3.1). These ^{56}Ni mass estimates are among the highest in the Anderson et al. (2014) and Valenti et al. (2016) samples.

The comparisons of the V-band and pseudobolometric light curves of SNe 2006Y, 2006ai, and 2016egz, respectively, with the Anderson et al. (2014) and Valenti et al. (2016) samples are shown in Fig. 3.4. Anderson et al. (2014) include SNe 2006Y and 2006ai in their sample analysis and identify SN 2006Y as an outlier to many observed trends; it shows the fastest decline from the bright maximum followed by the shortest plateau length. The V-band light curves of SNe 2006ai and 2016egz show peak and plateau characteristics similar to SN 2006Y. The similarities stand out even more when their light curves are normalized to peak, showing one of the largest peak-to-tail luminosity contrasts and the shortest (optically thick) photospheric durations (Fig. 3.4(a)). The

---

[3]The observed SED peaks are bluer than our wavelength coverage during the first $\sim$ 10 days for SNe 2006Y, 2006ai, and 2016egz, potentially underestimating the blackbody temperatures.
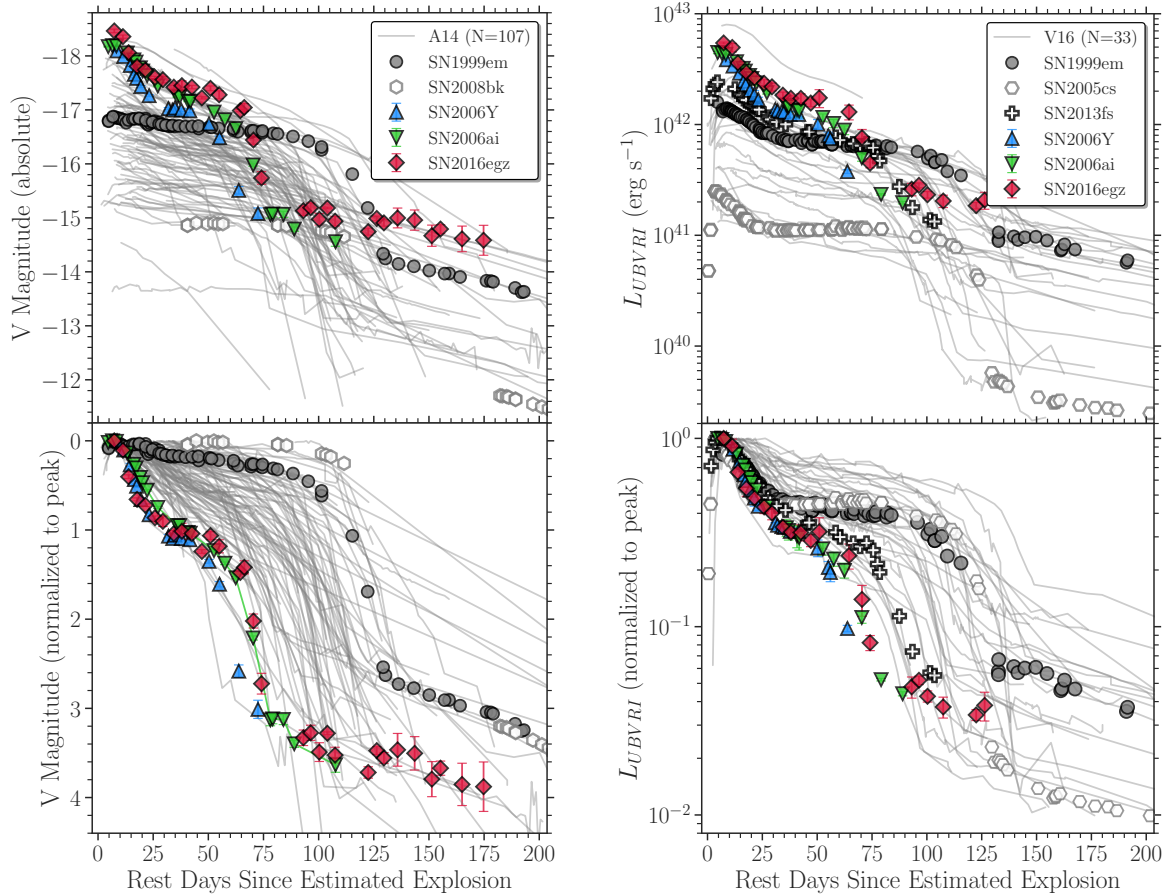
(a) Anderson et al. (2014 A14) sample   **(b)** Valenti et al. (2016 V16) Sample

Figure 3.4: Comparison of the unnormalized (top) and normalized to peak (bottom) light curves of SNe 2006Y, 2006ai, and 2016egz with SN II samples (gray transparent lines), including the archetypal SN IIP 1999em, the low-luminosity SNe IIP 2005cs and 2008bk, and the early-flash SN 2013fs. Error bars denote 1σ uncertainties and are sometimes smaller than the marker size. Note the similar high luminosity and short plateaus of SNe 2006Y, 2006ai, and 2016egz, which could be more pronounced, as their peaks are lower limits (i.e., not observed).

peculiarities of SNe 2006Y and 2016egz could be even more extreme (compared to *normal* SN II population), given that their light-curve peaks are lower limits (not observed).

The similar characteristics can also be seen in the pseudobolometric light-curve comparison in Fig. 3.4(b). In addition, the peaks and the following decline rates of SNe 2006Y, 2006ai, and 2016egz are brighter and steeper, respectively, than those of SN 2013fs (Yaron et al. 2017) whose early time ($\lesssim 5\,\mathrm{d}$) spectra show *flash features* (high-ionization CSM emission lines excited by the SN shock-breakout radiation; Gal-Yam et al. 2014; Khazov et al. 2016; Bruch et al. 2021). Various flash spectral and light-curve modeling have inferred high mass-loss rates for SN 2013fs, ranging from ~ 0.001–$0.1\,M_\odot\,\mathrm{yr}^{-1}$ for the last few years to decades before the explosion (e.g., Moriya et al. 2017; Morozova et al. 2017; Yaron et al. 2017, but see also Dessart et al. 2017; Soker 2021 and Kochanek 2019 for the possible alternatives from an extended envelope and binary interaction, respectively). Thus, the brighter and steeper peaks of SNe 2006Y, 2006ai, and 2016egz likely indicate the presence of similar or even denser CSM. However, we still do not see flash features, probably because the SN ejecta had already overrun the CSM by the time of our first spectra (Fig. 3.2).

As first-order estimates for progenitor and explosion properties, we use the SN IIP light-curve scaling relations of Goldberg et al. (2019) that give degenerate parameter space for progenitor radius, ejecta mass (M_{ej}), and explosion energy (E_{exp}) based on the observed luminosity at day 50, plateau duration, and ^{56}Ni mass. We caution that these relations are not calibrated to short-plateau SNe, such as SNe 2006Y, 2006ai, and 2016egz, whose light curves start to drop from the plateaus around day 50, but nonetheless they should provide some crude estimates. The extra heating from ^{56}Ni extends plateau duration, but it is not the lack of ^{56}Ni that causes the short plateaus of SNe 2006Y, 2006ai, and 2016egz, given their high ^{56}Ni mass estimates. If we assume a typical RSG radius of $800\,R_\odot$, then H-rich $M_{\mathrm{ej}} \sim 1$, 2, and $4\,M_\odot$ and $E_{\mathrm{exp}} \sim 0.3, 0.4, 0.8 \times 10^{51}\,\mathrm{erg}$

can be inferred, respectively, for SNe 2006Y, 2006ai, and 2016egz from the light-curve scaling relations. This suggests significant progenitor H-rich envelope stripping.

3.4.3   MESA+STELLA Progenitor and Light-curve Modeling

In order to explore the effect of H-rich envelope stripping in SN II light curves in more detail and to better extract physical parameters from the short-plateau light curves, we construct a large MESA+STELLA single-star progenitor and light-curve model grid. For the MESA progenitor model grid, we vary ZAMS masses ($M_{\mathrm{ZAMS}} = 10.0$–$25.0\,M_\odot$ with $2.5\,M_\odot$ increments) and wind scaling factors ($\eta_{\mathrm{wind}} = 0.0$–$3.0$ with 0.1 increments), while fixing subsolar ZAMS metallicity ($Z = 0.3\,Z_\odot$) and no rotation ($\nu/\nu_{\mathrm{crit}} = 0$). For the MESA explosion model grid, we vary explosion energies ($E_{\mathrm{exp}} = 0.4$–$2.0 \times 10^{51}\,\mathrm{erg}$ with $0.2 \times 10^{51}\,\mathrm{erg}$ increments) and ^{56}Ni masses ($M_{\mathrm{Ni}} = 0.04$, 0.07, and $0.1\,M_\odot$) for each progenitor model. Then we hand off these explosion models to STELLA to produce synthetic light curves and expansion velocities. A more detailed description of the model grid is presented in Appendix 3.6.1.

The full light-curve model grid with $M_{\mathrm{Ni}} = 0.07\,M_\odot$ (totaling 1,303 models)[4] is shown in Fig. 3.5. This shows SN II subtypes as part of a continuous population, delineated by their H-rich envelope mass ($M_{\mathrm{H_{env}}}$; we use the 20% mass fraction point $X(\mathrm{H}) \geq 0.2$).[5] Short-plateau SNe represent a transitional class between SNe IIL and IIb in a narrow $M_{\mathrm{H_{env}}}$ window ($\Delta M_{\mathrm{H_{env}}} \sim 1.2\,M_\odot$). This is likely why these short-plateau SNe are so rare. The SN II plateau slope correlations with the maximum brightness and plateau duration (e.g., Anderson et al. 2014; Sanders et al. 2015; Galbany et al. 2016b; Valenti et al. 2016) are also naturally reproduced with some scatter by varying $M_{\mathrm{H_{env}}}$ and E_{exp}.

---

[4]The full light-curve model grids with $M_{\mathrm{Ni}} = 0.04\,M_\odot$ (1,301 models) and $0.1\,M_\odot$ (1,306 models) are shown in Figs. 3.15 & 3.16, respectively, displaying an SN II population trend similar to that of the $M_{\mathrm{Ni}} = 0.07\,M_\odot$ grid, albeit with varying plateau duration and tail luminosity.

[5]The general SN II population trend is independent of the particular choice of mass fraction point, i.e., $X(\mathrm{H}) = 0.1$ and 0.5 show a similar trend, albeit with different $M_{\mathrm{H_{env}}}$ cuts.

(a) IIP $(4.5\,M_\odot \leq M_{\mathrm{H_{env}}} \leq 15.8\,M_\odot)$

(b) IIL $(2.12\,M_\odot \leq M_{\mathrm{H_{env}}} \leq 4.5\,M_\odot)$

(c) Short-Plateau $(0.91\,M_\odot \leq M_{\mathrm{H_{env}}} \leq 2.12\,M_\odot)$

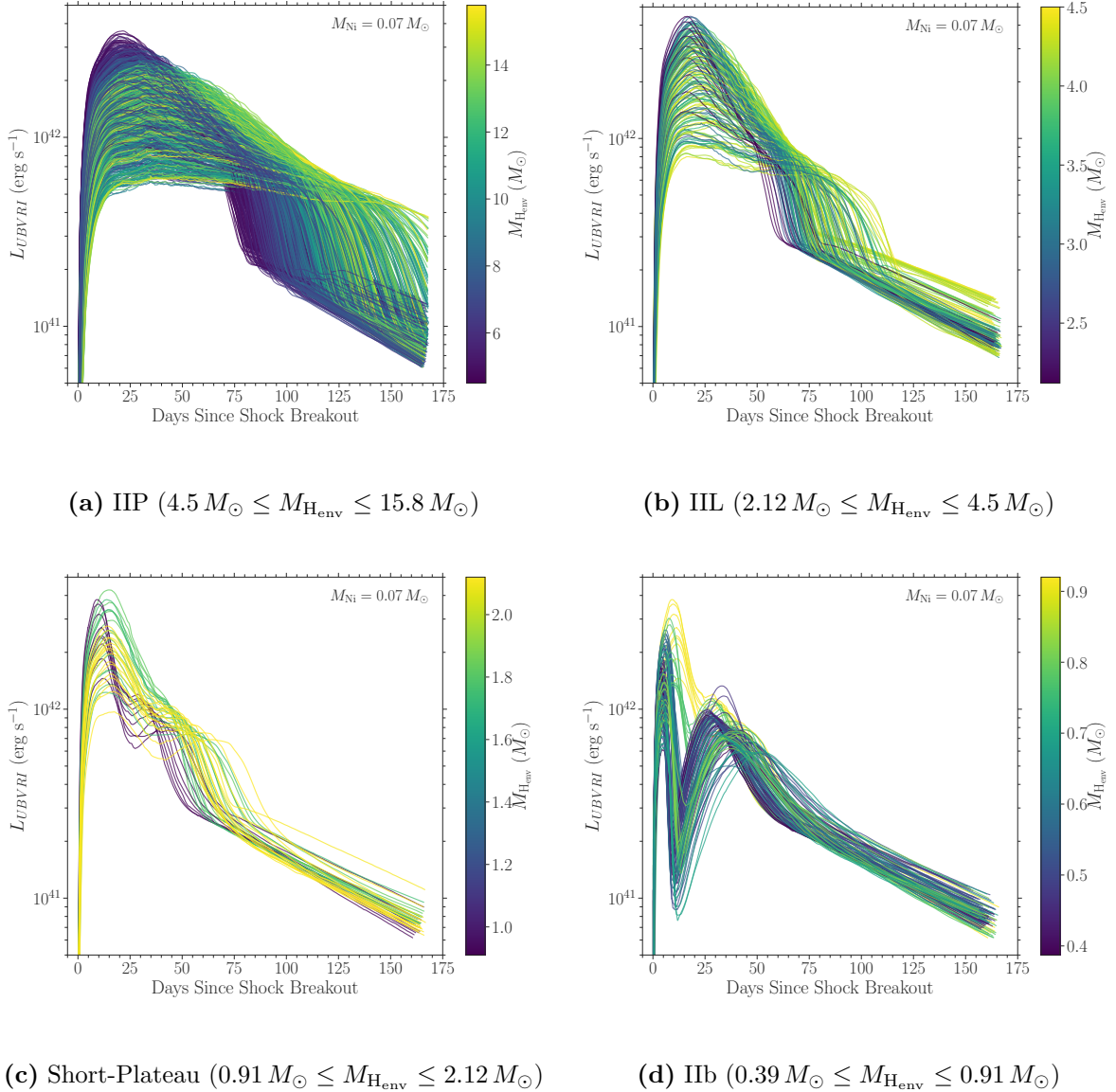**(d)** IIb $(0.39\,M_\odot \leq M_{\mathrm{H_{env}}} \leq 0.91\,M_\odot)$

Figure 3.5: `MESA+STELLA` pseudobolometric light-curve models with a single ^{56}Ni mass ($M_{\mathrm{Ni}} = 0.07\,M_\odot$), color coded by the H-rich envelope mass ($M_{\mathrm{H_{env}}}$) at the core collapse. Arbitrary cuts in $M_{\mathrm{H_{env}}}$ are applied to display each SN II subtype in each panel. Light curves with the same color in each panel come from the same progenitor model exploded with different energies (E_{exp}); higher E_{exp} result in brighter, steeper, and shorter photospheric-phase light curves. Note the continuous population of SNe IIP–IIL–short-plateau–IIb in descending order of $M_{\mathrm{H_{env}}}$ and the narrow $M_{\mathrm{H_{env}}}$ window that results in short-plateau SNe.

As the population is rather continuous, the applied $M_{\mathrm{H_{env}}}$ cuts are somewhat arbitrary and mainly for presentation purposes.

In order to demonstrate the effect of ^{56}Ni heating on the SN II light curves, we use a finer M_{Ni} grid spacing (0.00–0.10 $M_\odot$ with 0.01 $M_\odot$ increments) for a representative model of each SN II subtype and show their light curves in Fig. 3.6. The early phase is M_{Ni} independent, as it is powered by shock cooling. For the SN IIP/L models, the extra heating from ^{56}Ni extends the photospheric-phase duration (Kasen & Woosley 2009; Goldberg et al. 2019; Kozyreva et al. 2019), but does not affect the overall IIP/L light-curve morphology. For the short-plateau SN models, on the other hand, the *plateau* phase is dominantly powered by ^{56}Ni heating (unlike those of the SN IIP models, but rather similar to the second peak of the SN IIb models), and the light curves result in IIL morphology with lower M_{Ni} ($\lesssim 0.05\,M_\odot$). This suggests the high M_{Ni} preference of short-plateau SNe.

Using the Binary Population and Spectral Synthesis Version 2 (`BPASS` v2; Eldridge et al. 2017) and the SuperNova Explosion Code (`SNEC`; Morozova et al. 2015) with a single $E_{\mathrm{exp}} = 10^{51}$ erg and $M_{\mathrm{Ni}} = 0.05\,M_\odot$, Eldridge et al. (2018) show a similar SN II population trend with respect to the total progenitor hydrogen mass (M_{H}) and note the small population of short-plateau SNe ($\sim 4.7\%$ of all SNe II). They find a lower M_{H} range for SNe IIL (0.003–0.7 $M_\odot$) than short-plateau (0.3–2.0 $M_\odot$), compared to our model grid of SNe IIL (1.3–3.1 $M_\odot$) and short-plateau (0.45–1.3 $M_\odot$). But we do not consider this as a serious conflict as the subtype classifications are again ambiguous and also sensitive to other physical parameters (e.g., E_{exp} and M_{Ni} as shown in Figures. 3.5 and 3.6). A more detailed analyses of our `MESA+STELLA` model grid and its comparisons to observed SN II samples will be presented in a future publication (Hiramatsu et al., in prep.). In this work, we focus on its application to short-plateau SNe.

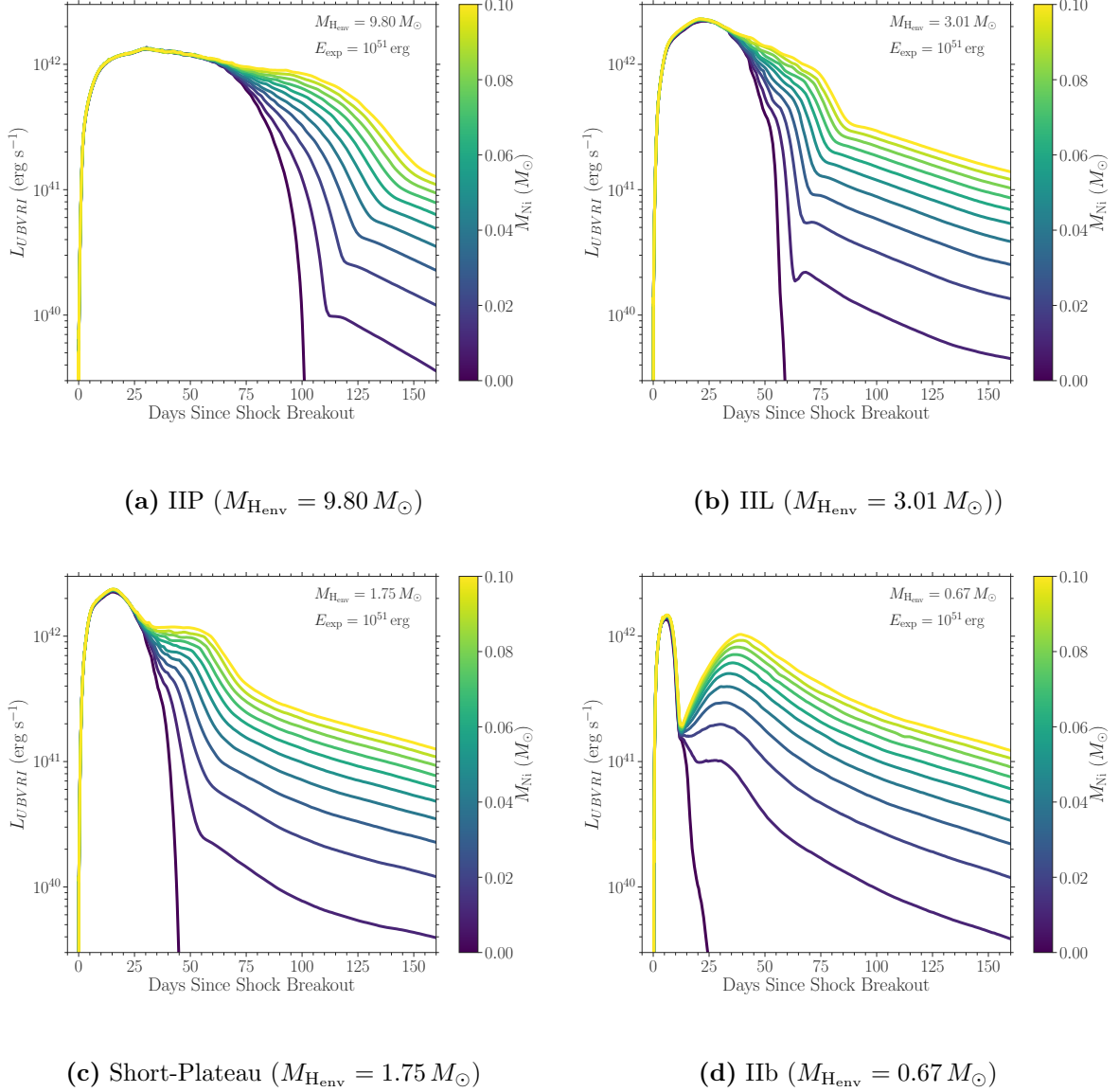The short-plateau SN models come from massive progenitors ($M_{\mathrm{ZAMS}} \geq 17.5\,M_\odot$)

(a) IIP ($M_{\mathrm{H_{env}}} = 9.80\,M_{\odot}$)

(b) IIL ($M_{\mathrm{H_{env}}} = 3.01\,M_{\odot}$))

(c) Short-Plateau ($M_{\mathrm{H_{env}}} = 1.75\,M_{\odot}$)

(d) IIb ($M_{\mathrm{H_{env}}} = 0.67\,M_{\odot}$)

Figure 3.6: `MESA+STELLA` pseudobolometric light-curve models with a single explosion energy ($E_{\mathrm{exp}} = 10^{51}\,\mathrm{erg}$) from a representative progenitor model of each SN II subtype, color coded by the ^{56}Ni mass (M_{Ni}). The initial shock-cooling phase is M_{Ni} independent, while the following photospheric phase is M_{Ni} dependent. Note that in the short-plateau $M_{\mathrm{H_{env}}}$ range, the light curves also span IIL morphology with a lower M_{Ni} ($\lesssim 0.05\,M_{\odot}$).

with strong wind mass loss ($\eta_{\text{wind}} \geq 1.2$) stripping significant amounts of the H-rich envelope ($\gtrsim 9\,M_\odot$). We caution that this could partially be due to a modeling bias as the wind mass loss is more sensitive to the choice of η_{wind} for more massive progenitors. But we also note that $15.0\,M_\odot$ progenitors within the short-plateau $M_{\text{H}_{\text{env}}}$ range (modeled with $\eta_{\text{wind}} = 3.4$; not included in the grid) do not result in short-plateau SNe, but IIL, even with $M_{\text{Ni}} = 0.1\,M_\odot$. With binary interactions, Eldridge et al. (2018) find a wider M_{ZAMS} range (7–25 $M_\odot$) for short-plateau SNe. Thus, it is useful to have independent means of estimating M_{ZAMS} for cross checking (e.g., direct progenitor identification and nebular spectra; see §3.4.6 for nebular spectral analysis).

For SNe 2006Y, 2006ai, and 2016egz, we perform χ^2 fitting on the observed pseudobolometric light curves with our model grid. In Fig. 3.7, we show the resultant model-grid log likelihood distributions of E_{exp} and the progenitor properties at the core collapse: $M_{\text{H}_{\text{env}}}$, total mass ($M_{\text{tot}}$), and photospheric radius (R_{ph}), along with the best-fit light-curve models and the maximum likelihood parameters. The parameter choices are based on SNe IIP light-curve scaling relations (Popov 1993; Kasen & Woosley 2009; Sukhbold et al. 2016; Goldberg et al. 2019). But we split the mass parameter into two components: $M_{\text{H}_{\text{env}}}$ and M_{tot} to estimate He-core mass ($M_{\text{He}_{\text{core}}} = M_{\text{tot}} - M_{\text{H}_{\text{env}}}$) and then to translate $M_{\text{He}_{\text{core}}}$ to M_{ZAMS}. As we control H-rich envelope stripping by arbitrarily varying η_{wind}, there is no one-to-one relationship between M_{tot} and M_{ZAMS}. Thus, $M_{\text{He}_{\text{core}}}$–$M_{\text{ZAMS}}$ relation is more reliable as it is less sensitive to H-rich envelope stripping and metallicity for $M_{\text{ZAMS}} \lesssim 30\,M_\odot$ (Woosley & Weaver 1995; Woosley et al. 2002), although binary interaction may alter the relation (e.g., Zapartas et al. 2019, 2021).

Overall, the observed short-plateau light curves of SNe 2006Y, 2006ai, and 2016egz are reasonably well reproduced by the models with $M_{\text{H}_{\text{env}}} \simeq 1.7\,M_\odot$, $M_{\text{tot}} \simeq 7.1$–$8.5\,M_\odot$, $R_{\text{ph}} \simeq 480$–$580\,R_\odot$, and $E_{\text{exp}} \simeq 0.8$–$2.0 \times 10^{51}$ erg. We also note that there exists some parameter degeneracy (Dessart & Hillier 2019; Goldberg et al. 2019; Goldberg & Bildsten

(a) SN 2006Y
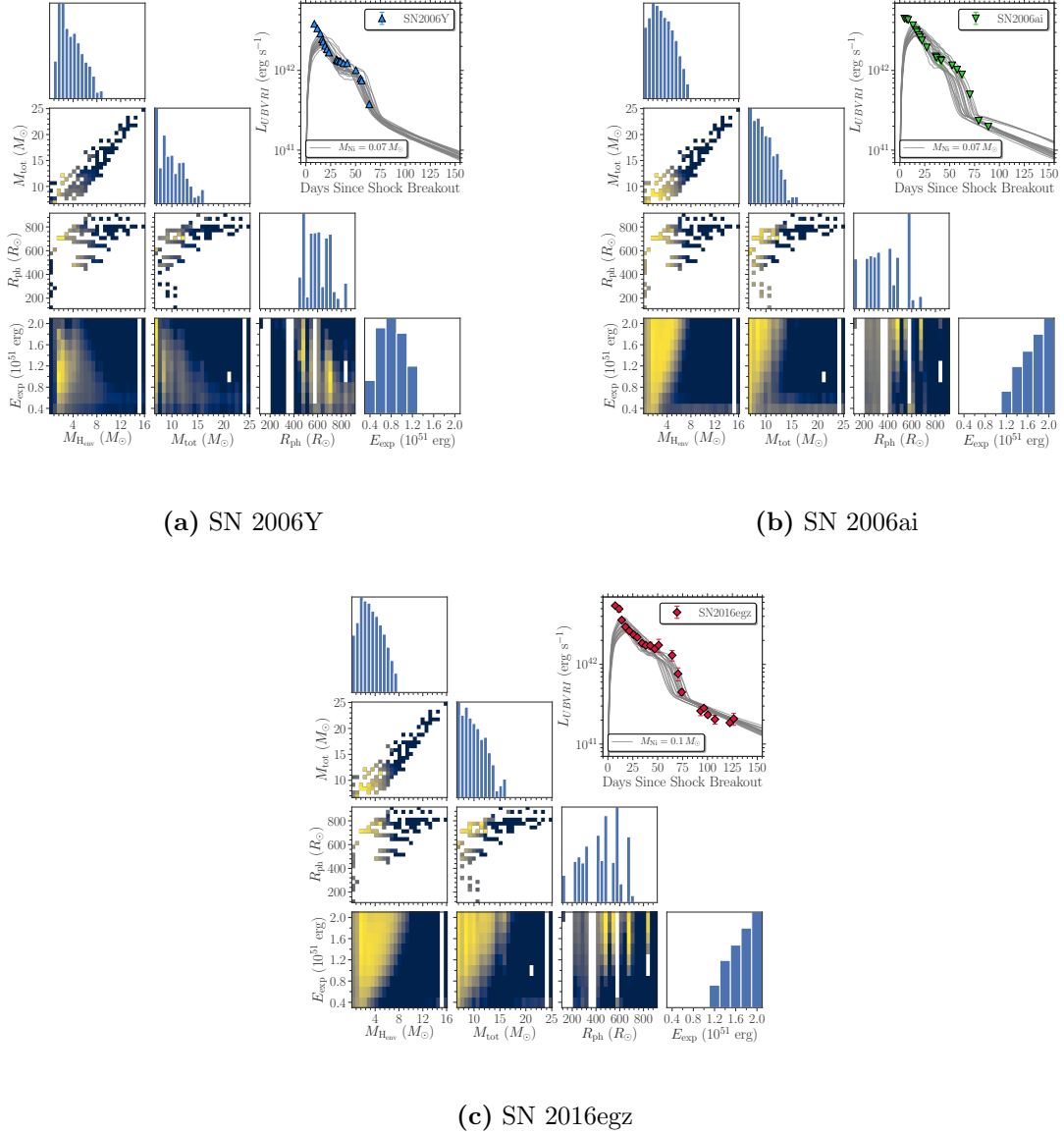

(b) SN 2006ai

(c) SN 2016egz

Figure 3.7: Model-grid log likelihood distributions of the explosion energy (E_{exp}) and the progenitor properties at the core collapse: H-rich envelope mass ($M_{\mathrm{H_{env}}}$), total mass (M_{tot}), and photospheric radius (R_{ph}), along with the 20 best-fit light-curve models and the maximum likelihood parameters. In the 2D correlation plots, the brighter yellow regions correspond to the higher correlations, while the blank space corresponds to the parameter space that is not covered by the model grid. The $M_{\mathrm{Ni}} = 0.07\,M_\odot$ grid is used to fit SNe 2006Y and 2006ai, while the $M_{\mathrm{Ni}} = 0.1\,M_\odot$ grid is used to fit SN 2016egz. The overall light-curve morphology is reasonably well reproduced, except the early ($\lesssim 10$ days) excess emission, which we attribute to CSM interaction (Figs. 3.8 & 3.9). Note the inferred small $M_{\mathrm{H_{env}}}$ and high He-core masses ($M_{\mathrm{He_{core}}} = M_{\mathrm{tot}} - M_{\mathrm{H_{env}}}$) of 5.4–6.9 $M_\odot$ for SNe 2006Y, 2006ai, and 2016egz.

2020). Using the $M_{\mathrm{He_{core}}}$–M_{ZAMS} relation from the Sukhbold et al. (2016) model grid, we translate $M_{\mathrm{He_{core}}} \simeq 5.4$–$6.9\,M_\odot$ to $M_{\mathrm{ZAMS}} \simeq 18$–$22\,M_\odot$. This suggests partially stripped massive progenitors. Finally, we note that the observed early ($\lesssim 10$ days) emission of SNe 2006Y, 2006ai, and 2016egz are underestimated by the models, indicating the presence of an additional power source to pure shock-cooling emission from the bare stellar atmosphere.

3.4.4   `MESA+STELLA` CSM Light-curve Modeling

In order to account for the early excess emission, we propose CSM interaction as a possible power source, as suggested in §3.4.2. At handoff to `STELLA`, we affix a wind density profile with $\rho_{\mathrm{wind}}(r) = \dot{M}_{\mathrm{wind}}/4\pi r^2 v_{\mathrm{wind}}$, where $\dot{M}_{\mathrm{wind}}$ is a constant wind mass-loss rate, and v_{wind} is the wind velocity for time t_{wind} (i.e., the CSM mass, $M_{\mathrm{CSM}} = \dot{M}_{\mathrm{wind}} t_{\mathrm{wind}}$), onto the subset of `MESA` explosion models that result in short-plateau SNe (40 models each with $M_{\mathrm{Ni}} = 0.04$, 0.07, and $0.1\,M_\odot$; Figs. 3.5(c), 3.15(c), & 3.16(c)). In addition to the 400 spatial zones for the original SN ejecta, we use 200 spatial zones for the CSM model in `STELLA`. We construct a grid of CSM models by varying $\dot{M}_{\mathrm{wind}}$ (10^{-5}–$10^{-1}\,M_\odot\,\mathrm{yr}^{-1}$ with 0.5 dex increments) and t_{wind} (10 and 30 yr) for each `MESA` short-plateau SN model, assuming a typical RSG $v_{\mathrm{wind}} = 10\,\mathrm{km\,s}^{-1}$ (Moriya et al. 2011). The subset of the CSM light-curve model grid is shown in Fig. 3.8 where the effect of increasing CSM mass on the light-curve luminosity and shape can be seen.

In Fig. 3.9, we show the CSM model-grid log likelihood distributions of M_{CSM} and E_{exp} from χ^2 fitting on SNe 2006Y, 2006ai, and 2016egz. The observed early excess emission as well as the overall light curves of SNe 2006Y, 2006ai, and 2016egz are reasonably well reproduced by the CSM models with $M_{\mathrm{CSM}} \simeq 0.1$–$0.3\,M_\odot$ ($\dot{M}_{\mathrm{wind}} \simeq 10^{-2}\,M_\odot\,\mathrm{yr}^{-1}$ with $t_{\mathrm{wind}} = 10$ yr for SN 2006Y and 30 yr for SNe 2006ai and 2016egz) and $E_{\mathrm{exp}} \simeq 1.0$–
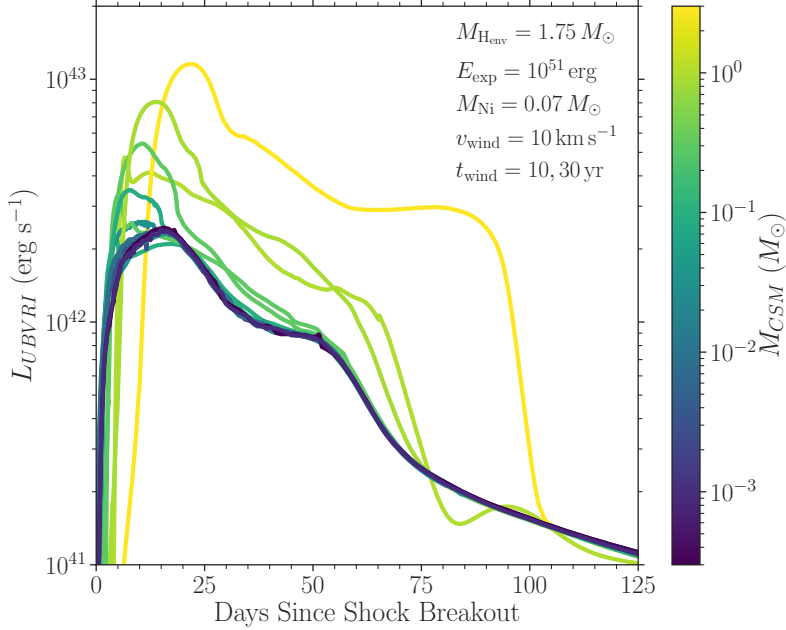
Figure 3.8: Subset of MESA+STELLA pseudobolometric CSM light-curve models with the single wind velocity (v_{wind}) and two different mass-loss duration (t_{wind}), color coded by the CSM mass ($M_{\mathrm{CSM}} = \dot{M}_{\mathrm{wind}} t_{\mathrm{wind}}$). Light curves with the same color come from different combinations of $\dot{M}_{\mathrm{wind}}$ and t_{wind} that result in the same M_{CSM}; higher $\dot{M}_{\mathrm{wind}}$ and lower t_{wind} result in sharper light-curve peaks. Note the effect of CSM interaction on both the luminosity and shape.

$1.4 \times 10^{51}\,\mathrm{erg}$. This suggests enhanced mass loss (a few orders of magnitude greater than the standard continuous $\dot{M}_{\mathrm{wind}} \sim 10^{-5}\,M_\odot\,\mathrm{yr}^{-1}$) in the last few decades before the explosion. The inferred E_{exp} are generally lower than those from the CSM-free fits (Fig. 3.7) since the CSM interaction provides additional luminosity, especially around the peak. The actual CSM could be even denser and more confined for SNe 2006Y, 2006ai, and 2016egz because their light-curve peaks are lower limits.

3.4.5   Photospheric Spectra

As in the Anderson et al. (2014) sample light-curve analysis, Gutiérrez et al. (2014, 2017b,c) also include SNe 2006Y and 2006ai in their sample spectral analysis and identify their spectral peculiarity, namely, the smallest Hα P Cygni absorption to emission ratios (a/e). They also find a correlation between a/e and light-curve plateau slope (i.e., SNe
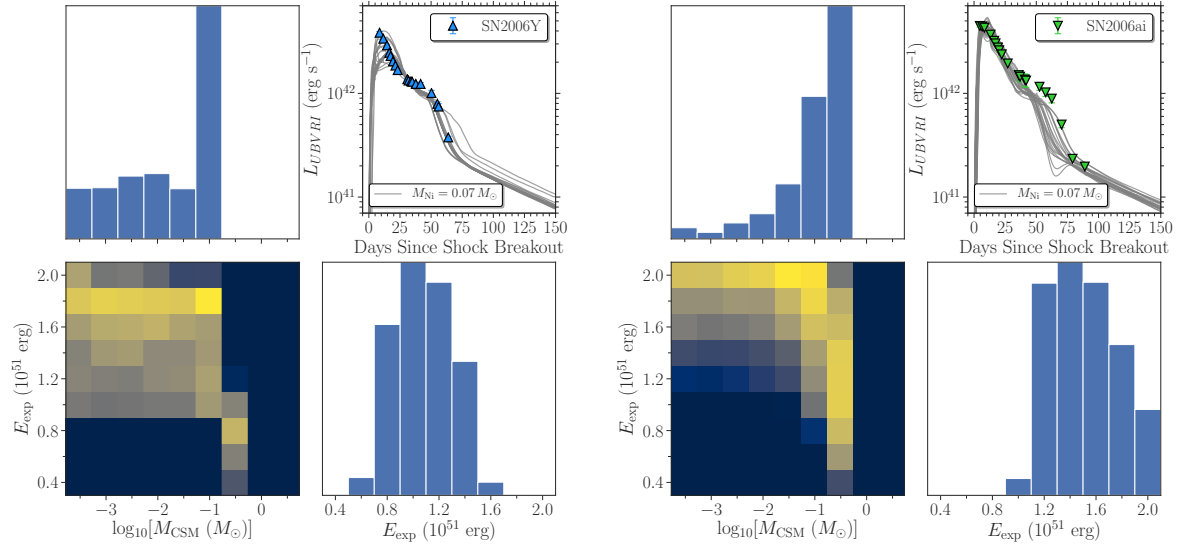
(a) SN 2006Y

(b) SN 2006ai
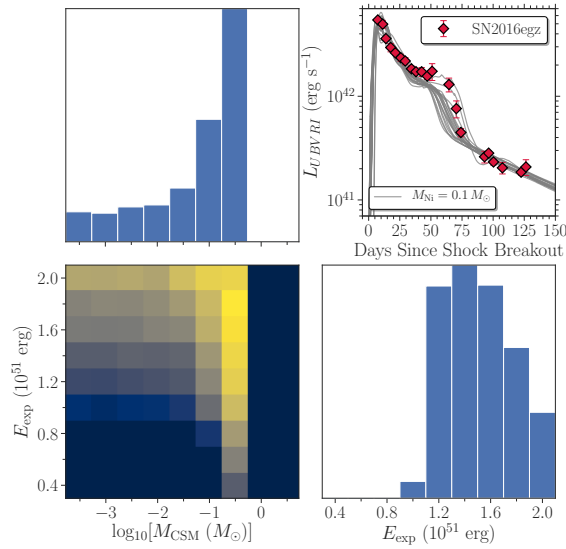
(c) SN 2016egz

Figure 3.9: Similar to Fig. 3.7, but with the CSM models. The early ($\lesssim 10$ days) excess emission are reasonably well reproduced. Note the inferred smaller E_{exp} compared to the CSM-free fits in general, and the large M_{CSM} that suggest violent mass loss in the last few decades before the explosion (actual M_{CSM} could be even higher as the light-curve peaks are lower limits).
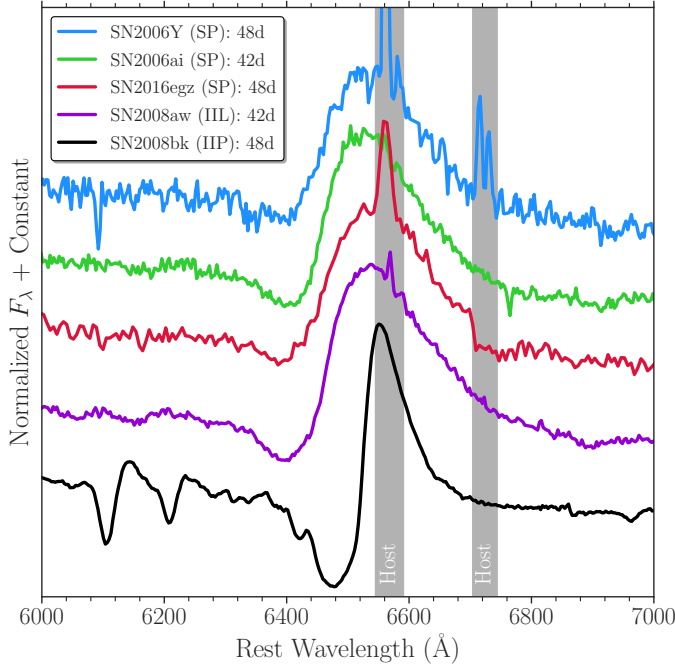
Figure 3.10: Comparison of the Hα P Cygni profiles of short–plateau (SP) SNe 2006Y, 2006ai and 2016egz with the SN IIL 2008aw and the SN IIP 2008bk around 50 days after explosion (Gutiérrez et al. 2014, 2017b), retrieved via the Open Supernova Catalog. The gray shaded regions represent host galaxy contamination. Each spectrum is normalized by its broad SN Hα peak. Note that the Hα P Cygni absorption to emission ratios of SNe 2006Y, 2006ai and 2016egz are smaller than those of the SN IIP 2008bk and even the SN IIL 2008aw.

IIL have shallower absorption components than SNe IIP). Several possible explanations for the smaller a/e for SNe IIL have been proposed, e.g., lower $M_{H_{env}}$ (Schlegel 1996; Gutiérrez et al. 2014, 2017c) and steeper envelope density gradients (Dessart & Hillier 2005; Dessart et al. 2013; Gutiérrez et al. 2014). In Fig. 3.10, we show the Hα P Cygni profile comparison of SNe 2006Y, 2006ai, and 2016egz with SNe IIL and IIP. SN 2016egz displays a Hα P Cygni profile similar to that of SNe 2006Y and 2006ai with a shallower absorption feature than SNe IIL and IIP. This supports lower $M_{H_{env}}$ as a possible cause of smaller a/e since short-plateau SNe with lower $M_{H_{env}}$ result in smaller a/e than SNe IIP and IIL, as seen in our MESA+STELLA light-curve model grid (Fig. 3.5).

For SNe 2006Y, 2006ai, and 2016egz, we measure expansion velocities of Fe II $\lambda 5169$ from the absorption minimum by fitting a P Cygni profile. In Fig. 3.11, we show the velocity comparison of SNe 2006Y, 2006ai, and 2016egz with the MESA+STELLA short-plateau SN models with $M_{Ni} = 0.07\,M_\odot$ (Fig. 3.5(c)),[6] as well as the mean velocity

---

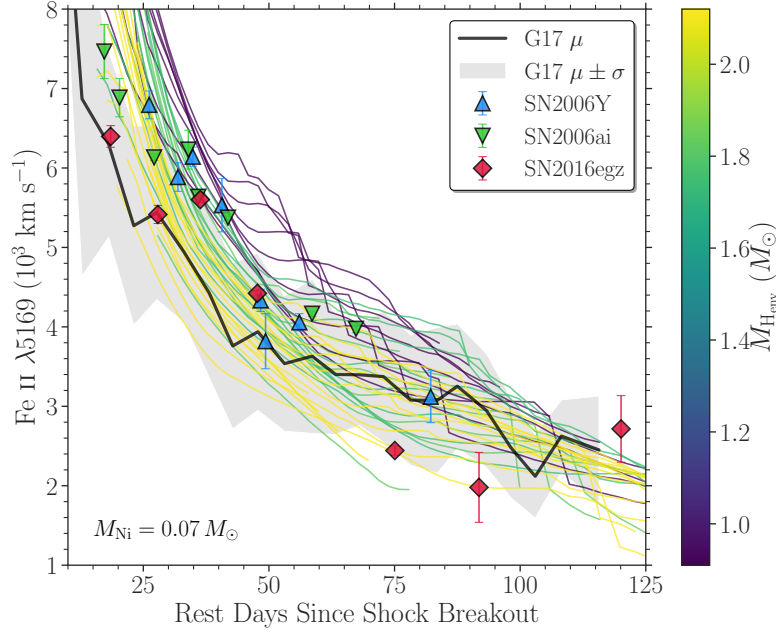[6]The short-plateau SN models with $M_{Ni} = 0.04$ and $0.1\,M_\odot$ are shown in Fig. 3.17, displaying a

Figure 3.11: Comparison of Fe II $\lambda 5169$ velocities of SNe 2006Y, 2006ai, and 2016egz with the Gutiérrez et al. (2017b G17) mean velocity evolution (black line and gray shaded region) and `MESA+STELLA` short-plateau SN models with $M_{\mathrm{Ni}} = 0.07 \, M_\odot$ (defined by the Sobolev optical depth $\tau_{\mathrm{Sob}} = 1$), color coded by $M_{\mathrm{H_{env}}}$ as in Fig. 3.5(c). Error bars denote 1σ uncertainties and are sometimes smaller than the marker size. Velocity models with the same color come from the same progenitor model exploded with different energies; higher explosion energies result in faster velocities. Note the better agreements with the higher $M_{\mathrm{H_{env}}}$ models for SNe 2006Y, 2006ai, and 2016egz.

evolution from the Gutiérrez et al. (2017b) SN II sample. The overall velocity evolution is better reproduced with the higher $M_{\mathrm{H_{env}}}$ ($\gtrsim 1.7 \, M_\odot$) models. This is in agreement with the values inferred from the light-curve fitting (Fig. 3.7). The Fe II $\lambda 5169$ velocities of SNe 2006Y, 2006ai, and 2016egz are generally higher than the Gutiérrez et al. (2017 b) mean velocity evolution, but still within 1σ deviation. Thus, unlike their light curves, their velocities do not appear to be outliers.

However, it is worth noting that the velocity of SN 2016egz is lower than those of SNe 2006Y and 2006ai, despite it exhibiting a more luminous light curve (Fig. 3.4).

velocity evolution similar to that of the $M_{\mathrm{Ni}} = 0.07 \, M_\odot$ models, albeit with varying late-time evolution.

This is in disagreement with the SN IIP luminosity–velocity correlation ($L_P \propto v_P^2$) from the homologously expanding photosphere set by H-recombination (Hamuy & Pinto 2002; Kasen & Woosley 2009; Goldberg et al. 2019). By comparing the light curves (Fig. 3.5(c)) and velocities (Fig. 3.11) of short-plateau SN models, we do not see an obvious L_P–v_P correlation (e.g., some of the highest and lowest $M_{\mathrm{H_{env}}}$ models have similar L_P, but the highest $M_{\mathrm{H_{env}}}$ models have systematically lower v_P). This suggests that the short-plateau light curves are not purely powered by shock energy released at the H-recombination front; ^{56}Ni heating is also important in shaping their light curves (more so than in typical SN IIP light curves). This is in agreement with the light-curve analysis with varying M_{Ni} (Fig. 3.6(c)).

Finally, we note that both line shape and velocity could also be affected by the extra emission from persistent CSM interaction (e.g, Moriya et al. 2011, 2018a; Dessart et al. 2016a; Hillier & Dessart 2019), even though high-velocity Hα absorption features are absent (Chugai et al. 2007). Thus, the qualitative analyses, partially based on the light-curve modeling, in this section merit future spectral modeling of short-plateau SNe with and without CSM interaction.

3.4.6   Nebular Spectra

While there are no late-time ($> 100\,\mathrm{d}$) spectra available for SNe 2006Y and 2006ai, we obtained two nebular-phase ($> 200\,\mathrm{d}$) spectra for SN 2016egz (Fig. 3.2). We simultaneously fit a Gaussian profile to the broad SN Hα (excluding the narrow host Hα region) and a double-Gaussian profile to [O I] $\lambda\lambda6300, 6364$ assuming a doublet flux ratio of 3:1 (as not resolved) and single FWHM velocity. These fits give Hα and [O I] FWHM velocity ranges of $3{,}000$–$4{,}000\,\mathrm{km\,s^{-1}}$ and $3{,}400$–$3{,}700\,\mathrm{km\,s^{-1}}$, respectively. Due to the low signal-to-noise ratio (S/N) and fringing, we are unable to measure [Ca II] $\lambda\lambda7291, 7323$

fluxes. Instead, we inject a double-Gaussian profile at the [Ca II] rest wavelengths by assuming a doublet flux ratio of 1:1 and the same single FWHM velocity as the [O I] doublet at each epoch to place a 3σ flux upper limit.

It is known that [O I] and its ratio to [Ca II] are insensitive respectively to the SN explosive nucleosynthesis and the SN ejecta density and temperature, so can be used as a proxy for progenitor O-core mass, and so ZAMS mass (e.g., Fransson & Chevalier 1989; Woosley & Weaver 1995; Woosley et al. 2002; Elmhamdi et al. 2004; Maeda et al. 2007; Dessart & Hillier 2011, 2020; Jerkstrand et al. 2012, 2014, 2015; Fang & Maeda 2018; Fang et al. 2019). Also, since Hα and [N II] are dominantly emitted respectively from the H- and He-rich envelopes, (Hα, [N II])/[O I] can be used as a proxy for H/He-rich envelope stripping (Jerkstrand et al. 2015; Fang et al. 2019; Dessart & Hillier 2020).

However, there are a few caveats to note especially for stripped-envelope SNe (SESNe: IIb, Ib, and Ic in descending order of H/He-rich envelope mass). [N II]/[O I] could be affected by the progenitor He burning due to more He/N-layer burning in more massive stars (Jerkstrand et al. 2015; Fang et al. 2019). Also, [Ca II]/[O I] could be affected by the explosion energy due to more emission from the synthesized calcium than primordial calcium in the H-rich envelope (Li & McCray 1993; Maguire et al. 2012; Jerkstrand et al. 2015; Jerkstrand 2017). In principle, the progenitor convective mixing and SN explosive ^{56}Ni mixing could also alter these line ratios for CCSNe in general (Jerkstrand 2017; Dessart & Hillier 2020). Because of these possible systematic effects, the direct and quantitative comparison of the nature of the progenitors between different subclasses (e.g., SNe II vs. SESNe) will require detailed spectral modeling. Nevertheless, these line ratios should provide rough CCSN progenitor estimates.

In Fig. 3.12, we show the comparison of the nebular line ratios of SN 2016egz with a combined CCSN sample from Kuncarayakti et al. (2015), Fang et al. (2019), and
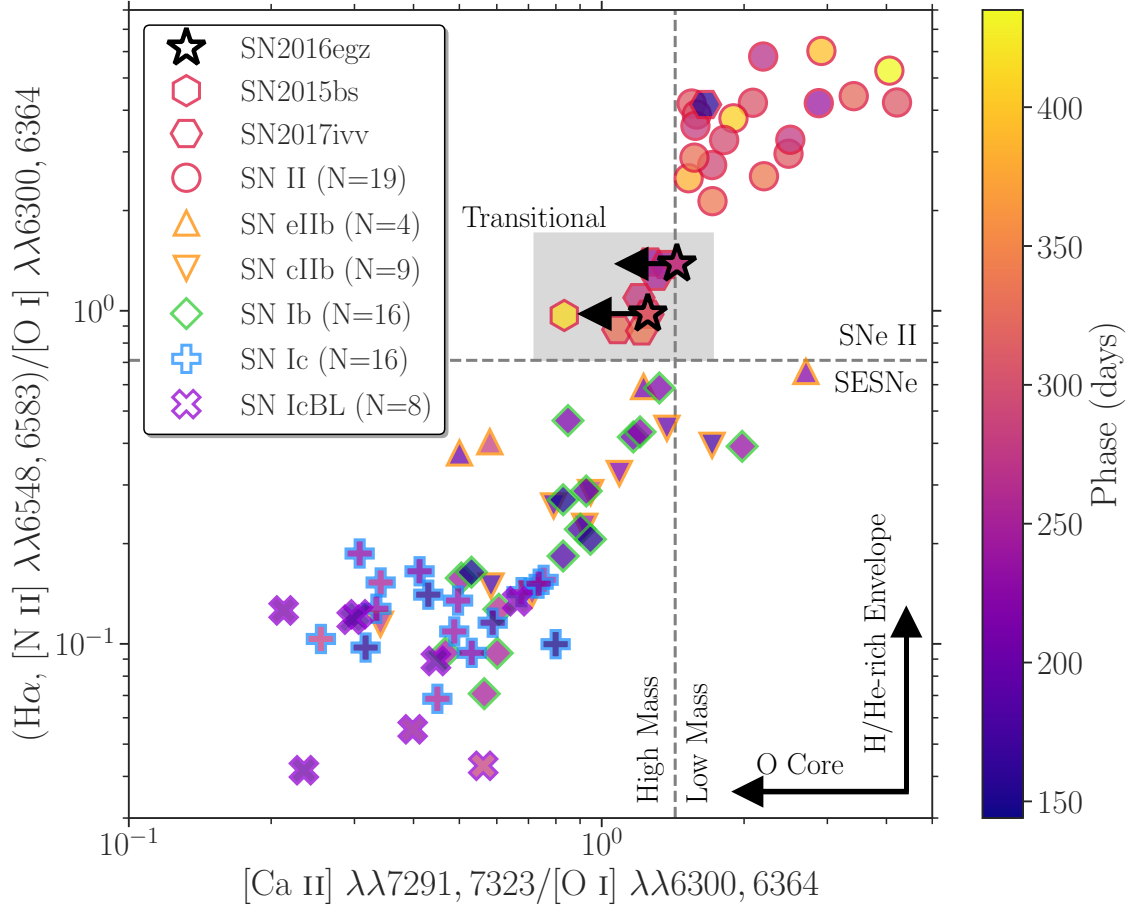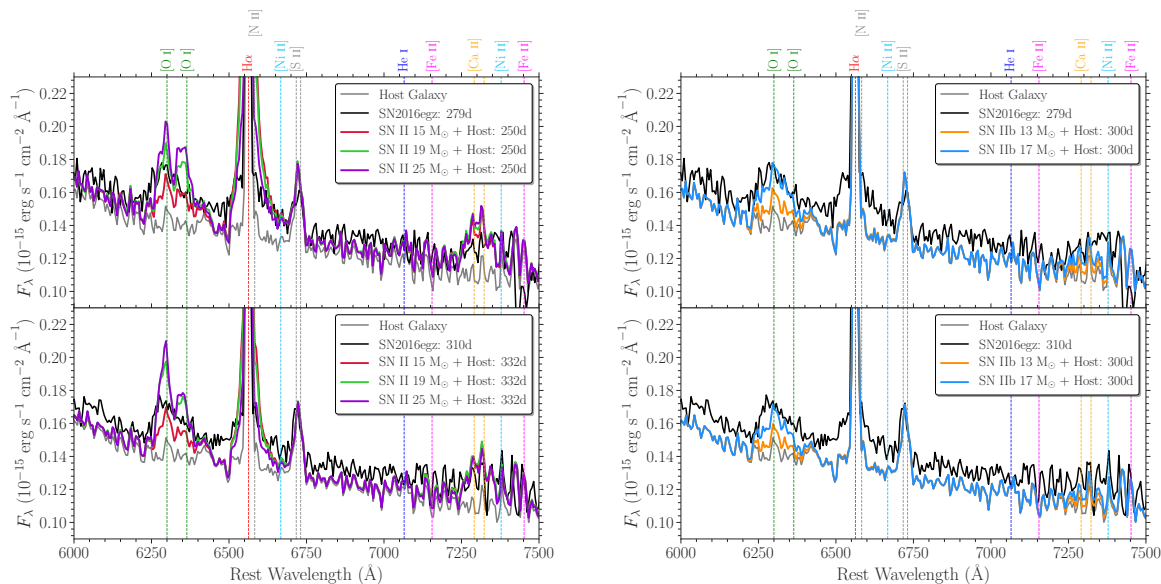
Figure 3.12: Comparison of the nebular line ratios of SN 2016egz with a CCSN sample, color coded by the phase. [Ca II]/[O I] and (Hα, [N II])/[O I] are proxies for progenitor O-core mass and H/He-rich envelope stripping, respectively. The vertical gray dashed line (= 1.43) is a rough division between SNe II and SESNe adopted in Gutiérrez et al. (2020), and the horizontal gray dashed line (= 0.71) is the highest value (+1σ error) in the SESN sample of Fang et al. (2019). Note the similar transitional nature of SN 2016egz to SNe II 2015bs and 2017ivv in between SNe II and SESNe (gray shaded region). Figure adapted from Kuncarayakti et al. (2015), Fang et al. (2019), and Gutiérrez et al. (2020), and expanded to include additional measurements from this work on the Kuncarayakti et al. (2015) SN II sample and SNe II 1990E, 1993K, 2012A (Silverman et al. 2017), 1990K (Cappellaro et al. 1995), 1994N (Pastorello et al. 2004), 2002hh (Faran et al. 2014), 2003B, 2008bk (Gutiérrez et al. 2017b), 2005cs (Pastorello et al. 2009), 2012aw (Jerkstrand et al. 2014), 2013ej (Silverman et al. 2012), 2015bs (Anderson et al. 2018), and 2016bkv (Hosseinzadeh et al. 2018), retrieved via the Open Supernova Catalog and WISeREP.

Gutiérrez et al. (2020) and additional SN II measurements from this work.[7] The general increasing and decreasing trends, respectively, in the progenitor O-core mass and H/He-rich envelope stripping can be seen in the sequence of SNe II–IIb–Ib–Ic–IcBL. For a given CCSN, [Ca II]/[O I] is relatively constant over $\sim$ 150–400 d after the explosion (Elmhamdi et al. 2004; Maguire et al. 2012; Kuncarayakti et al. 2015; Fang et al. 2019), while (Hα, [N II])/[O I] decreases with time (Maguire et al. 2012; Fang et al. 2019). Since the mean phases of the SN II and SESN samples are 330 days and 215 days, respectively, we expect to see more separation in the (Hα, [N II])/[O I] space if they had been all taken at the same epoch.

Fang et al. (2019) divide the SN IIb sample into extended (eIIb) and compact (cIIb) H-rich envelope classes based on their light-curve morphology. Chevalier & Soderberg 2010 suggest $M_{\mathrm{H_{env}}} \gtrsim 0.1\,M_\odot$ for SNe eIIb, and otherwise for SNe cIIb. Given the $M_{\mathrm{H_{env}}}$ range, SNe eIIb typically result in a double-peak light curve (Fig. 3.5(d)) where the first and second peaks are powered by shock-cooling envelope and radioactive decay, respectively. Compared to the other SESN types, Fang & Maeda (2018) and Fang et al. (2019) identify excess emission around [N II] for SNe eIIb and attribute it to Hα from the residual envelope.

We note that SN 2016egz as well as SNe 2015bs and 2017ivv lie in a somewhat transitional region between SNe II and eIIb–Ib (Fig. 3.12). For SN II 2015bs, Anderson et al. (2018) infer a high progenitor M_{ZAMS} of 17–25 $M_\odot$ based on the nebular line fluxes and velocities. Dessart & Hillier (2020) also suggest a high $M_{\mathrm{He_{core}}}$ and low $M_{\mathrm{H_{env}}}$ to better match the broad nebular line profiles ($v_{\mathrm{H\alpha,\,FWHM}} \simeq 4{,}200\,\mathrm{km\,s^{-1}}$; see also Dessart et al. 2010). For SN 2017ivv, Gutiérrez et al. (2020) estimate a M_{ZAMS} of 15–17 $M_\odot$ and note the transitional characteristics from SN II to IIb by analyzing the temporal evolution of

---

[7]By following the same procedure as the SN 2016egz measurements, except for [Ca II] where we fit a double-Gaussian profile with a single FWHM velocity.

(a) SN II models of Jerkstrand et al. (2014)   **(b)** SN IIb models of Jerkstrand et al. (2015)

Figure 3.13: Comparison of the nebular spectra of SN 2016egz with the SN II and IIb models from different progenitor M_{ZAMS}. The host spectrum is added to the model spectra that are scaled to match the distance, ^{56}Ni mass, and phase of the observed SN spectra. Due to the significant host contamination and low S/N, only broad [O I] and Hα features can be identified. Note the observed broad Hα and [O I] strengths in between those of SNe II–IIb and 17–25 $M_\odot$ models, respectively.

the nebular line ratios. Following this line of reasoning, the nebular line ratios (and upper limits) and velocities of SN 2016egz likely suggest a similar partially stripped massive progenitor. This agrees with the inferred parameters from the light-curve analysis.

In order to be more quantitative, we compare the nebular spectra of SN 2016egz with the SNe II and IIb models of Jerkstrand et al. (2014, 2015), respectively, in Fig. 3.13 where [O I] fluxes can be used to estimate the progenitor M_{ZAMS}. We scale the model spectra by the observed distance, ^{56}Ni mass, and phase of the SN 2016egz nebular spectra according to Equation (2) of Bostroem et al. (2019). Then, we add the observed host galaxy spectrum to the model spectra to account for the host contamination. The broad SN Hα (excluding the narrow host component) fluxes are in between those of the SNe II and IIb

models, indicating a small $M_{\mathrm{H_{env}}}$. The model [O I] lines start to saturate above $19\,M_\odot$ around 300 days (Jerkstrand et al. 2014), making the $19\,M_\odot$ and $25\,M_\odot$ models almost indistinguishable. Thus, we put a conservative M_{ZAMS} constraint of 17–$25\,M_\odot$ based on the observed [O I] fluxes. This is consistent with the expected $M_{\mathrm{ZAMS}} \gtrsim 17.5\,M_\odot$ from the light-curve analysis. One caveat to note is that there is no measurable [O I] $\lambda5577$ in the observed spectra due to the significant host contamination, preventing us from constraining the temperature and directly estimate the O-core mass (Jerkstrand et al. 2014, 2015; Jerkstrand 2017).

3.5 Discussion

3.5.1 Formation Channel

The short-plateau SNe 2006Y, 2006ai, and 2016egz most likely come from partially stripped massive progenitors,[8] but a remaining question is their exact formation channel. If it is single-star evolution as assumed in this work, the main theoretical uncertainties are RSG wind mass-loss rates and stellar rotation (e.g., Hirschi et al. 2004; Georgy 2012; Chieffi & Limongi 2013; Meynet et al. 2015; Renzo et al. 2017). We assume no rotation and tweak the wind efficiency by hand, but it is debatable whether such high mass-loss rates are physically plausible. Observationally, there is indeed a wide range of measured RSG wind mass-loss rates (e.g., de Jager et al. 1988; van Loon et al. 2005; Mauron & Josselin 2011; Goldman et al. 2017; Beasor et al. 2020). In addition, recent observational and theoretical studies on RSGs and SNe II indicate that RSG wind mass-loss rates may be independent from metallicity (Goldman et al. 2017; Chun et al. 2018; Gutiérrez et al. 2018). Thus, it could be possible that the short-plateau SNe 2006Y, 2006ai, and 2016egz

---

[8]The lack of nebular spectra for SNe 2006Y and 2006ai remains a caveat.

originate from single-star evolution. However, it is unlikely the case if RSG mass-loss rates are metallicity dependent (as in the main-sequence O/B stars; e.g., Vink et al. 2000, 2001; Mokiem et al. 2007), given the estimated subsolar host metallicities. In such a case, interacting binary evolution is more plausible, as Eldridge et al. (2017, 2018) indeed show some interacting binary products also result in short-plateau SNe. It is also important to note that any mass-loss models need to reproduce the observed populations of not only SNe II but also RSGs. For example, Neugent et al. (2020) recently show that the luminosity function of RSGs can be used to constrain their mass-loss rates. Future statistical studies with both RSG and SN II populations at various metallicities are required to distinguish the formation channels of short-plateau SNe.

Aside from the continuous mass loss, the origin of the confined dense CSM is not well understood. In the single-star scenario, a number of possible mechanisms have been proposed, including pulsation-driven superwinds (Heger et al. 1997; Yoon & Cantiello 2010), extended stellar envelopes (Dessart et al. 2017; Soker 2021), and internal gravity waves (Quataert & Shiode 2012; Shiode & Quataert 2014; Quataert et al. 2016; Fuller 2017; Leung & Fuller 2020; Morozova et al. 2020; Wu & Fuller 2021). Although the expected M_{ZAMS} range (19–25 $M_\odot$), where pulsation-driven superwinds could significantly alter mass loss, matches with our inferred M_{ZAMS} range for SNe 2006Y, 2006ai, and 2016egz, the expected maximum mass-loss rate of $\lesssim 10^{-3}\,M_\odot\,\mathrm{yr}^{-1}$ around 10^4–$10^6\,\mathrm{yr}$ before the core collapse may not result in confined CSM. Also, as the expected timescale of dominant CSM emission from an extended envelope (up to about 10–100 stellar radii) is only over a few days after explosion, whether it can reproduce the $\sim 10\,\mathrm{d}$ excess emission seen in SNe 2006Y, 2006ai, and 2016egz is questionable. In the binary scenario, the confined dense CSM may be expected from a wind collision interface formed between each binary component if the separation is wide enough (Kochanek 2019). With such a wide separation, however, short-plateau SNe do not result solely from binary interaction

(Eldridge et al. 2017, 2018). As such, the enhanced mass loss from internal gravity waves remains more probable, although the light-curve model predictions can be quite flexible by varying the amount and time of nuclear energy injection (Morozova et al. 2020).

3.5.2 Implications for the RSG Problem

Regardless of the exact progenitor formation scenario, our conclusion based on the SN photometric and spectroscopic analyses should still hold, and it is worth discussing the implications of the short-plateau SNe for the RSG problem. Some proposed solutions even point toward the nonexistence of the RSG problem, as the high-mass progenitors ($\gtrsim 20\,M_\odot$) may not end their lives as RSGs, but as yellow supergiants (or even blue supergiants or Wolf–Rayet stars) resulting in SNe IIb/Ib (or Ib/c) due to binary interaction (Eldridge et al. 2008, 2013, 2017, 2018), stellar rotation (Hirschi et al. 2004; Chieffi & Limongi 2013), and/or wind mass loss (Georgy 2012; Meynet et al. 2015; Renzo et al. 2017). Others propose the high-mass RSGs do explode as SNe II, but the mistreatment of dust extinction (Walmswell & Eldridge 2012; Beasor & Davies 2016) and/or bolometric correction (Davies & Beasor 2018) in the direct progenitor identifications systematically underestimates the progenitor masses. In addition, the statistical significance of the RSG problem has been questioned (see Davies & Beasor 2020; Kochanek 2020 for recent discussions). If the RSG problem is indeed real, then the direct collapse of high-mass RSGs to black holes (i.e., failed explosion) is a plausible solution (O'Connor & Ott 2011; Ugliano et al. 2012; Kochanek 2014; Gerke et al. 2015; Pejcha & Thompson 2015; Sukhbold et al. 2016; Adams et al. 2017; Basinger et al. 2020; Pejcha 2020; Kresse et al. 2021). In this context, the transitional nature of SNe 2006Y, 2006ai, and 2016egz is important, highlighting the possibility that these partially stripped massive progenitors die as RSGs and explode as short-plateau SNe II, rather than becoming SESNe or directly collapsing to
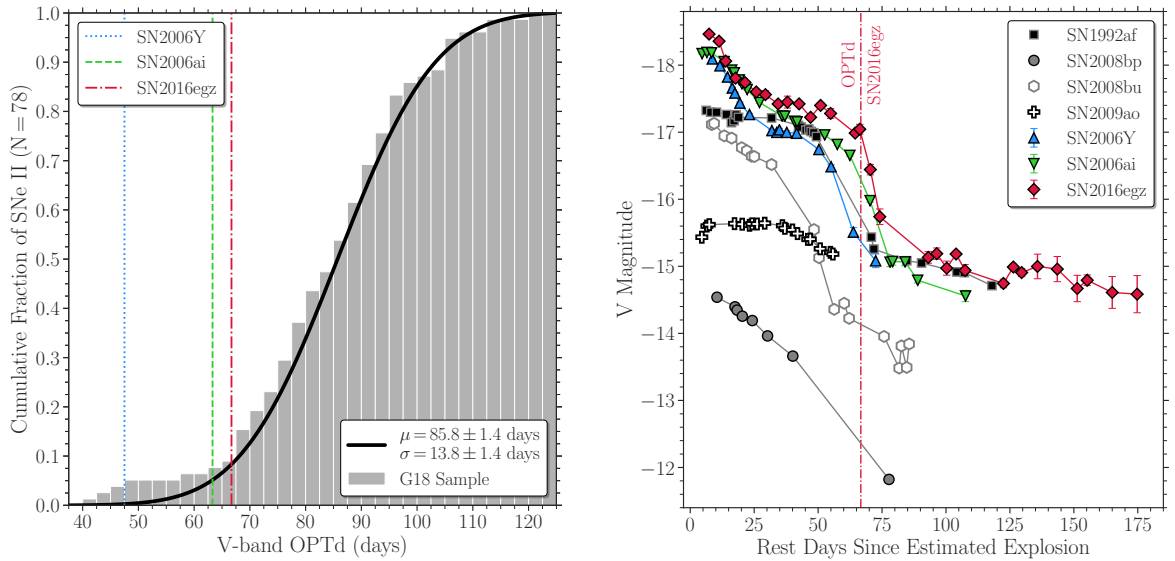
(a) Cumulative distribution of *V*-band optically-thick phase duration (OPTd) of the Gutiérrez et al. (2018 G18) sample

(b) SN II *V*-band light curves with shorter OPTd than SN 2016egz, as in (a), from Anderson et al. (2014)

Figure 3.14: Distribution of the SN II OPTd with a mean $\mu \simeq 86\,\text{days}$ and standard deviation $\sigma \simeq 14\,\text{days}$. SNe 2006Y, 2006ai, and 2016egz show similar luminous short-plateau light curves, while SNe 2008bp and 2008bu show IIL-like light curves (the extinction and explosion epoch of SN 1992af are not well constrained, and the fall from the plateau of SN 2009ao is not well sampled). Note the small fraction of short-plateau SNe ($3/78 \simeq 4\%$).

black holes.

As a first-order rate estimate for short-plateau SNe, we use the optically thick phase duration (OPTd; the time between the explosion and the plateau drop) distribution of SNe II (including SNe 2006Y, 2006ai, and 2016egz) from Gutiérrez et al. (2018) in Fig. 3.14. The lack of SNe II with OPTd $\lesssim 40\,\text{days}$ indicates that there exists an H-rich envelope boundary between SNe II and IIb, as also seen in the light-curve model grid (Fig. 3.5). On the tail of the smooth Gaussian-like OPTd distribution, there is a small population with shorter OPTd than SN 2016egz (Fig. 3.14).

SNe 2008bp[9] and 2008bu show IIL-like light curves with fainter ^{56}Co decay tails than those of SNe 2006Y, 2006ai, and 2016egz. Their light curves might be reproduced with the high-mass ($\geq 17.5\,M_\odot$) progenitor models within the short-plateau $M_{\mathrm{H_{env}}}$ range with a lower M_{Ni} and varying E_{exp} (Figs. 3.5(c) & 3.6(c)). We do not consider the other SNe as probable short-plateau candidates here because of the uncertainties in extinction and explosion epoch for SN 1992af (Anderson et al. 2014; Galbany et al. 2016b; Gutiérrez et al. 2017b) and the poor light-curve sampling at the plateau fall for SN 2009ao. If we take the short-plateau SN fraction of 3/78 (or 5/78 if we naively include SNe 2008bp and 2008bu) at face value, a short-plateau SN rate of $\sim 4\%$ (or $\sim 6\%$) of all SNe II can be inferred. This is roughly consistent with the rate estimate from Eldridge et al. (2018) ($\sim 4.7\%$; see §3.4.3). Recently, Gofman et al. (2020) apply enhanced mass-loss rates to RSGs and found that massive RSGs ($M_{\mathrm{ZAMS}} \simeq 20\text{–}21\,M_\odot$) with a similar $M_{\mathrm{H_{env}}}$ range ($\sim 0.8\text{–}1.8\,M_\odot$) to that of our short-plateau SN models end up as dust-unobscured SNe II. They roughly estimate a rate of this class to be 2–4% of all SNe II, which is similar to our estimate of short-plateau SNe.

Assuming the Salpeter IMF with lower and upper RSG mass limits of 8 and $25\,M_\odot$, respectively, the inferred ZAMS mass range of the short-plateau SNe 2006Y, 2006ai, and 2016egz (18–22 $M_\odot$) corresponds to 10% of all SNe II. It may be possible that the missing fraction ($10\% - 4\% = 6\%$) does not end up as RSGs, but there also seems to be an absence of promising high-mass SESN candidates (Lyman et al. 2016; Taddia et al. 2018; Barbarino et al. 2020). Thus, together with SN 2015bs (Anderson et al. 2018) and the possible failed explosion of a $\sim 25\,M_\odot$ RSG (Gerke et al. 2015; Adams et al. 2017; Basinger et al. 2020), this apparent rate mismatch may support the proposed *islands of explodability in a sea of black hole formation* (Sukhbold et al. 2016) where there is no

---

[9]The extinction estimate for SN 2008bp may be significantly underestimated (Anderson et al. 2014), and so the luminosity could be much higher.

single mass cut between SN II explosions and black hole formations (see also O'Connor & Ott 2011; Ugliano et al. 2012; Pejcha & Thompson 2015; Patton & Sukhbold 2020; Pejcha 2020; Sukhbold & Adams 2020; Kresse et al. 2021).

In order to further test the hypothesis, more detailed progenitor mass and rate calculations of short-plateau SNe are necessary. The bare photospheres of the short-plateau SN progenitor models in this work lie in the effective temperature and photospheric luminosity ranges of $3.65 < \log_{10}(T_{\mathrm{eff}}/\mathrm{K}) < 3.72$ and $5.23 < \log_{10}(L_{\mathrm{ph}}/L_\odot) < 5.53$, respectively, which are within those observed for luminous RSGs (e.g., Levesque et al. 2005, 2006; Massey et al. 2009; Drout et al. 2012; Gordon et al. 2016). Given the high constant mass loss as well as the enhanced mass loss in the last few decades before the explosion, however, significant dust extinction is likely expected for the short-plateau SN progenitors (e.g., Nozawa & Fukugita 2013; Nozawa et al. 2014), making their direct progenitor identifications unlikely (if they all come from the single-star channel; see Eldridge et al. 2017, 2018 for the interacting binary channel). The circumstellar dust is likely destroyed as the SN shock progresses through. Therefore, SN photometric and spectroscopic analyses of large samples will be required to better determine their progenitor mass and rate distributions.

3.6   Conclusions

We have presented the optical/NIR photometric and spectroscopic observations of luminous Type II short-plateau SNe 2006Y, 2006ai, and 2016egz. Based on the V-band and pseudobolometric light-curve sample comparisons, the peculiar light curves with the short plateaus and luminous peaks suggest partially stripped H-rich envelopes and CSM interaction at early time. We have constructed a large MESA+STELLA single-star progenitor and light-curve model grid (with and without CSM interaction) that shows

a continuous population of SNe IIP–IIL–IIb-like light-curve morphology in descending order of H-rich envelope mass, with short-plateau SNe lying in a confined parameter space between SNe IIL and IIb with large ^{56}Ni masses ($\gtrsim 0.05\,M_\odot$). For SNe 2006Y, 2006ai, and 2016egz, our model grid suggests high-mass RSG progenitors ($M_{\rm ZAMS} \simeq 18$–$22\,M_\odot$) with small H-rich envelope masses ($M_{\rm H_{env}} \simeq 1.7\,M_\odot$) to reproduce the short-plateau light curves, and enhanced mass loss ($\dot{M} \simeq 10^{-2}\,M_\odot\,{\rm yr}^{-1}$) for the last few decades before the explosion to capture the early luminous peaks. In addition, the P Cygni profiles and photospheric velocities likely point toward low H-rich envelope masses, and the nebular line ratios and spectral model comparisons prefer high-mass ($M_{\rm ZAMS} \simeq 17$–$25\,M_\odot$) progenitors.

Although the exact progenitor formation channel remains an open question, the transitional nature of SNe 2006Y, 2006ai, and 2016egz has important implications for the RSG problem, in that these partially stripped massive progenitors end their lives as RSGs and explode as short-plateau SNe. We roughly estimate a short-plateau SN rate of $\sim 4\%$ of all SNe II, which is smaller than the IMF expectation of $\sim 10\%$. This rate mismatch may support the proposed *islands of explodability* scenario. Further verification of this scenario requires the determination of the short-plateau SN progenitor mass and rate distributions through large SN photometric and spectroscopic sample analyses (as done in this work for three objects), as their direct progenitor identifications are expected to be quite challenging. Current and future large transient surveys are promising to provide the necessary SN samples.

3.6.1   Appendix: Extra `MESA`+`STELLA` Description and Models

We start with `MESA` 10398 test suites, `example_make_pre_ccsn` and `example_ccsn_IIp`, respectively, for progenitor evolution from the pre-main sequence to Fe-core infall and

SN explosions from the core collapse to near shock breakout (by excising the core and injecting a thermal bomb). Then we use STELLA for SN light-curve and expansion-velocity calculations from the shock breakout to radioactive decay tail. The reader is referred to Paxton et al. (2018) for more details on the workflow and relevant physical parameters.

For the MESA progenitor model grid, we vary ZAMS masses ($M_{\mathrm{ZAMS}} = 10.0$–$25.0\,M_\odot$ with $2.5\,M_\odot$ increments) and wind scaling factors ($\eta_{\mathrm{wind}} = 0.0$–$3.0$ with 0.1 increments), while fixing subsolar ZAMS metallicity ($Z = 0.3\,Z_\odot$), no rotation ($\nu/\nu_{\mathrm{crit}} = 0$), mixing length in the H-rich envelope ($\alpha_{\mathrm{env}} = 3.0$), and convective overshooting parameters ($f_{\mathrm{ov}} = 0.02$ and 0.01 for $10.0\,M_\odot$ and the other ZAMS masses, respectively). As the main objective of this work is to observe how SN II light curves are affected by H-rich envelope stripping, we control the progenitor mass loss by using the *Dutch* prescription (Glebbeek et al. 2009, and references therein) and arbitrarily varying η_{wind} in single-star evolution (see, e.g., Mauron & Josselin 2011; Goldman et al. 2017; Beasor et al. 2020 for a wide range of observed RSG mass-loss rates), rather than exploring the details of mass-loss mechanisms (e.g., interacting binary evolution; see Eldridge 2017 for a review). With our parameter setup, $\sim 20\%$ of the MESA progenitor models do not advance to Fe-core formation, mostly due to some low-mass ($\leq 12.5\,M_\odot$) models developing highly degenerate cores and fail during off-center burning stages such as neon ignition.

For the MESA explosion model grid, we vary explosion energies ($E_{\mathrm{exp}} = 0.4$–$2.0 \times 10^{51}\,$erg with $0.2 \times 10^{51}\,$erg increments) for each progenitor model. The SN shock propagation is modeled with the Duffell (2016) Rayleigh-Taylor instability mixing prescription until near shock breakout, and the resultant ^{56}Ni distribution is scaled to match a fixed ^{56}Ni mass ($M_{\mathrm{Ni}} = 0.04$, 0.07, and $0.1\,M_\odot$). Then, we hand off these explosion models to STELLA to produce synthetic light curves and expansion velocities using 400 spatial zones and 40 frequency bins. Any fallback material is frozen onto the central remnant and excised via a $500\,\mathrm{km\,s^{-1}}$ velocity cut at the inner boundary at the handoff between MESA

and STELLA (i.e., the extra heating from fallback accretion onto the central remnant is not taken into account, but can be relevant for high-mass progenitors with low E_{exp}; e.g., Lisakov et al. 2018; Chan et al. 2018; Moriya et al. 2019). With our parameter setup, $\sim 5\%$ each of the MESA explosion models and STELLA light-curve models do not converge numerically, mostly with high-mass ($\geq 22.5\,M_{\odot}$) progenitors. We simply discard the failed models (in Fe-core formation or explosion) and focus on the bulk properties of the model grid in this work.

As for the model grids with $M_{\mathrm{Ni}} = 0.04$ and $0.1\,M_{\odot}$, the light-curve models are shown in Figs. 3.15 & 3.16, and the short-plateau SN velocity models are shown in Fig. 3.17.

(a) IIP ($4.5\,M_\odot \leq M_{\mathrm{H_{env}}} \leq 15.8\,M_\odot$)

(b) IIL ($2.12\,M_\odot \leq M_{\mathrm{H_{env}}} \leq 4.5\,M_\odot$)

(c) Short-Plateau ($0.91\,M_\odot \leq M_{\mathrm{H_{env}}} \leq 2.12\,M_\odot$)

(d) IIb ($0.39\,M_\odot \leq M_{\mathrm{H_{env}}} \leq 0.91\,M_\odot$)
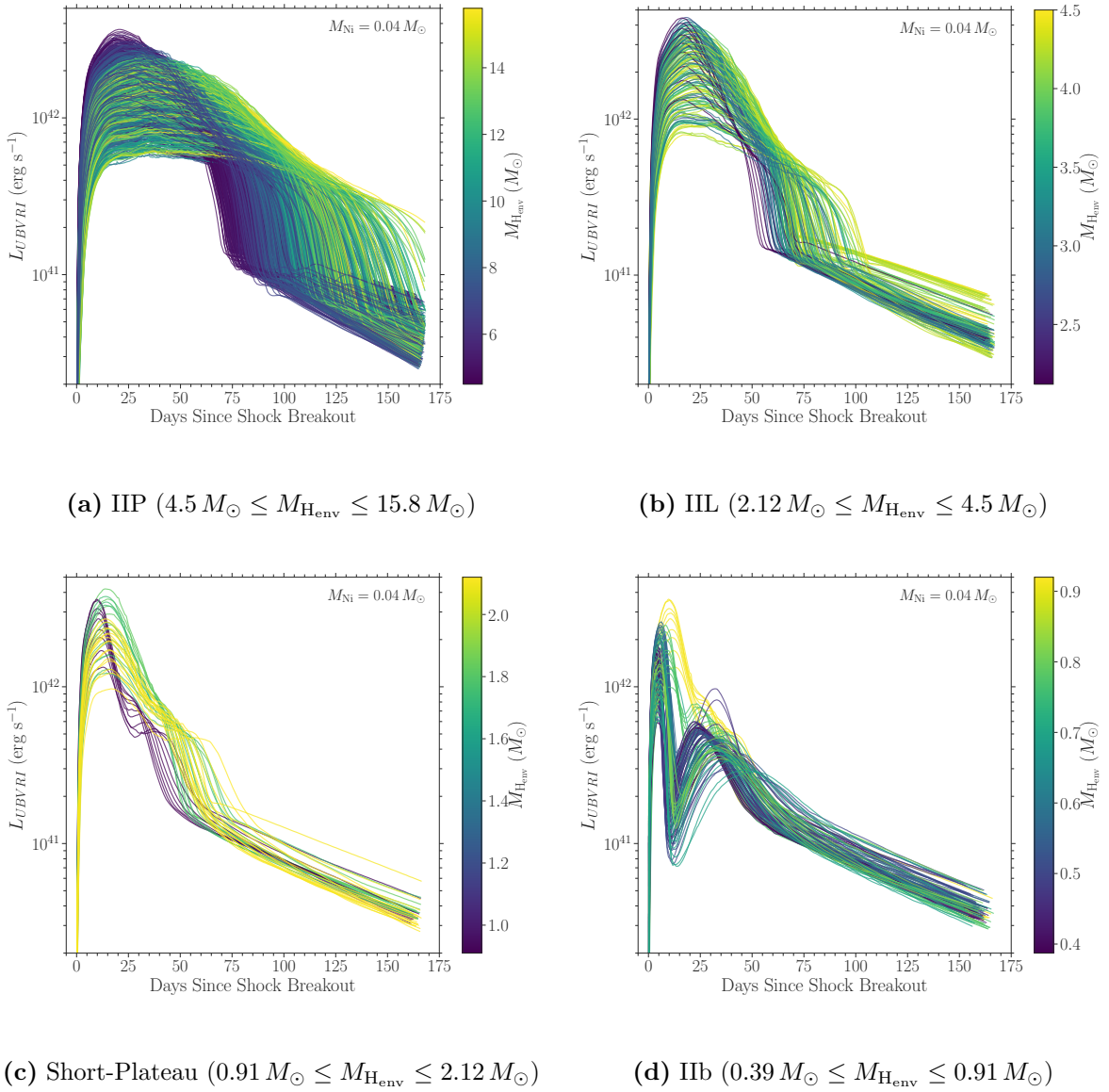
Figure 3.15: Same as Fig. 3.5, but with $M_{\mathrm{Ni}} = 0.04\,M_\odot$.

(a) IIP $(4.5\,M_\odot \leq M_{\mathrm{H_{env}}} \leq 15.8\,M_\odot)$

(b) IIL $(2.12\,M_\odot \leq M_{\mathrm{H_{env}}} \leq 4.5\,M_\odot)$

(c) Short-Plateau $(0.91\,M_\odot \leq M_{\mathrm{H_{env}}} \leq 2.12\,M_\odot)$

(d) IIb $(0.39\,M_\odot \leq M_{\mathrm{H_{env}}} \leq 0.91\,M_\odot)$
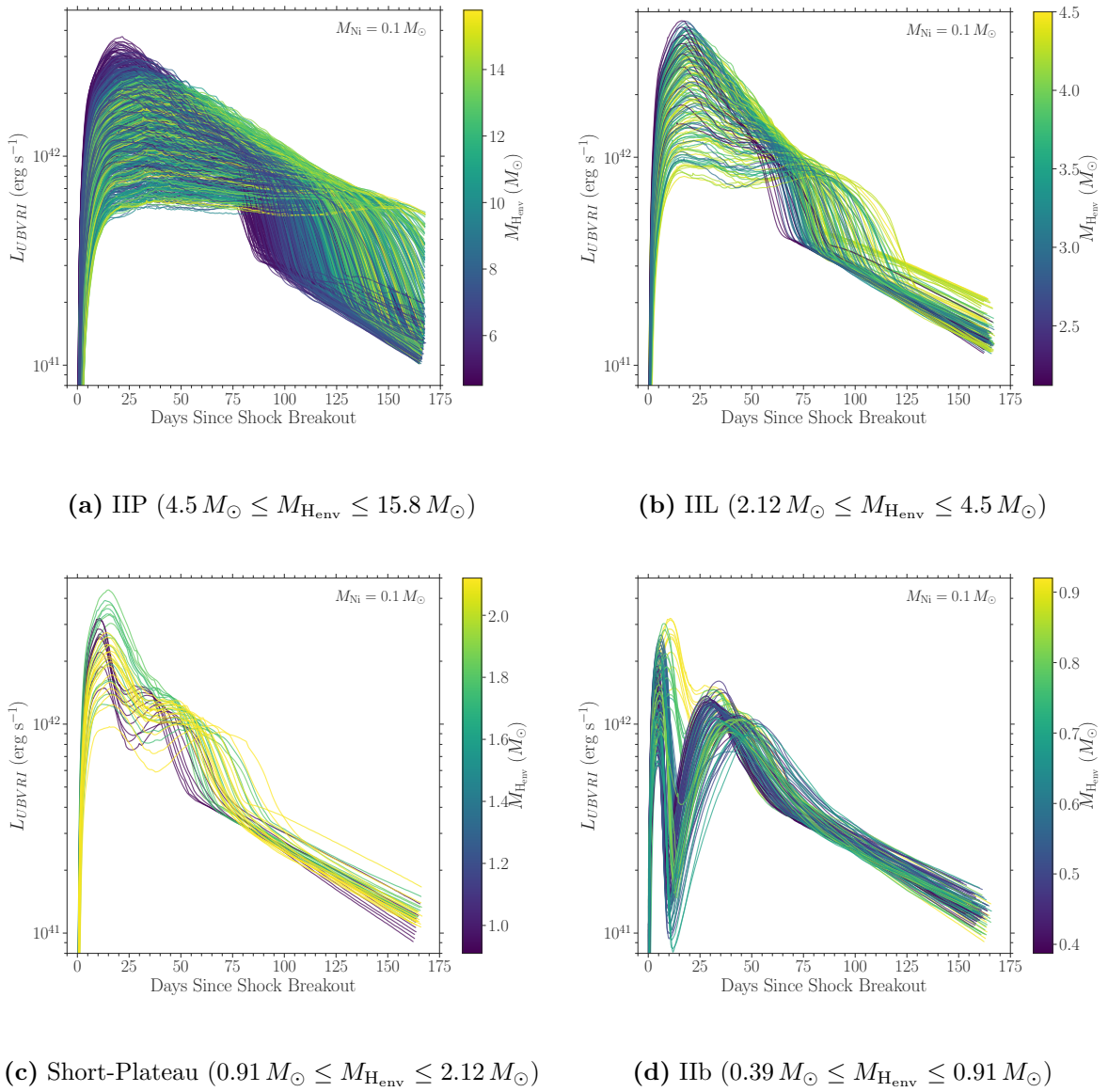
Figure 3.16: Same as Fig. 3.5, but with $M_{\mathrm{Ni}} = 0.1\,M_\odot$.

(b) $M_{\mathrm{Ni}} = 0.04\,M_{\odot}$ **(a)** $M_{\mathrm{Ni}} = 0.1\,M_{\odot}$
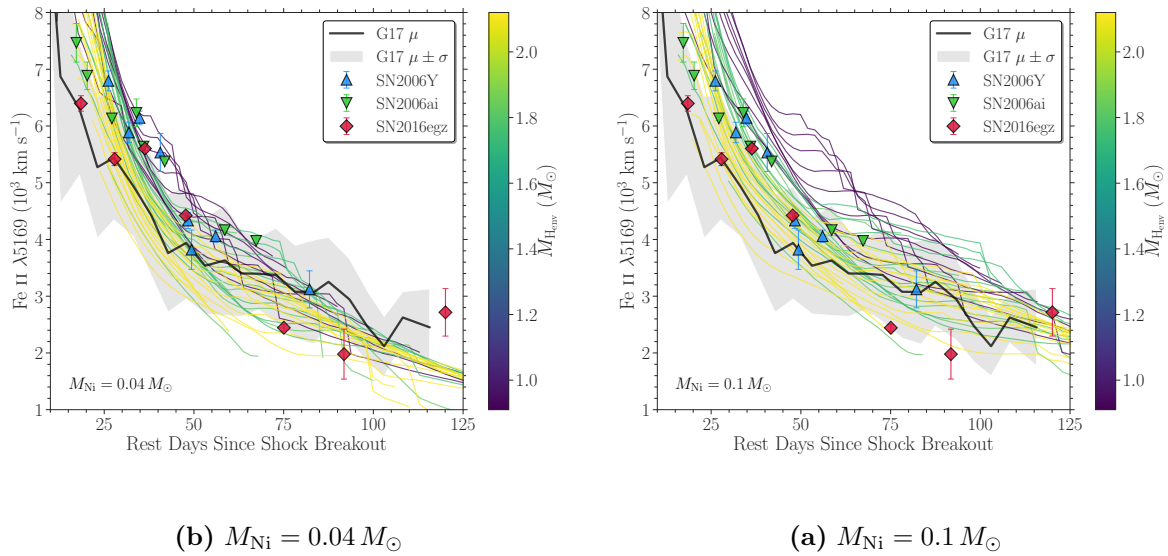
Figure 3.17: Same as Fig. 3.11, but with $M_{\mathrm{Ni}} = 0.04$ and $0.1\,M_{\odot}$.

Chapter 4

Superlinear Type II Superluminous Supernovae

This chapter is reproduced from Hiramatsu et al. (in prep.). I would like to thank my coauthors, without whom this work would not have been possible: Takashi J. Moriya, D. Andrew Howell, Iair Arcavi, Jamison Burke, Griffin Hosseinzadeh, Curtis McCully, Stefano Valenti, Maria R. Drout, Saurabh W. Jha, Youssef Eweis, and Sergei I. Blinnikov.

4.1 Introduction

SLSNe are characterized by their bright light curves ($\lesssim -21$ mag) that require mysterious power sources beyond those of traditional SNe (e.g., radio active decay or shock-deposited energy; see Gal-Yam et al. 2014; Howell 2017; Moriya et al. 2018b for reviews). CSM interaction is thought to be a main power source for SNe with narrow Balmer-series emission lines in spectra (SNe IIn), some of which become bright enough to reach into the SLSN regime (SLSNe-II). Due to CSM contamination, however, the nature of underlying SNe and their progenitor systems remain elusive.

SNe Ia are the thermonuclear explosions of CO WDs (see Howell 2011; Maoz et al. 2014; Maguire 2016 for reviews). Despite their cosmological uses discovering the accelerating expansion of the Universe and revealing its energy contents (Riess et al. 1998;

Perlmutter et al. 1999), open questions still remain on their progenitor systems and explosion mechanisms. The two leading theories are the single-degenerate (SD) scenario in which a CO WD accrete material from a nondegerate companion, and the double-degenerate (DD) scenario in which a CO WD merge with another WD.

SNe Ia-CSM are an intriguing intersection between SNe IIn and SNe Ia in that they show Balmer-series emission lines on top of a diluted SN Ia-like continuum (e.g., Silverman et al. 2013b). A few SNe Ia-CSM show clear SN Ia-dominated spectra at early phase (e.g., SN 2002ic; Hamuy et al. 2003; Deng et al. 2004; Wood-Vasey et al. 2004 and PTF11kx; Dilday et al. 2012; Silverman et al. 2013a), confirming their SN Ia origin. On the other hand, most of them are dominated by CSM interaction without clean SN Ia signatures (e.g., Leloudas et al. 2015), making the hydrogen/helium-poor core-collapse SN (SN Ic) origin also compatible (e.g., see Fox et al. 2015; Inserra et al. 2016 for the discussions on SN 2012ca). If SNe Ia-CSM indeed come from SNe Ia, then these are the best candidates for the SD scenario (e.g., Terman et al. 1994; Taam & Sandquist 2000; Sabach & Soker 2014; Soker 2019; Ablimit 2021).

SLSN-II 2006gy is another possible intriguing case that may bridge SLSNe-II and SNe Ia. It was originally suggested to originate from a very massive star (even as high as $\sim 100\,M_\odot$; Ofek et al. 2007; Smith et al. 2007, 2010). However, Jerkstrand et al. (2020) recently reanalyze a nebular spectrum of SLSN-II 2006gy (Kawabata et al. 2009), identifying strong iron lines that require comparable iron yields to SNe Ia which are higher than CCSNe. They also show their updated light curve is compatible to SNe Ia interacting with massive CSM of $\sim 13\,M_\odot$. In this context, observations of SN IIn/SLSNe-II and modeling of SNe Ia-CSM are of great importance in revealing their true nature.

Here, we report optical photometry and spectroscopy of SLSNe-II 2017fck and 2019cmv with post-maximum "superlinear" light curves, along with a numerical light-curve model grid of SNe Ia-CSM. We summarize their discoveries, follow-up observations, and data

reduction in § 4.2 & 4.3. In § 4.4, we analyze their host galaxies, spectra, and light curves, identifying some similarities to SNe Ia-CSM, especially the linearly declining luminous light curves. Then in § 4.5, we perform numerical light-curve modeling of SNe Ia-CSM, reproducing the diversity in SNe Ia-CSM by various CSM density distributions. Finally, we discuss possible progenitors systems and summarize our findings in § 4.6.

4.2   Discoveries

The *Gaia* Science Alerts (Hodgkin et al. 2021) discovered SN 2017fck (Gaia17bro) on 2017 July 2.54 (UT dates are used throughout) at 16.48 mag in G band at R.A. = $05^h19^m54^s.370$ and Dec. = $-56°11'08".48$ with a last non-detection limit on 2017 June 7.80 at 21.5 mag in G band, using the *Gaia* Spacecraft (Delgado et al. 2017). Strader (2017) obtained an optical spectrum of SN 2017fck on 2017 August 1.38 with the Goodman Spectrograph on the Southern Astrophysical Research Telescope (SOAR), classifying it as an SN IIn at a redshift $z = 0.09442$ from the narrow host galaxy lines (see also Strader et al. 2017 noting a possible Ia/Ic-CSM classification).

The Zwicky Transient Facility (ZTF; Bellm et al. 2019; Graham et al. 2019) discovered SN 2019cmv (ZTF19aalbrgu) on 2019 March 25.51 at 17.92 mag in g band at R.A. = $18^h57^m52^s.996$ and Dec. = $+45°35'24".00$, using the ZTF camera on the Samuel Oschin 48-inch Schmidt Telescope at the Palomar Observatory (Nordin et al. 2019). Upon the ZTF discovery, the *Gaia* Science Alerts reported a prediscovery G-band detection on 2019 February 24.92 at 19.51 mag at R.A. = $18^h57^m52^s.990$ and Dec. = $+45°35'24".00$ to TNS. The associated last G-band non-detection limit on 2019 February 24.85 (< 2 hours of discovery) at 21.5 mag was retrieved via the *Gaia* Photometric Science Alerts (Hodgkin et al. 2021). Thus, the tighter *Gaia* discovery and last non-detection are adopted in this work. Fremling et al. (2019) obtained an optical spectrum of SN 2019cmv on 2019 April

17.92 with the SPectrograph for the Rapid Acquisition of Transients (SPRAT) on the Liverpool Telescope (LT), classifying it as an SLSN-II at a redshift $z = 0.097$ from the narrow Balmer-series emission lines.

Given the reasonable last non-detection limits, we estimate an explosion epoch of each SN by simply taking the midpoint of the last non-detection and the first detection with the error being the estimated explosion epoch minus the last non-detection. This yields $\mathrm{MJD}_0 = 57924 \pm 11$ and 58538.89 ± 0.03 respectively for SNe 2017fck and 2019cmv, which is used as a reference epoch for all phases unless otherwise specified.

We obtained a host galaxy spectrum of each SN after the SN had faded (§ 4.3) and determined an SN-independent redshift: $z = 0.09456 \pm 0.00004$ and 0.0974 ± 0.0004 respectively for SNe 2017fck and 2019cmv (§ 4.4.1), which we adopt in this work. Then we assume a standard Lambda cold dark matter cosmology with $H_0 = 71.0 \ \mathrm{km\,s^{-1}\,Mpc^{-1}}$, $\Omega_\Lambda = 0.7$, and $\Omega_m = 0.3$, and convert the redshift to a luminosity distance: $d_L = 427.6$ Mpc ($\mu = 38.16$ mag) and 441.3 Mpc (38.22 mag) for SNe 2017fck and 2019cmv, respectively.

4.3   Observations and Data Reduction

LCO *UBgVri*-band data for SNe 2017fck and 2019cmv were obtained with the Sinistro cameras on the network of 1-m telescopes at the Cerro Tololo Inter-American Observatory (District IV, Chile), Siding Spring Observatory (New South Wales, Australia), South African Astronomical Observatory (Sutherland, South Africa), and McDonald Observatory (Texas, USA), through GSP. Using `lcogtsnpipe`, PSF fitting was performed. Reference images were obtained with a Sinistro camera after the SN had faded, and image subtraction was performed using `PyZOGY`. *UBV*- and *gri*-band data were calibrated to Vega (Stetson 2000) and AB (Albareti et al. 2017) magnitudes, respectively, using

standard fields observed on the same night by the same telescope as the SN. In addition, public *Gaia G*-band light curve for SNe 2017fck and 2019cmv and ZTF *gr*-band light curves for SN 2019cmv were retrieved via the *Gaia* Photometric Science Alerts and the ALeRCE ZTF Explorer (Förster et al. 2021), respectively, and used in the following analysis.

LCO optical spectra for SNe 2017fck and 2019cmv were taken with the FLOYDS spectrographs mounted on the 2m FTN and FTS at Haleakala (USA) and Siding Spring (Australia), respectively, through the Supernova Key Project and GSP. A 2″0 slit was placed on the target along the parallactic angle. One-dimensional spectra were extracted, reduced, and calibrated following standard procedures using `floyds_pipeline`. A late-time optical spectrum of SN 2017fck was obtained with the Low Dispersion Survey Spectrograph 3 (LDSS-3) mounted on the 6.5 m Magellan Clay telescope on 2018 March 15.0. The VHP-All grism coupled with a 1″0 slit for dispersion was used to obtained a single 1,200 s exposure. The data were reduced in a standard manner using PyRAF. In addition, the classification spectra of SNe 2017fck (Strader 2017) and 2019cmv (Fremling et al. 2019) were retrieved via TNS and used in the following analysis.

The host galaxy spectrum of SN 2017fck was observed with the Robert Stobie Spectrograph (RSS; Smith et al. 2006) mounted on the Southern African Large Telescope (SALT) at Sutherland (South Africa) on 2018 October 6.0 (through Rutgers University program 2018-1-MLT-006; PI: S. W. Jha). A 1″5 wide longslit and the PG0900 grating in two tilt angles were used to cover the wavelength range from 470–840 nm. The data were reduced using a custom pipeline based on standard PyRAF spectral reduction routines and the `PySALT` package (Crawford et al. 2010). The host galaxy spectrum of SN 2019cmv was observed with FTN/FLOYDS and reduced in the same way as described above (see § 4.4.1 for the host galaxy association).

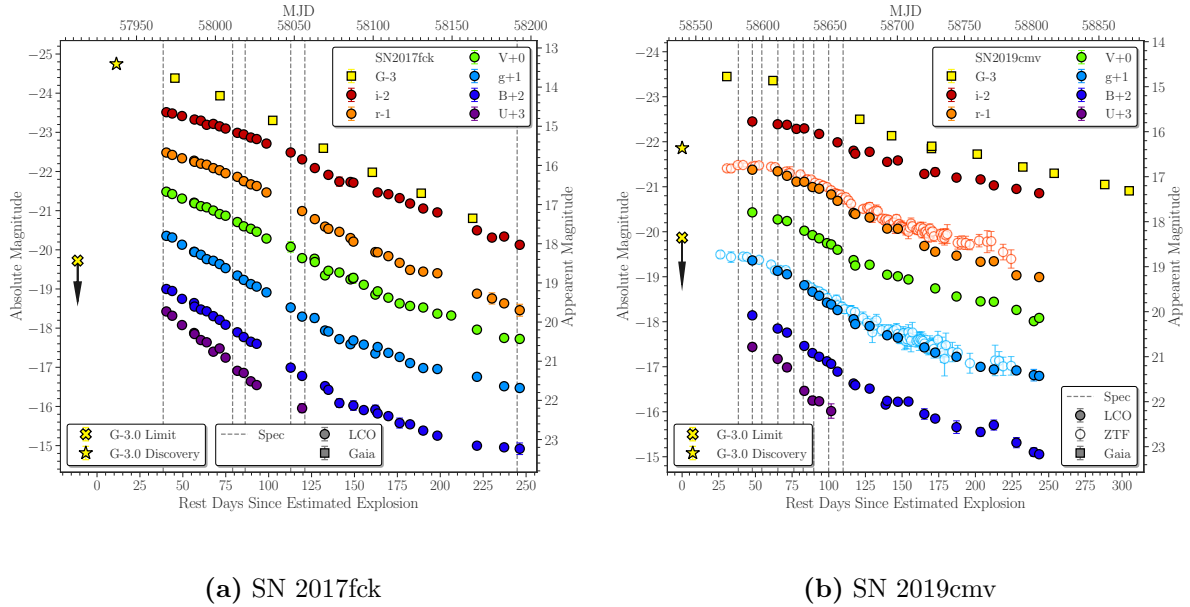All photometry and spectroscopy of SNe 2017fck and 2019cmv are presented in

(a) SN 2017fck   **(b)** SN 2019cmv

Figure 4.1: Extinction-corrected light curves of SNe 2017fck and 2019cmv. Error bars denote 1σ uncertainties and are sometimes smaller than the marker size. The gray vertical dashed lines show the spectral epochs (Fig. 4.2). The explosion epoch of SN 2017fck is not well constrained (±11 d), while that of SN 2019cmv is extremely well constrained (±0.03 d; showing the rapid rise of at least ~ 2.0 mag within the first epoch). ZTF r-band light curve is systematically brighter than that of LCO since ZTF bandpass is slightly redder, including the strong Hα contribution at the SN redshift. Note the similar superluminous G-band peaks ($-21.8 \leq M_G \leq -20.4$) and long G-band superlinear decline (~ 0.01–0.02 mag day^{-1} for $\gtrsim 200$ days).

Figs. 4.1 & 4.2, respectively, and will be available for download via the Open Supernova Catalog and WISeREP. For SNe 2017fck and 2019cmv, no Na I D absorption is seen at the host redshift (Fig. 4.2), indicating low host extinction at the SN position. Thus, we correct all photometry and spectroscopy only for the MW extinction (Schlafly & Finkbeiner 2011, via IRSA) of $A_V = 0.075$ and 0.156 for SNe 2017fck and 2019cmv, respectively, assuming the Fitzpatrick (1999) reddening law with $R_V = 3.1$.

(a) SN 2017fck   **(b)** SN 2019cmv
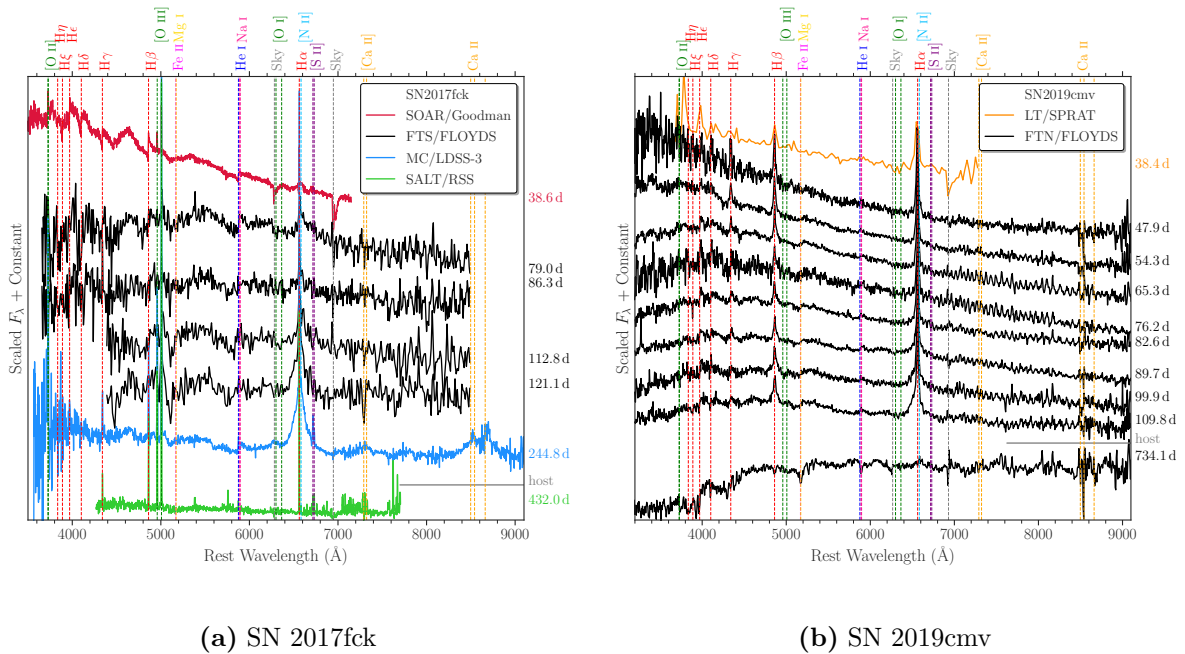
Figure 4.2: Extinction-corrected spectral time series of SNe 2017fck and 2019cmv. The phase of each spectrum is given on the right. The first spectrum of each SN is the classification spectrum on TNS. The last spectra show a star-forming and elliptical host galaxies for SNe 2017fck and 2019cmv, respectively. Note the Balmer-series line evolution from the narrow symmetric profiles to broad asymmetric profiles and the increasing $H\alpha/H\beta$ flux ratios.

4.4   Analysis

4.4.1   Host Galaxies

We use the archival images and catalogs from the Dark Energy Survey Data Release 2 (DES DR2; DES Collaboration et al. 2021) and the Pan-STARRS1 Data Release 2 (PS1 DR2; Flewelling et al. 2020), respectively, to identify the host galaxies of SNe 2017fck and 2019cmv. We obtain the Kron radii (in which $\sim 90\%$ of the total luminosity should be contained; Kron 1980) of nearby galaxy-like objects within 0.′5 of the SN location from the DES and PS1 catalogs, and associate the one with the smallest offset from the SN location in terms of Kron radius as a potential host galaxy. In Fig. 4.3, we show the

94

(a) SN2017fck   **(b)** SN2019cmv
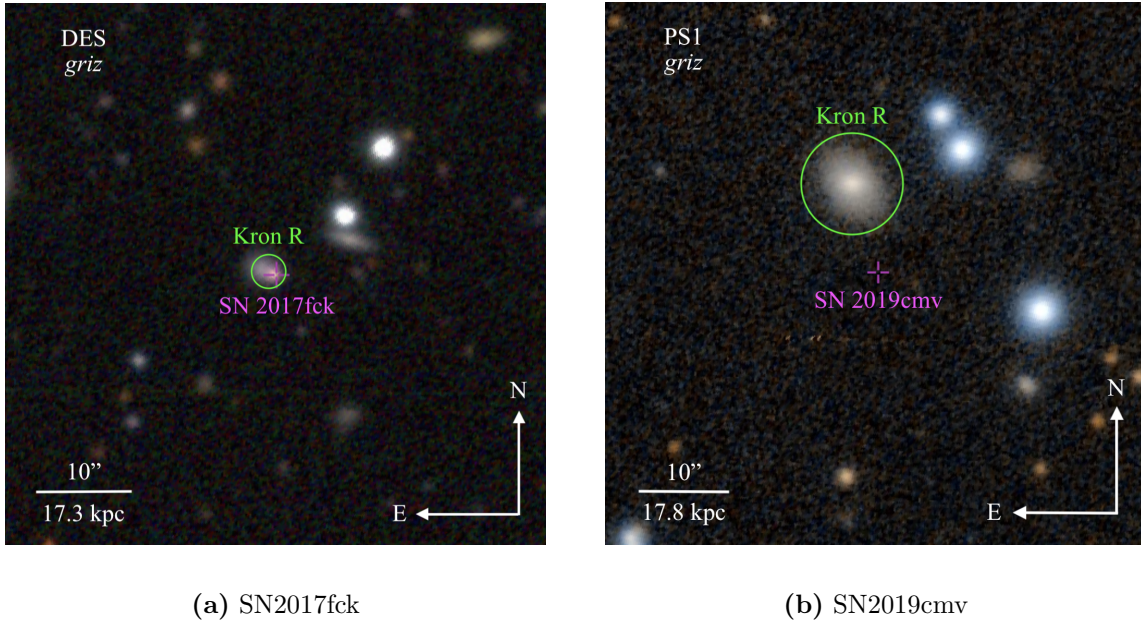
Figure 4.3: Archival $1'\!.0 \times 1'\!.0$ color composites of SNe 2017fck and 2019cmv sites and their host galaxies, retrieved via the Aladin Sky Atlas (Bonnarel et al. 2000; Boch & Fernique 2014). The each SN location and its host galaxy are marked respectively by the purple crosshair and the green circle with a Kron radius. Note that SN 2017fck is within its host galaxy's Kron radius, while SN 2019cmv is at 1.8 Kron radii away from its probable host galaxy.

archival DES and PS1 color-composite images of the SN location with the potential host galaxies marked with their Kron radii. The host galaxy association is straightforward for SN 2017fck as it is located within the Kron radius of its compact host. In contrast, SN 2019cmv is located at 18.3 kpc (1.81 Kron radii) away from its potential elliptical galaxy, making the association somewhat uncertain, especially given the SLSN nature.

In order to strength the host galaxy identification, we obtained a spectrum of the potential host for each SN to measure its redshift. The host galaxy spectra resemble that of typical star-forming and elliptical galaxies for SN 2017fck and 2019cmv, respectively (Fig. 4.2). We measure host galaxy lines by fitting a Gaussian profile to each line. This yields weighted averages of $z = 0.09456 \pm 0.00004$ and 0.0974 ± 0.0004 respectively for the potential hosts of SNe 2017fck and 2019cmv, which agrees well with the SN redshifts.

Thus, we associate these as the host galaxies in this work. However, we also note that SLSNe are preferentially hosted in faint galaxies ($-13.5 \gtrsim M_g \gtrsim -16.5$; Perley et al. 2016), and a ultra-faint host galaxy for SN 2019cmv (below the PS1 detection limit of $M_g \gtrsim -13.8$ at the SN redshift) cannot be ruled out.

For SN 2017fck, we place the host galaxies in the BPT diagrams based on the line ratios of [O III] $\lambda5007$/Hβ, [N II] $\lambda6583$/Hα, and [S II] $\lambda6717$/Hα. According to the Kewley et al. (2006) classification scheme, the host galaxy lies in the star-forming region in the BPT diagrams. Thus, we estimate an SFR from the Hα luminosity using the Kennicutt (1998) calibration, giving $0.4 \pm 0.1 \, M_\odot \, \mathrm{yr}^{-1}$. We also estimate a host galaxy metallicity from the measured line ratios and various estimates using PyMCZ. This yields a weighted average of $12 + \log_{10}(\mathrm{O/H}) = 8.13$, roughly corresponding to $0.2 \, Z_\odot$ (Asplund et al. 2009).

In order to extract the host galaxy properties of SN 2019cmv as well as SN 2017fck, we perform galaxy SED modeling with Prospector (Johnson et al. 2021). We follow the procedures described in Schulze et al. (2021), assuming a linear-exponential star formation history (SFH $\propto t \times e^{-t/\tau}$, where t is the age and τ is the e-folding timescale of SFH), the Chabrier (2003) IMF, the Calzetti et al. (2000) extinction model, and the Byler et al. (2017) ionized gas model. Then the galaxy parameters[1]: stellar mass ($M_\star$), age, τ, extinction, and metallicity were inferred in a Bayesian way with emcee (Foreman-Mackey et al. 2013). To construct SED, we retrieve the host galaxy optical photometry from DES DR2 and PS1 DR2, and IR photometry from the Two Micron All Sky Survey (2MASS; Skrutskie et al. 2006) and the Wide-field Infrared Survey Explorer (WISE; Wright et al. 2010).

The host galaxy of SN 2017fck is a low-mass ($\log[M_\star(M_\odot)] \simeq 8.6$), star-forming galaxy ($\log[\mathrm{SFR}(M_\odot \, \mathrm{yr}^{-1})] \simeq -0.4$–$0.1$) at a subsolar metallicy ($\log[Z(Z_\odot)] \simeq -0.6$),

---

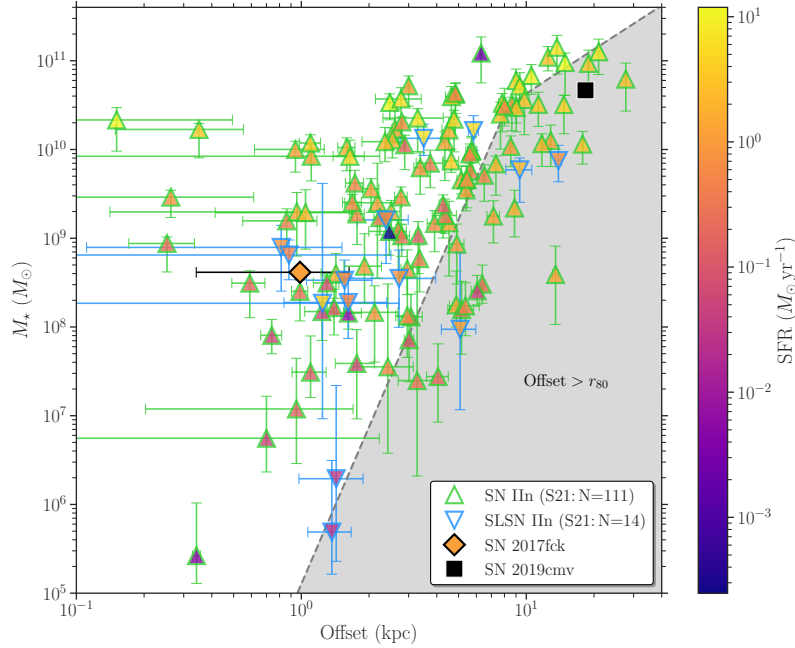[1]For SN 2017fck, the metallicity is fixed at the measured value from the host emission lines.

Figure 4.4: Comparison of the host stellar masses ($M_\star$) and offsets of SNe 2017fck and 2019cmv with the PTF sample from Schulze et al. (2021 S21), color coded by the star formation rate (SFR). SN 2019cmv is colored black since its SFR is well outside the sample range ($\log[\mathrm{SFR}\,(M_\odot\,\mathrm{yr}^{-1})] \simeq -9$). Error bars denote 1σ uncertainties. The gray shaded region shows where the offset is larger than the 80% light radius (r_{80}) of the host galaxy given its stellar mass (Miller et al. 2019; Mowla et al. 2019). Note that SN 2017fck appears consistent with the SN IIn and SLSN IIn samples, while SN 2019cmv seems an outlier due to its low SFR.

typical of SLSN host galaxies (Perley et al. 2016), while that of SN 2019cmv is a massive ($\log[M_\star(M_\odot)] \simeq 10.7$) elliptical galaxy ($\log[\mathrm{SFR}(M_\odot\,\mathrm{yr}^{-1})] \simeq -9$) at a subsolar metallicity ($\log[Z(Z_\odot)] \simeq -0.5$). In Fig. 4.4, we show the comparison of the $M_\star$, SN offsets, and SFR of the host galaxies of SNe 2017fck and 2019cmv with the Palomar Transient Factory (PTF) sample from Schulze et al. (2021). The host galaxy of SN 2017fck lies in the typical regions covered by SNe IIn and SLSNe IIn. Although the large host offset of SN 2019cmv alone does not stand out, the host galaxy is still an outlier given its low SFR. In this context, we consider the Ia-CSM origin as a viable scenario. We note that SNe Ia-CSM are also generally hosted in spiral or dwarf galaxies (Silverman et al. 2013

b), but longer delay times are expected for the SN Ia-CSM progenitor systems than for the typical SLSN-II massive progenitors (e.g., Ablimit 2021).

4.4.2 Spectral Evolution

We use the spectral library fitting code GEneric cLAssification TOol (GELATO; Harutyunyan et al. 2008) to cross-correlate the spectra of SNe 2017fck and 2019cmv to other well-observed interacting SNe. In Fig. 4.5, we show good spectral matches to SNe 2017fck and 2019cmv, namely SN IIn 1998S (Fassia et al. 2001) and SNe Ia-CSM 1997cy (Turatto et al. 2000) and 2005gj (Prieto et al. 2007), at four different phases.

In the early phase ($\sim$ 40 days after explosion), the spectra are characterized by the narrow Balmer-series emission lines on top of the blue continuum. For SN 2017fck, similar narrow Balmer-series and He I P Cygni features to SN 2008S are also seen. During $\sim$ 80–110 days after explosion, weak He I emission lines appear, Hα emission lines become broader and asymmetric with the suppressed red wing, and the Hα/Hβ flux ratio increases, typical of SNe Ia-CSM (Silverman et al. 2013b). The spectral evolution of SN 2019cmv is slower compared to SNe 2017fck and 2005gj in that the continuum and Hβ emission line stay bluer and stronger, respectively, which might suggest a different level of CSM contamination on the underlying SN (Leloudas et al. 2015). Even at $\sim$ 240 days after explosion, the spectra of SNe 2017fck and 1997cy are not yet fully nebular, showing the broad Hα and Ca II NIR triplet emission lines on the persistent continuum due to CSM interaction. To diagnose the underlying SN composition, fully nebular spectra at later epochs ($\gtrsim$ 400 days after explosion; see § 4.4.3) would be necessary, as was done for SLSN-II 2006gy, suggesting a possible Ia-CSM origin (Jerkstrand et al. 2020).

We measure Hα and Hβ line fluxes of SNe 2017fck and 2019cmv by fitting a multi-Gaussian profile (to account for the asymmetry) to each line. Since no obvious Hβ line
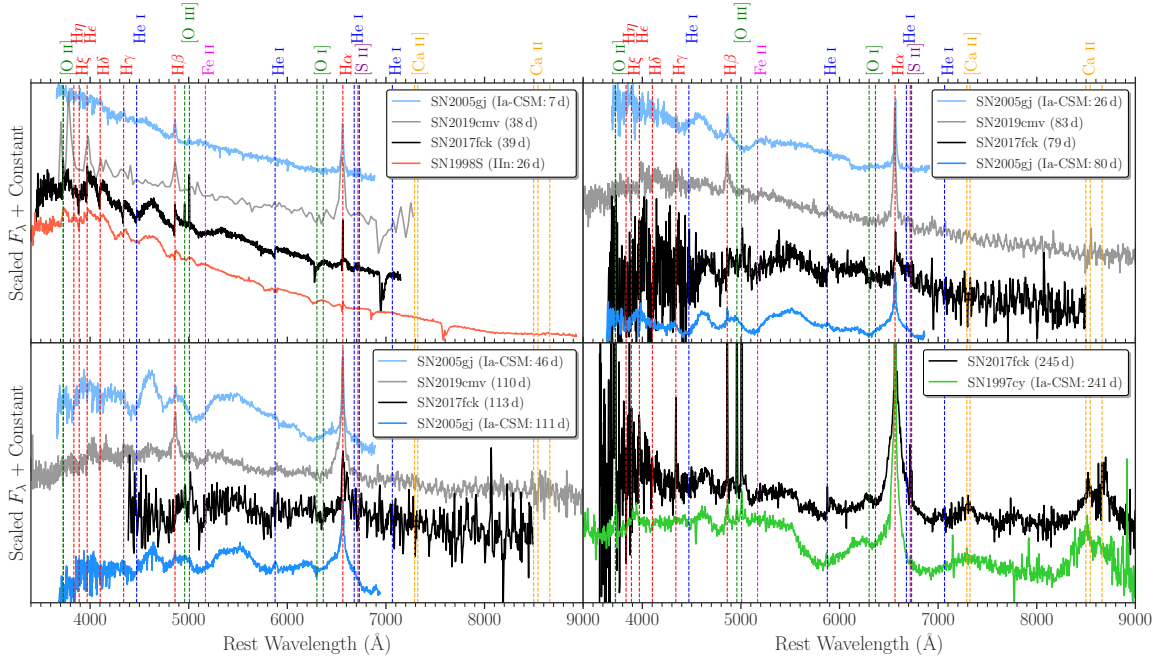
Figure 4.5: Spectral comparisons of SNe 2017fck and 2019cmv at four different phases with SN IIn 2008S (Fassia et al. 2001) and SNe Ia-CSM 1997cy (Turatto et al. 2000) and 2005gj (Prieto et al. 2007), revrived via WISeREP. The spectral matches for SNe 2019cmv and 2017fck were identified by GELATO and plotted at the top and bottom in each panel, respectively. The spectra are characterized by the narrow Balmer-series emission lines on top of the blue continuum at ∼ 40 d, by the broad asymmetric Hα emission lines with the suppressed red wing and increasing Hα/Hβ flux ratios during ∼ 80–110 d, and then by the broad Ca II NIR triplet as well as Hα emission lines on the persistent continuum at ∼ 240 d. Note that the spectral evolution of SN 2019cmv is slower compared to SNe 2017fck and 2005gj in terms of the continuum and emission lines.

is seen in the spectra of SN 2017fck, the upper limit at each epoch is estimated assuming the same FWHM as Hα. In Fig. 4.6, we show the comparison of the Hα/Hβ flux-ratio evolution of SNe 2017fck and 2019cmv with well-observed interacting SNe. SLSNe-II CSS121015 is included in the comparison because of its overall spectral similarities to SN Ia-CSM 2005gj (Benetti et al. 2014). As seen in the IIn and Ia-CSM cumulative fractions from the Silverman et al. (2013b) sample, Hα/Hβ flux ratios are generally smaller for SNe IIn (e.g., SN 1998S) than for SNe Ia-CSM (e.g., SN 2005gj), possibly due to the higher kinetic energy budgets from core-collapse than thermonuclear explosions.
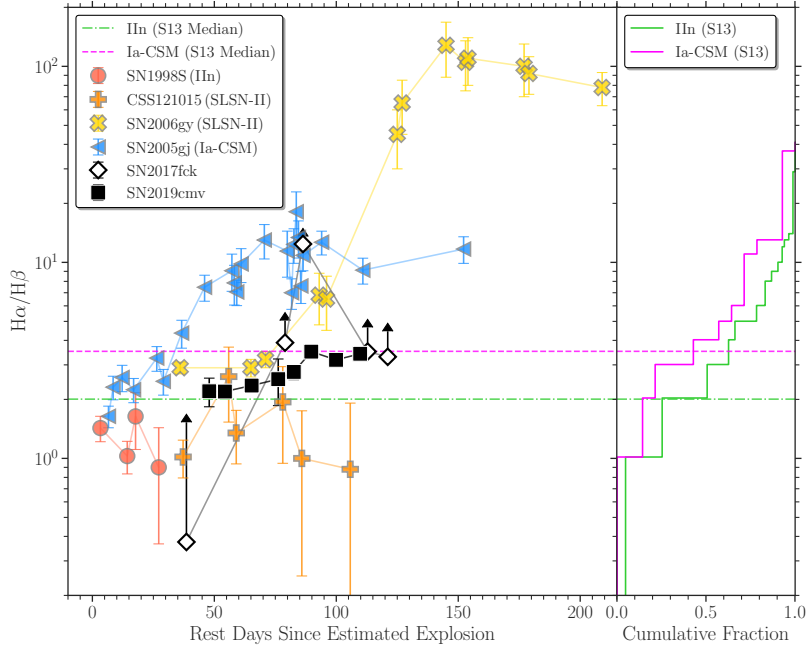
Figure 4.6: Comparison of the Hα/Hβ flux-ratio evolution of SNe 2017fck and 2019cmv with SN IIn 2008S (Fassia et al. 2001), SLSNe-II CSS121015 (Benetti et al. 2014) and 2006gy (Smith et al. 2010), and SN Ia-CSM 2005gj (Prieto et al. 2007), as well as the SN IIn and Ia-CSM cumulative fractions from the Silverman et al. (2013b S13) sample. Error bars and arrows respectively denote 1σ uncertainties and limits. The median of Hα/Hβ flux ratio over all epochs is smaller for SNe IIn (e.g., SN 1998S) than for SNe Ia-CSM (e.g., SN 2005gj). Note the increasing Hα/Hβ flux ratios (and limits) of SNe 2017fck and 2019cmv that are above the SN IIn median.

SNe 2017fck and 2019cmv show the increasing Hα/Hβ flux ratios (and limits), which appears slightly more consistent with those of SNe Ia-CSM than IIn, although not conclusive given the wide overlapping SN Ia-CSM and IIn distributions. It is also interesting to note the large increasing Hα/Hβ flux ratios of SN 2006gy, which might also support its possible Ia-CSM origin.

4.4.3   Bolometric Light Curves

We fit a blackbody SED to every epoch of photometry containing at least three filters (excluding the i band owing to strong Hα contamination at the SN redshift) obtained

within 0.3 days of each other to estimate blackbody temperature and radius. Then we integrate the fitted blackbody SED over the full (and optical: 3250–8900Å) wavelength range to obtain bolometric (and pseudobolometric) luminosity at each epoch. For the early epochs where only *Gaia G*-band photometry is available, we covert its magnitude to pseudobolometric luminosity assuming a constant zero pseudobolometric correction with a 20% uncertainty, given the comparably wide optical wavelength coverage.

In Fig. 4.7, we show the comparison of the pseudobolometric light curves of SNe 2017fck and 2019cmv with well-observed SLSNe-II and SNe Ia-CSM. PTF11kx is a transitional SN Ia/Ia-CSM[2] in the sense that it initially showed Ia-dominated spectra and then transitioned to CSM-dominated spectra (Dilday et al. 2012; Silverman et al. 2013a), which is different from the other SNe Ia-CSM in the comparison with CSM-dominated spectra throughout their evolution. Except PTF11kx, the light-curve characteristics of SNe 2017fck and 2019cmv are similar to those of the other SLSNe-II and SNe Ia-CSM in that they show bright maximums ($\gtrsim 10^{43}\,\mathrm{erg\,s^{-1}}$) and superlinear post-maximum declines (for $\gtrsim 100$ days) powered by CSM interaction. For SNe Ia-CSM 1997cy, 1999E, and 2012ca, the late-time observations reveal the light-curve drops from the linear decline phase around 400–600 days, which may indicate the end of CSM-dominated phase and the beginning of nebular phase.

In order to quantify their light-curve characteristics, we measure the maximum luminosity ($L_{\mathrm{opt,max}}$) and rise time ($t_{\mathrm{opt,rise}}$) of each SN by fitting a parabola around the peak when available. Then we fit a line from the peak to decline up to 100 days post maximum to measure the decline slope ($s_{\mathrm{opt,postmax}}$). When the peak is not observed, we use the first data point as the lower and upper limits of $L_{\mathrm{opt,max}}$ and $t_{\mathrm{opt,rise}}$, respectively, and measure $s_{\mathrm{opt,postmax}}$ from the first data point assuming a constant linear decline from

---

[2]SN 2002ic is another transional SN Ia/Ia-CSM (Hamuy et al. 2003; Deng et al. 2004; Wood-Vasey et al. 2004), but not included in the comparison due to the sparse multi-band light-curve sampling.
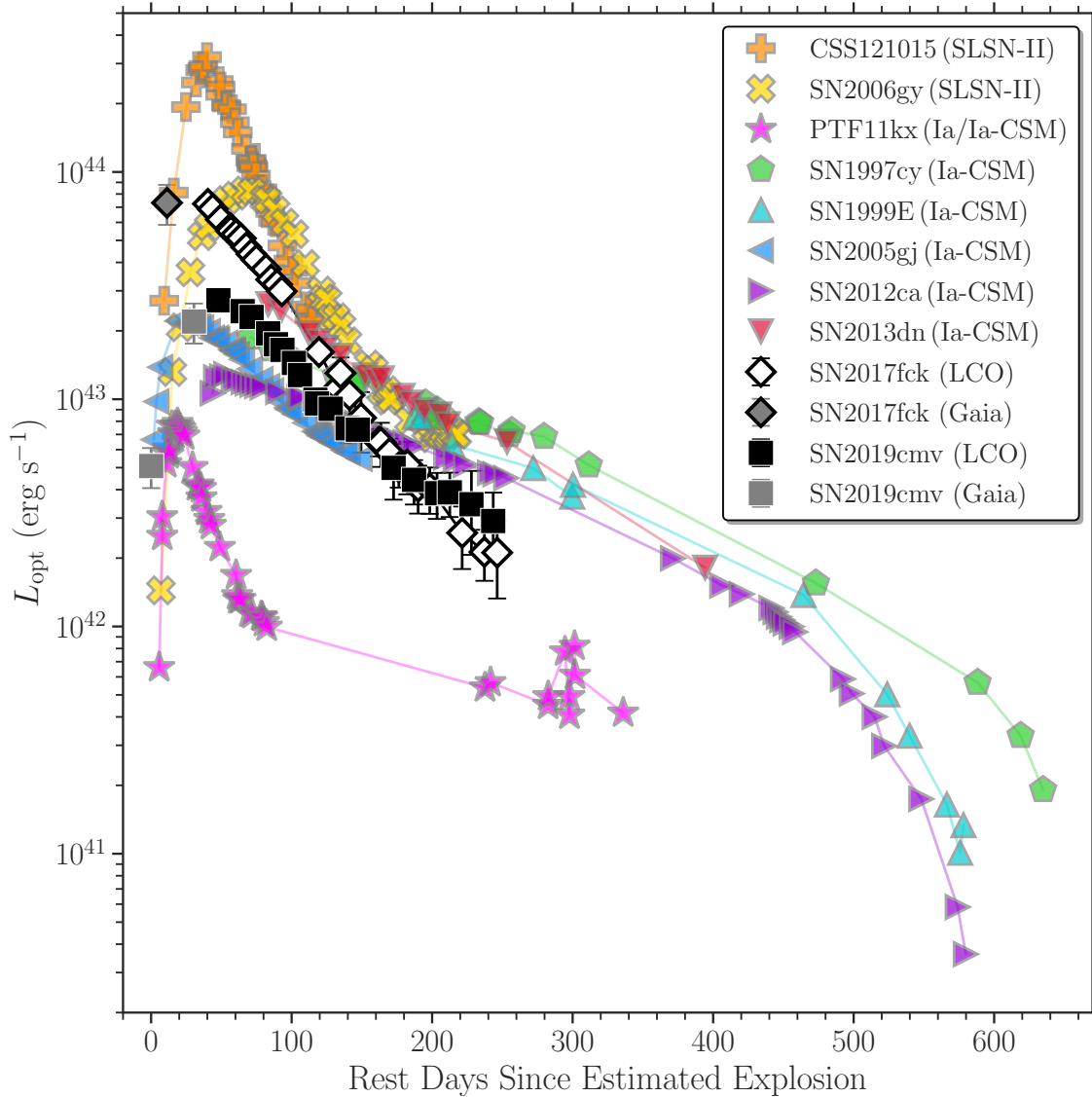
Figure 4.7: Comparison of the pseudobolometric light curves of SNe 2017fck and 2019cmv with SLSNe-II CSS121015 (Benetti et al. 2014) and 2006gy (Jerkstrand et al. 2020), and SNe Ia-CSM PTF11kx (Dilday et al. 2012), 1997cy (Turatto et al. 2000), 1990E (Rigon et al. 2003), 2005gj (Prieto et al. 2007), 2012ca (Inserra et al. 2016), and 2013dn (Fox et al. 2015); the possible Ia-CSM origin has also been discussed for CSS121015 and SN 2006gy. For SNe 2017fck and 2019cmv, the pre-maximum and post-maximum luminosity is calculated from the *Gaia G*-band photometry and the LCO multi-band photometry, respectively. Error bars denote 1σ uncertainties. Note that except the transitional SN Ia/Ia-CSM PTF11kx, the other SLSNe-II and SNe Ia-CSM, including SNe 2017fck and 2019cmv, are characterized by the bright maximum ($\gtrsim 10^{43}$ erg s^{-1}) and superlinear post-maximum declines (for $\gtrsim 100$ days).
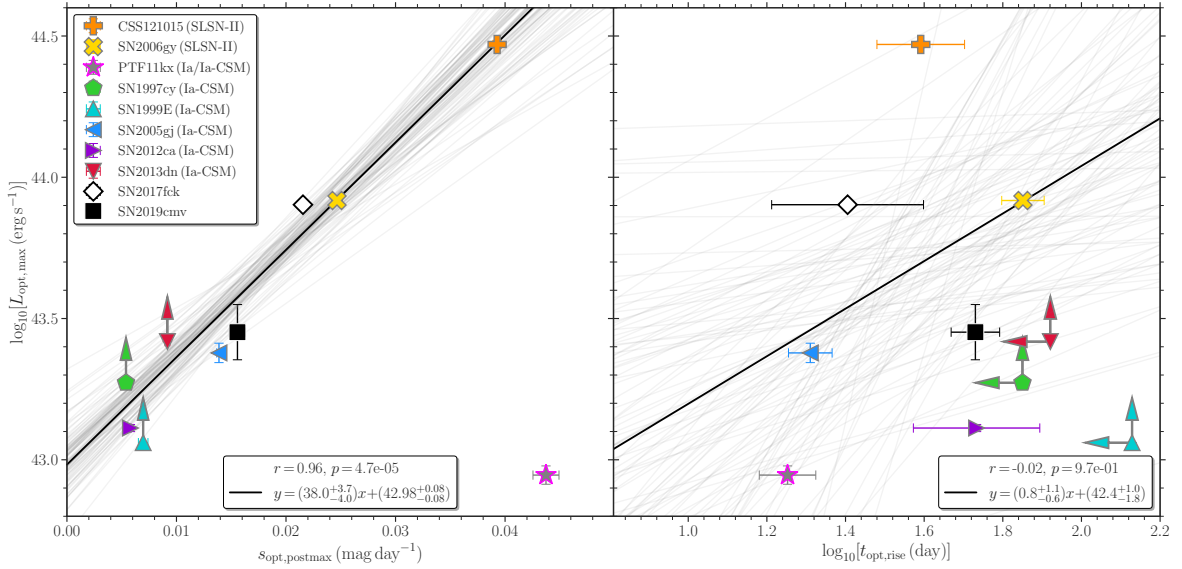
Figure 4.8: Pearson correlation tests (coefficient r and p-value) and liner fits between the maximum pseudobolometric luminosity ($L_{\rm opt,max}$), post-maximum decline slope ($s_{\rm opt,postmax}$), and rise time to the maximum ($t_{\rm opt,rise}$) of SNe 2017fck and 2019cmv with the same sample as in Fig. 4.7, except PTF11kx (grayed star) given its transitional nature. Error bars and arrows respectively denote 1σ uncertainties and limits. The gray transparent and black solid lines respectively represent randomly drawn 100 fits and the best fits from `emcee`. Note the significant correlation between $L_{\rm opt,max}$ and $s_{\rm opt,postmax}$, and the negligible correlation between $L_{\rm opt,max}$ and $t_{\rm opt,rise}$.

the peak.

In Fig. 4.8, we show the comparisons of the measured $L_{\rm opt,max}$, $t_{\rm opt,rise}$, and $s_{\rm opt,postmax}$. Except PTF11kx, a positive trend in $L_{\rm opt,max}$ vs. $s_{\rm opt,postmax}$ can be seen; brighter SNe decline faster. The points are more scattered in $L_{\rm opt,max}$ vs. $t_{\rm opt,rise}$, likely due to poorly constrained explosion epochs of some sample SNe. We then perform Pearson correlation tests for $L_{\rm opt,max}$ vs. $s_{\rm opt,postmax}$ and $L_{\rm opt,max}$ vs. $t_{\rm opt,rise}$, finding a significant and negligible correlations, respectively. We also perform linear fitting in a Bayesian way, assuming flat priors to all parameters, with `emcee`. The tightness of the linear fits also suggests a significant and negligible correlations respectively for $L_{\rm opt,max}$ vs. $s_{\rm opt,postmax}$ and $L_{\rm opt,max}$ vs. $t_{\rm opt,rise}$. These correlations may indicate some similarities in the progen-

itor systems and CSM configurations for the sample SLSNe-II and SNe Ia-CSM, which
we try to reproduce with numerical Ia-CSM light-curve modeling in §4.5.

4.5   SN Ia-CSM Light-Curve Modeling

We construct a numerical light-curve model grid of SNe Ia that collide to dense CSM
to investigate their expected properties. For this purpose, we use the one-dimensional
multi-group radiation hydrodynamics code STELLA. The code has been used for numerical
modeling of SNe powered by CSM interaction (e.g., Moriya et al. 2013; Noebauer et al.
2016; Hiramatsu et al. 2021a). It allows us to calculate the psudobolometric luminosity
to compare with observations.

We take the W7 ejecta model of SNe Ia (Nomoto et al. 1984) and attach CSM on
top of the W7 ejecta. The W7 ejecta model has the ejecta mass of $1.38\,M_{\odot}$, nickel mass
of $0.58\,M_{\odot}$, and kinetic energy of $1.3 \times 10^{51}\,\mathrm{erg}$. We assume solar metallicity CSM with
three different density distributions: $\rho_{\mathrm{CSM}}(r) \propto r^{-2}$, r^{-1}, and constant. We change the
CSM density and radius to have different CSM masses (M_{CSM}). The CSM parameters are
chosen so that M_{CSM} does not become too large (0.5–$21.3\,M_{\odot}$). We assume large CSM
radii (0.5–$3.5 \times 10^{16}\,\mathrm{cm}$) because the CSM interaction signatures persist for a long time
in the SNe we are interested in (Fig. 4.7). Average mass-loss rates ($\dot{M}$) can be estimated
by assuming a steady wind-like mass loss with a velocity (v): $\dot{M} = M_{\mathrm{CSM}}/(r/v)$.

In Fig. 4.9, we show the comparisons of the psudobolometric light curves of SNe 2017fck
and 2019cmv with the W7+CSM models. In these comparisons, we shift the refer-
ence epoch to the estimated maximum for clarity. The light curves of SNe 2017fck and
2019cmv are obviously brighter and broader than the pure W7 model. The W7+CSM
models with all the density distributions cover comparable maximum luminosities to
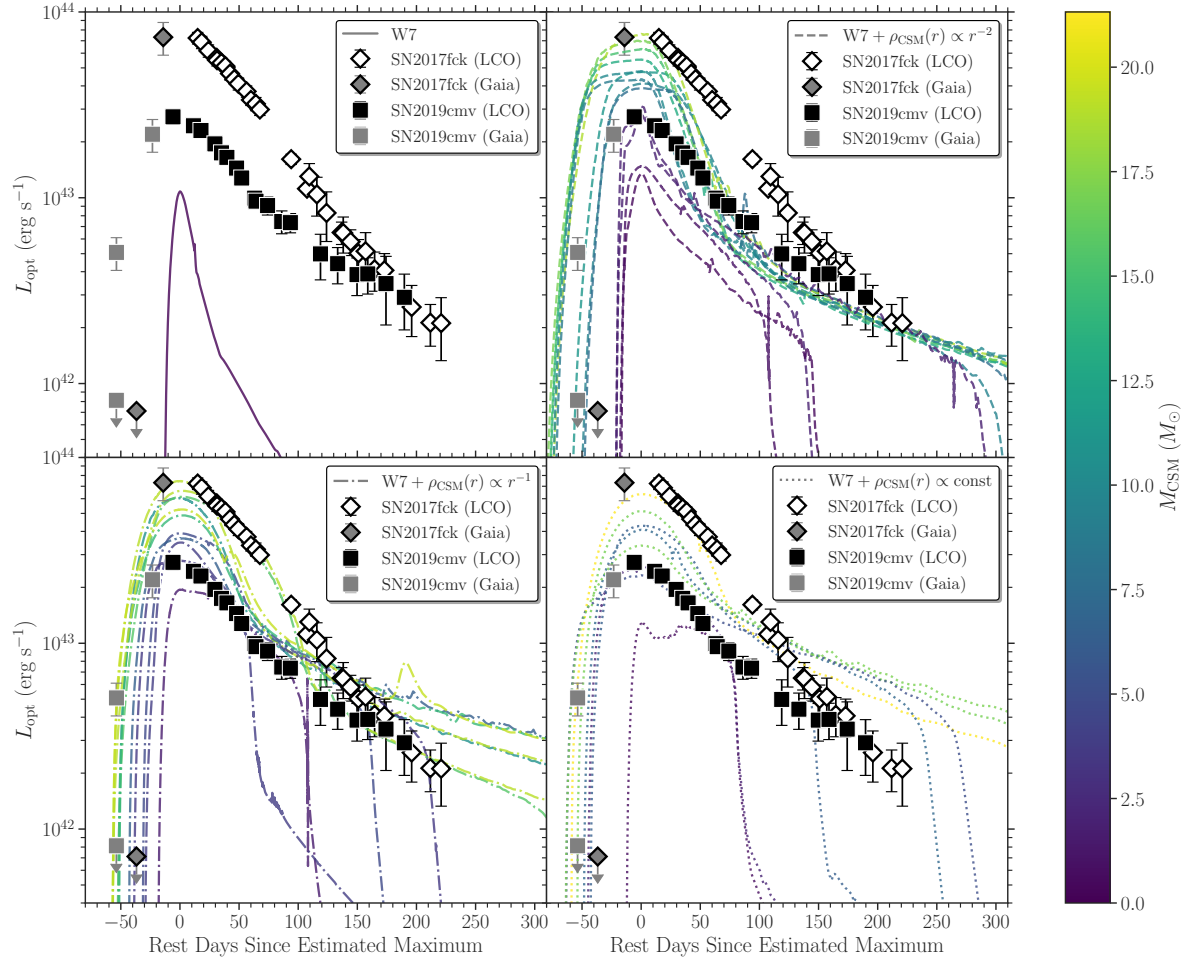SNe 2017fck and 2019cmv. In general, the W7+CSM models with the r^{-2} density dis-

Figure 4.9: Comparisons of the pseudobolometric light curves of SNe 2017fck and 2019cmv (as in Fig. 4.7) with the W7+CSM models with three different CSM density distributions, color coded by the CSM mass (M_{CSM}). The downward arrows denote the last non-detection limits from *Gaia*. The CSM models with the r^{-2} (and constant) distributions decline too rapidly (and slowly) after the peak compared to SNe 2017fck and 2019cmv. Note that the peak luminosities and decline rates of SNe 2017fck and 2019cmv are best reproduced by the CSM models with the r^{-1} distribution with $M_{CSM} = 15.7\,M_\odot$ and $3.6\,M_\odot$, respectively, although the rise times differ by $\sim \pm 15$ days.
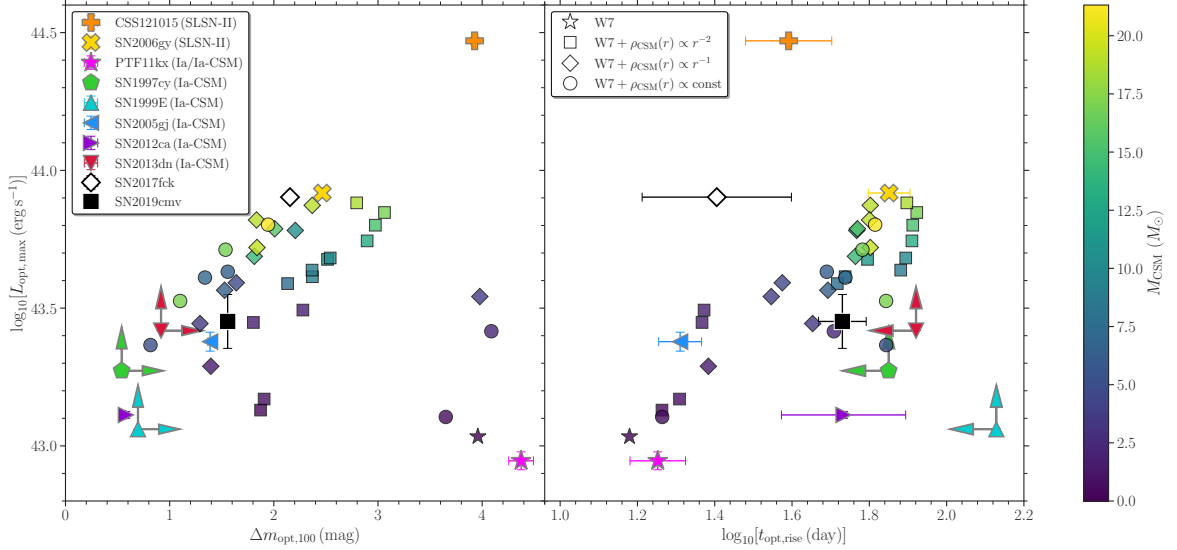
Figure 4.10: Comparisons of the maximum pseudobolometric luminosity ($L_{\rm opt,max}$), post-maximum decline rate ($\Delta m_{\rm opt,100}$), and rise time to the maximum ($t_{\rm opt,rise}$) of SNe 2017fck and 2019cmv with the same sample and W7+CSM models as in Figs. 4.7 & 4.9, respectively. The pure W7 model is the closest match to PTF11kx given its early Ia-dominated evolution. The W7+CSM models span a wide $L_{\rm opt,max}$ range, covering most of the sample except CSS121015. Note that the W7+CSM models are able to reproduce the observed correlation between $L_{\rm opt,max}$ and $\Delta m_{\rm opt,100}$, and also predict a correlation between $L_{\rm opt,max}$ and $t_{\rm opt,rise}$.

tribution decline faster from the maximum due to the less dense outer CSM than the other density distributions. On the other hand, the W7+CSM models with the constant density distribution decline slower due to the denser outer CSM region. The W7+CSM models with the r^{-1} density distribution best reproduces the maximum luminosities and declines of SN 2017fck and 2019cmv with $M_{\rm CSM} = 15.7 M_\odot$ and $3.6 M_\odot$, respectively. One caveat to note is that the model rise times are slower and faster than those of SNe 2017fck and 2019cmv, respectively, by ~ 15 days, which may require an additional component, such as a shell or cavity, in close proximity to the progenitor (e.g., Wood-Vasey et al. 2004).

In Fig. 4.10, we show the comparisons of $L_{\rm opt,max}$, $t_{\rm opt,rise}$, and post-maximum decline

106

rate for 100 days $(\Delta m_{\mathrm{opt,100}})$[3] of the W7+CSM models with the observed SLSN-II and SN Ia-CSM sample. The transitional SN Ia/Ia-CSM PTF11kx lies in the similar parameter space to the pure W7 model given its early Ia-dominated evolution. The W7+CSM models with the reasonable M_{CSM} $(\lesssim 20\,M_\odot)$ range cannot occupy the parameter space of SLSN-II CSS121015, supporting the massive star origin despite the spectral similarities to SN Ia-CSM 2005gj, as also suggested by Benetti et al. (2014). In contrast, the W7+CSM models with $M_{\mathrm{CSM}} \sim 15\,M_\odot$ can reproduce the parameter space of SLSN-II 2006gy reasonably well, indicating the possible Ia-CSM origin, which is in agreement with Jerkstrand et al. (2020).

In addition, the W7+CSM models reproduce a positive correlation in $L_{\mathrm{opt,max}}$ vs. $\Delta m_{\mathrm{opt,100}}$ observed in the SN Ia-CSM sample, suggesting that the light-curve diversity in SNe Ia-CSM $(L_{\mathrm{opt,max}} \leq 10^{44}\,\mathrm{erg\,s^{-1}})$ can be explained by the diversity in CSM distributions (i.e., $M_{\mathrm{CSM}} \sim 1\text{–}15\,M_\odot$). The models also predict a positive correlation in $L_{\mathrm{opt,max}}$ vs. $t_{\mathrm{opt,rise}}$, which needs to be tested with more SNe Ia-CSM with better-constrained explosion epochs. Another constraining observable would be a drop from the linear decline phase, as observed in SNe 1997cy, 1999E, and 2012ca, which should correlate with the CSM extension. We also note that the inferred CSM mass range for SNe Ia-CSM would be lowered (or raised) if we assume a more (or less) luminous underlying SN Ia model, such as that of 91T-like (or 91bg-like). This might then explain the spectral differences seen in SNe Ia-CSM (Leloudas et al. 2015; e.g., the stronger SN Ia-like continuum of SN 2017fck due to an underlying 91T-like SN, compared to that of SN 2019cmv due to an underlying 91bg-like SN).

---

[3]The choice of $\Delta m_{\mathrm{opt,100}}$, instead of $s_{\mathrm{opt,postmax}}$, has been made due to numerical noise in some models, making it harder to measure the linear slope.

4.6   Discussion and Summary

4.6.1   SN Ia-CSM Progenitor System

The W7+CSM light-curve models can cover the observed SN Ia-CSM parameter space with various CSM distributions (i.e., $M_{\rm CSM} \sim 1$–$15 \, M_{\odot}$), but a remaining question is whether SN Ia progenitor systems are able to produce such high-mass CSM. One possible scenario might be a binary progenitor system consisting of a CO WD and giant ($< \, 8 \, M_{\odot}$) or supergiant ($\geq \, 8 \, M_{\odot}$) companion star that undergoes common envelope (CE) evolution and explodes by a core merger inside the CE (e.g., Terman et al. 1994; Taam & Sandquist 2000; Sabach & Soker 2014; Soker 2019; Ablimit 2021). From binary population synthesis calculations, CE masses of $\sim \, 2$–$7 \, M_{\odot}$ and $\sim \, 6$–$12 \, M_{\odot}$ and delay times of ~ 0.1–$10 \, {\rm Gyr}$ and ~ 30–$120 \, {\rm Myr}$ could be expected with a giant and supergiant companion star, respectively (Ablimit 2021). Therefore, CE evolution could in principle roughly span the inferred CSM mass range of SNe Ia-CSM from the W7+CSM models, although detailed simulations are necessary to confirm if the final product of CE evolution is indeed a core merger inducing an SN Ia explosion. In this scenario, the progenitor system of SN 2017fck ($M_{\rm CSM} \sim 15 \, M_{\odot}$) would be a CO WD + supergiant, while that of SN 2019cmv ($M_{\rm CSM} \sim 3 \, M_{\odot}$) would be a CO WD + giant whose longer delay time would then allow the large offset from the potential elliptical host galaxy. However, it is less clear if the inferred r^{-1} density distribution for SNe 2017fck and 2019cmv could be realized by the CE scenario.

4.6.2   SN Ia-CSM Signatures

As the summary of this work, we check the observed and modeled properties of SNe 2017fck and 2019cmv against the SN Ia-CSM signatures from Silverman et al. (2013

SN	Peak Luminosity $(-21.3 \leq M_R \leq -19)$ & Rise Time $(\sim 20\text{--}40\,\mathrm{days})$	Spectral Homogeneity: Hα Ca II NIR triplet diluted SN Ia	Hα Profile: narrow P-Cygni strong fluctuations suppressed red wing	Line Flux: weak He I weak Hβ large Hα/Hβ	UV MIR no radio no X-ray	Mass Loss $\sim 10^{-1}\,M_\odot\,\mathrm{yr}^{-1}$	Host Galaxy: spiral or dwarf
2017fck	✓	✓	✓	✓	–	✓	✓
2019cmv	✓	?	✓?	✓	–	✓	✗

Figure 4.11: Silverman et al. (2013b) SN Ia-CSM Signature Checklist. Check marks, check+question marks, and cross marks (respectively) indicate observations consistent, perhaps consistent, and inconsistent with the signatures. Dashed lines indicate the lack of observational constraints, and lone question marks indicate unknowns.

b). The checklist is shown in Fig. 4.11 and discussed in the following.

- Peak absolute magnitudes of $-21.3 \leq M_R \leq -19$ and rise times of $\sim 20\text{--}40$ days are observed for SNe Ia-CSM. In G band (with the similar effective wavelength to R band; Fig. 4.1), SNe 2017fck and 2019cmv show the peak magnitudes of $-21.8 \leq M_G \leq -20.4$ and rise times of $\sim 25\text{--}50$ days that are slightly brighter and longer, respectively, but still comparable to the SN Ia-CSM population. These are reaching into the SLSN regime.

- Spectral homogeneity is seen for SNe Ia-CSM in that they show strong and broad Hα ($\sim 2{,}000\,\mathrm{km\,s^{-1}}$) and Ca II NIR triplet ($\sim 10{,}000\,\mathrm{km\,s^{-1}}$) on top of a diluted SN Ia-like "quasi-continuum." The late-time (~ 250 d) spectrum of SN 2017fck show all the above features (Fig. 4.5). The spectra of SN 2019cmv (observed only up to ~ 110 d) are dominated by Hα, not showing a clear quasi-continuum or Ca II NIR triplet (Fig. 4.2). On the other hand, if SLSN-II 2006gy is indeed an SN Ia-CSM, some spectral heterogeneity within the SN Ia-CSM population is expected.

- For the Hα profiles of SNe Ia-CSM, narrow P Cygni profiles ($50\text{--}100\,\mathrm{km\,s^{-1}}$), fluctuating emission profiles (until $\sim 100\text{--}150$ days after maximum), and suppressed red wings (after $\sim 75\text{--}100$ days after maximum) are observed. SNe 2017fck and 2019cmv show Hα fluctuations and suppressed red wings (Fig. 4.2). The early-time

(~ 40 d) spectrum of SN 2017fck show a narrow Hα P Cygni profile as well, while the spectral resolutions of the other SN 2017fck and 2019cmv spectra are not high enough to resolve it (Fig. 4.5).

- Weak He I and Hβ emission lines and large Hα/Hβ flux ratios are observed for SNe Ia-CSM. SN 2017fck and 2019cmv show all the above features (Figs. 4.5 & 4.6). However, we note that the observed Hα/Hβ flux ratios of SNe IIn and Ia-CSM cover a wide range, making the diagnosis somewhat inconclusive. SLSN-II 2006gy also shows large Hα/Hβ flux ratios.

- Multi-wavelength observations of SNe Ia-CSM has revealed UV emission without radio or X-ray counterparts (within the first few months) and MIR emission (~ 0.5–2 years). Unfortunately, we do not have any of the above constraints for SNe 2017fck and 2019cmv.

- Using rise times and X-ray upper limits with many analytical assumptions, wind mass-loss rates of $\sim 10^{-1}\,M_\odot\,\mathrm{yr}^{-1}$ can be inferred for SNe Ia-CSM. With the numerical CSM light-curve modeling, we infer large CSM masses of ~ 3–$15\,M_\odot$ with average mass-loss rates of $(0.7$–$5) \times 10^{-1}\,M_\odot\,\mathrm{yr}^{-1}$ for SNe 2017fck and 2019cmv (Fig. 4.9). Similarly, the models can cover most of the SN Ia-CSM parameter space with a CSM mass range of ~ 1–$15\,M_\odot$ (Fig. 4.10).

- Spiral galaxies (with MW-like luminosities and solar metallicities) and dwarf irregulars (with Magellanic Clouds-like luminosities and subsolar metallicities) are identified for SNe Ia-CSM. The host galaxy of SN 2017fck is a low-mass, star-forming galaxy at a subsolar metallicy. In contrast, the host galaxy of SN 2019cmv is a massive elliptical galaxy at a subsolar metallicity (Figs. 4.3 & 4.4), although a ultra-faint host galaxy ($M_g \gtrsim -13.8$) cannot be ruled out. Given the expected

longer delay times of SN Ia-CSM progenitor systems than typical SLSN-II massive progenitors, however, we consider the Ia-CSM origin more likely.

In addition to the Silverman et al. (2013b) SN Ia-CSM signatures, we suggest the linear light curves and correlations (Figs. 4.7 & 4.8) as possible signatures, which can also be reproduced by the numerical W7+CSM models with various density distributions (Figs. 4.9 & 4.10). With more well-observed samples, the late-time light-curve drops and nebular spectra would be another set of constraining signatures, probing the extent of CSM and underlying SN composition. As for CSM light-curve modeling, the effect of underlying SN Ia subtypes (e.g., 91T-like and 91bg-like) should also be explored.

SN 2017fck satisfy all the above SN Ia-CSM signatures where observations are available. SN 2019cmv may be missing some of the spectral signatures, but later observations are necessary to test them. With the possible addition of SNe 2017fck and 2019cmv to the SN Ia-CSM population, SNe Ia-CSM would cover wider light-curve parameter space, even into the SLSN regime ($L_{\rm opt,max} \leq 10^{44}\,{\rm erg\,s^{-1}}$), requiring the diversity in CSM distributions (i.e., $M_{\rm CSM} \sim 1\text{--}15\,M_\odot$) which might be produced during the CE phase of a WD and giant or supergiant companion stars.

Bibliography

Abbott, B. P., Abbott, R., Abbott, T. D., et al. 2017, ApJL, 848, L12

Ablimit, I. 2021, PASP, 133, 074201

Adamo, A., Smith, L. J., Gallagher, J. S., et al. 2012, MNRAS, 426, 1185

Adams, S. M., Kochanek, C. S., Gerke, J. R., Stanek, K. Z., & Dai, X. 2017, MNRAS, 468, 4968

Adams, S. M., Kochanek, C. S., Prieto, J. L., et al. 2016, MNRAS, 460, 1645

Aihara, H., Allende Prieto, C., An, D., et al. 2011, ApJS, 193, 29

Albareti, F. D., Allende Prieto, C., Almeida, A., et al. 2017, ApJS, 233, 25

Anderson, J. P., González-Gaitán, S., Hamuy, M., et al. 2014, ApJ, 786, 67

Anderson, J. P., Gutiérrez, C. P., Dessart, L., et al. 2016, A&A, 589, A110

Anderson, J. P., Dessart, L., Gutiérrez, C. P., et al. 2018, Nature Astronomy, 2, 574

Aniano, G., Draine, B. T., Hunt, L. K., et al. 2020, ApJ, 889, 150

Arcavi, I. 2017, Hydrogen-Rich Core-Collapse Supernovae, ed. A. W. Alsabti & P. Murdin (Cham: Springer International Publishing), 239–276

Arcavi, I., Hosseinzadeh, G., Hiramatsu, D., et al. 2018, Transient Name Server Classification Report, 2018-2082, 1

Arcavi, I., Gal-Yam, A., Cenko, S. B., et al. 2012, ApJL, 756, L30

Arcavi, I., Hosseinzadeh, G., Howell, D. A., et al. 2017, Nature, 551, 64

Armus, L., Heckman, T. M., Weaver, K. A., & Lehnert, M. D. 1995, ApJ, 445, 666

Asplund, M., Grevesse, N., Sauval, A. J., & Scott, P. 2009, ARA&A, 47, 481

Baldwin, J. A., Phillips, M. M., & Terlevich, R. 1981, PASP, 93, 5

Barbarino, C., Sollerman, J., Taddia, F., et al. 2020, arXiv e-prints, , arXiv:2010.08392

Barbon, R., Ciatti, F., & Rosino, L. 1979, A&A, 72, 287

Basinger, C. M., Kochanek, C. S., Adams, S. M., Dai, X., & Stanek, K. Z. 2020, arXiv e-prints, , arXiv:2007.15658

Beasor, E. R., & Davies, B. 2016, MNRAS, 463, 1269

Beasor, E. R., Davies, B., Smith, N., et al. 2020, MNRAS, 492, 5994

Bellm, E. C., Kulkarni, S. R., Graham, M. J., et al. 2019, PASP, 131, 018002

Benetti, S., Turatto, M., Balberg, S., et al. 2001, MNRAS, 322, 361

Benetti, S., Nicholl, M., Cappellaro, E., et al. 2014, MNRAS, 441, 289

Benvenuto, O. G., Panei, J. A., Nomoto, K., Kitamura, H., & Hachisu, I. 2015, ApJL, 809, L6

Berger, E., Soderberg, A. M., Chevalier, R. A., et al. 2009, ApJ, 699, 1850

Bersten, M. C., Benvenuto, O., & Hamuy, M. 2011, ApJ, 729, 61

Bianco, F. B., Modjaz, M., Oh, S. M., et al. 2016, Astronomy and Computing, 16, 54

Blinnikov, S., Lundqvist, P., Bartunov, O., Nomoto, K., & Iwamoto, K. 2000, ApJ, 532, 1132

Blinnikov, S. I., Eastman, R., Bartunov, O. S., Popolitov, V. A., & Woosley, S. E. 1998, ApJ, 496, 454

Blinnikov, S. I., Röpke, F. K., Sorokina, E. I., et al. 2006, A&A, 453, 229

Blondin, S., & Tonry, J. L. 2007, ApJ, 666, 1024

Boch, T., & Fernique, P. 2014, in Astronomical Society of the Pacific Conference Series, Vol. 485, Astronomical Data Analysis Software and Systems XXIII, ed. N. Manset & P. Forshay, 277

Boian, I., & Groh, J. H. 2019, A&A, 621, A109

—. 2020, MNRAS, 496, 1325

Bond, H. E., Bedin, L. R., Bonanos, A. Z., et al. 2009, ApJL, 695, L154

Bonnarel, F., Fernique, P., Bienaymé, O., et al. 2000, A&AS, 143, 33

Bostroem, K. A., Valenti, S., Horesh, A., et al. 2019, MNRAS, 485, 5120

113

Bostroem, K. A., Valenti, S., Sand, D. J., et al. 2020, ApJ, 895, 31

Botticella, M. T., Pastorello, A., Smartt, S. J., et al. 2009, MNRAS, 398, 1041

Breeveld, A. A., Landsman, W., Holland, S. T., et al. 2011, in American Institute of Physics Conference Series, Vol. 1358, American Institute of Physics Conference Series, ed. J. E. McEnery, J. L. Racusin, & N. Gehrels, 373–376

Brown, J. 2016, Transient Name Server Discovery Report, 2016-484, 1

Brown, P. J., Breeveld, A. A., Holland, S., Kuin, P., & Pritchard, T. 2014, Ap&SS, 354, 89

Brown, T. M., Baliber, N., Bianco, F. B., et al. 2013, PASP, 125, 1031

Bruch, R. J., Gal-Yam, A., Schulze, S., et al. 2021, ApJ, 912, 46

Byler, N., Dalcanton, J. J., Conroy, C., & Johnson, B. D. 2017, ApJ, 840, 44

Cai, Y. Z., Pastorello, A., Fraser, M., et al. 2018, MNRAS, 480, 3424

Calzetti, D., Armus, L., Bohlin, R. C., et al. 2000, ApJ, 533, 682

Cappellaro, E., Danziger, I. J., della Valle, M., Gouiffes, C., & Turatto, M. 1995, A&A, 293, 723

Chabrier, G. 2003, PASP, 115, 763

Chan, C., Müller, B., Heger, A., Pakmor, R., & Springel, V. 2018, ApJL, 852, L19

Chevalier, R. A., & Soderberg, A. M. 2010, ApJL, 711, L40

Chieffi, A., & Limongi, M. 2013, ApJ, 764, 21

Chugai, N. N., Chevalier, R. A., & Utrobin, V. P. 2007, ApJ, 662, 1136

Chun, S.-H., Yoon, S.-C., Jung, M.-K., Kim, D. U., & Kim, J. 2018, ApJ, 853, 79

Colless, M., Peterson, B. A., Jackson, C., et al. 2003, arXiv e-prints, , astro

Crawford, S. M., Still, M., Schellart, P., et al. 2010, in Society of Photo-Optical Instrumentation Engineers (SPIE) Conference Series, Vol. 7737, Society of Photo-Optical Instrumentation Engineers (SPIE) Conference Series, 25

Davies, B., & Beasor, E. R. 2018, MNRAS, 474, 2116

—. 2020, MNRAS, 496, L142

Davis, S., Hsiao, E. Y., Ashall, C., et al. 2019, ApJ, 887, 4

114

de Jaeger, T., Anderson, J. P., Pignata, G., et al. 2015, ApJ, 807, 63

de Jager, C., Nieuwenhuijzen, H., & van der Hucht, K. A. 1988, A&AS, 72, 259

de Vaucouleurs, G., de Vaucouleurs, A., Corwin, Herold G., J., et al. 1991, Third Reference Catalogue of Bright Galaxies (Springer, NY)

Delgado, A., Harrison, D., Hodgkin, S., et al. 2017, Transient Name Server Discovery Report, 2017-730, 1

Deng, J., Kawabata, K. S., Ohyama, Y., et al. 2004, ApJL, 605, L37

DES Collaboration, Abbott, T. M. C., Adamow, M., et al. 2021, arXiv e-prints, , arXiv:2101.05765

Dessart, L., & Hillier, D. J. 2005, A&A, 439, 671

—. 2011, MNRAS, 410, 1739

—. 2019, A&A, 625, A9

—. 2020, A&A, 642, A33

Dessart, L., Hillier, D. J., Audit, E., Livne, E., & Waldman, R. 2016a, MNRAS, 458, 2094

Dessart, L., Hillier, D. J., Livne, E., et al. 2011, MNRAS, 414, 2985

Dessart, L., Hillier, D. J., Waldman, R., & Livne, E. 2013, MNRAS, 433, 1745

Dessart, L., Hillier, D. J., Woosley, S., et al. 2016b, MNRAS, 458, 1618

Dessart, L., John Hillier, D., & Audit, E. 2017, A&A, 605, A83

Dessart, L., Livne, E., & Waldman, R. 2010, MNRAS, 408, 827

Dexter, J., & Kasen, D. 2013, ApJ, 772, 30

Dilday, B., Howell, D. A., Cenko, S. B., et al. 2012, Science, 337, 942

Doherty, C. L., Gil-Pons, P., Siess, L., & Lattanzio, J. C. 2017, PASA, 34, e056

Dolphin, A. 2016, DOLPHOT: Stellar photometry, ascl:1608.013

Drout, M. R., Massey, P., & Meynet, G. 2012, ApJ, 750, 97

Duffell, P. C. 2016, ApJ, 821, 76

Eisenstein, D. J., Weinberg, D. H., Agol, E., et al. 2011, AJ, 142, 72

115

Eldridge, J. 2017, Population Synthesis of Massive Close Binary Evolution, ed. A. W. Alsabti & P. Murdin (Cham: Springer International Publishing), 1–22

Eldridge, J. J., Fraser, M., Smartt, S. J., Maund, J. R., & Crockett, R. M. 2013, MNRAS, 436, 774

Eldridge, J. J., Izzard, R. G., & Tout, C. A. 2008, MNRAS, 384, 1109

Eldridge, J. J., Mattila, S., & Smartt, S. J. 2007, MNRAS, 376, L52

Eldridge, J. J., Stanway, E. R., Xiao, L., et al. 2017, PASA, 34, e058

Eldridge, J. J., Xiao, L., Stanway, E. R., Rodrigues, N., & Guo, N. Y. 2018, PASA, 35, 49

Elmhamdi, A., Danziger, I. J., Cappellaro, E., et al. 2004, A&A, 426, 963

Faber, S. M., Phillips, A. C., Kibrick, R. I., et al. 2003, Society of Photo-Optical Instrumentation Engineers (SPIE) Conference Series, Vol. 4841, The DEIMOS spectrograph for the Keck II Telescope: integration and testing, ed. M. Iye & A. F. M. Moorwood, 1657–1669

Fang, Q., & Maeda, K. 2018, ApJ, 864, 47

Fang, Q., Maeda, K., Kuncarayakti, H., Sun, F., & Gal-Yam, A. 2019, Nature Astronomy, 3, 434

Faran, T., Poznanski, D., Filippenko, A. V., et al. 2014, MNRAS, 442, 844

Fassia, A., Meikle, W. P. S., Chugai, N., et al. 2001, MNRAS, 325, 907

Fazio, G. G., Hora, J. L., Allen, L. E., et al. 2004, ApJS, 154, 10

Fesen, R. A., Shull, J. M., & Hurford, A. P. 1997, AJ, 113, 354

Filippenko, A. V. 1982, PASP, 94, 715

Fitzpatrick, E. L. 1999, PASP, 111, 63

Flewelling, H. A., Magnier, E. A., Chambers, K. C., et al. 2020, ApJS, 251, 7

Foreman-Mackey, D., Hogg, D. W., Lang, D., & Goodman, J. 2013, PASP, 125, 306

Förster, F., Moriya, T. J., Maureira, J. C., et al. 2018, Nature Astronomy, 2, 808

Förster, F., Cabrera-Vives, G., Castillo-Navarrete, E., et al. 2021, AJ, 161, 242

Fox, O. D., Silverman, J. M., Filippenko, A. V., et al. 2015, MNRAS, 447, 772

116

Fransson, C., & Chevalier, R. A. 1989, ApJ, 343, 323

Fraser, M., Reynolds, T., Inserra, C., & Yaron, O. 2016, Transient Name Server Classification Report, 2016-490, 1

Fraser, M., Magee, M., Kotak, R., et al. 2013, ApJL, 779, L8

Fremling, C., Dugas, A., & Sharma, Y. 2019, Transient Name Server Classification Report, 2019-590, 1

Fuller, J. 2017, MNRAS, 470, 1642

Gal-Yam, A. 2012, Science, 337, 927

—. 2019, ARA&A, 57, 305

Gal-Yam, A., Arcavi, I., Ofek, E. O., et al. 2014, Nature, 509, 471

Galbany, L., Stanishev, V., Mourão, A. M., et al. 2014, A&A, 572, A38

—. 2016a, A&A, 591, A48

Galbany, L., Hamuy, M., Phillips, M. M., et al. 2016b, AJ, 151, 33

Georgy, C. 2012, A&A, 538, L8

Gerke, J. R., Kochanek, C. S., & Stanek, K. Z. 2015, MNRAS, 450, 3289

Gessner, A., & Janka, H.-T. 2018, ApJ, 865, 61

Giacobbo, N., & Mapelli, M. 2019, MNRAS, 482, 2234

Glebbeek, E., Gaburov, E., de Mink, S. E., Pols, O. R., & Portegies Zwart, S. F. 2009, A&A, 497, 255

Gofman, R. A., Gluck, N., & Soker, N. 2020, MNRAS, 494, 5230

Goldberg, J. A., & Bildsten, L. 2020, ApJL, 895, L45

Goldberg, J. A., Bildsten, L., & Paxton, B. 2019, ApJ, 879, 3

Goldman, S. R., van Loon, J. T., Zijlstra, A. A., et al. 2017, MNRAS, 465, 403

Gordon, M. S., Humphreys, R. M., & Jones, T. J. 2016, ApJ, 825, 50

Graham, J. F. 2019, arXiv e-prints, , arXiv:1905.13197

Graham, M. J., Kulkarni, S. R., Bellm, E. C., et al. 2019, PASP, 131, 078001

Groenewegen, M. A. T., & Sloan, G. C. 2018, A&A, 609, A114

Guevel, D., & Hosseinzadeh, G. 2017, Dguevel/Pyzogy: Initial Release, vv0.0.1, Zenodo, doi:10.5281/zenodo.1043973

Guillochon, J., Parrent, J., Kelley, L. Z., & Margutti, R. 2017, ApJ, 835, 64

Gustafsson, B., Edvardsson, B., Eriksson, K., et al. 2008, A&A, 486, 951

Gutiérrez, C. P., Anderson, J. P., Hamuy, M., et al. 2014, ApJL, 786, L15

—. 2017a, ApJ, 850, 89

—. 2017b, ApJ, 850, 89

—. 2017c, ApJ, 850, 90

Gutiérrez, C. P., Anderson, J. P., Sullivan, M., et al. 2018, MNRAS, 479, 3232

Gutiérrez, C. P., Pastorello, A., Jerkstrand, A., et al. 2020, MNRAS, 499, 974

Hachisu, I., Kato, M., Saio, H., & Nomoto, K. 2012, ApJ, 744, 69

Hamuy, M. 2003, ApJ, 582, 905

Hamuy, M., & Pinto, P. A. 2002, ApJL, 566, L63

Hamuy, M., Phillips, M. M., Suntzeff, N. B., et al. 2003, Nature, 424, 651

Hamuy, M., Folatelli, G., Morrell, N. I., et al. 2006, PASP, 118, 2

Harutyunyan, A. H., Pfahler, P., Pastorello, A., et al. 2008, A&A, 488, 383

Heger, A., Fryer, C. L., Woosley, S. E., Langer, N., & Hartmann, D. H. 2003, ApJ, 591, 288

Heger, A., Jeannin, L., Langer, N., & Baraffe, I. 1997, A&A, 327, 224

Hillier, D. J., & Dessart, L. 2019, A&A, 631, A8

Hiramatsu, D., Howell, D. A., Moriya, T. J., et al. 2021a, ApJ, 913, 55

Hiramatsu, D., Howell, D. A., Van Dyk, S. D., et al. 2021b, Nature Astronomy,

Hirschi, R., Meynet, G., & Maeder, A. 2004, A&A, 425, 649

Hodgkin, S. T., Harrison, D. L., Breedt, E., et al. 2021, arXiv e-prints, , arXiv:2106.01394

Horne, K. 1986, PASP, 98, 609

Hosseinzadeh, G., Valenti, S., McCully, C., et al. 2018, ApJ, 861, 63

118

Howell, D. A. 2011, Nature Communications, 2, 350

Howell, D. A. 2017, Superluminous Supernovae, ed. A. W. Alsabti & P. Murdin (Cham: Springer International Publishing), 1–29

Howell, D. A. 2017, in American Astronomical Society Meeting Abstracts, Vol. 229, American Astronomical Society Meeting Abstracts #229, 341.10

Howell, D. A., & Global Supernova Project. 2017, in American Astronomical Society Meeting Abstracts, Vol. 230, American Astronomical Society Meeting Abstracts #230, 318.03

Howell, D. A., Sullivan, M., Perrett, K., et al. 2005, ApJ, 634, 1190

Hudgins, D., Herter, T., & Joyce, R. J. 1990, ApJL, 354, L57

Humphreys, R. M., Davidson, K., Jones, T. J., et al. 2012, ApJ, 760, 93

Inserra, C., Fraser, M., Smartt, S. J., et al. 2016, MNRAS, 459, 2721

Itagaki, K. 2018, Transient Name Server Discovery Report, 2018-285, 1

Janka, H. T., Müller, B., Kitaura, F. S., & Buras, R. 2008, A&A, 485, 199

Jerkstrand, A. 2017, Spectra of Supernovae in the Nebular Phase, ed. A. W. Alsabti & P. Murdin (Cham: Springer International Publishing), 795–842

Jerkstrand, A., Ertl, T., Janka, H. T., et al. 2018, MNRAS, 475, 277

Jerkstrand, A., Fransson, C., Maguire, K., et al. 2012, A&A, 546, A28

Jerkstrand, A., Maeda, K., & Kawabata, K. S. 2020, Science, 367, 415

Jerkstrand, A., Smartt, S. J., Fraser, M., et al. 2014, MNRAS, 439, 3694

Jerkstrand, A., Smartt, S. J., Sollerman, J., et al. 2015, MNRAS, 448, 2482

Jester, S., Schneider, D. P., Richards, G. T., et al. 2005, AJ, 130, 873

Johnson, B. D., Leja, J., Conroy, C., & Speagle, J. S. 2021, ApJS, 254, 22

Jones, S., Côté, B., Röpke, F. K., & Wanajo, S. 2019, ApJ, 882, 170

Jones, S., Hirschi, R., Nomoto, K., et al. 2013, ApJ, 772, 150

Kankare, E., Ergon, M., Bufano, F., et al. 2012, MNRAS, 424, 855

Kasen, D., & Woosley, S. E. 2009, ApJ, 703, 2205

Kawabata, K. S., Tanaka, M., Maeda, K., et al. 2009, ApJ, 697, 747

Kennicutt, Robert C., J. 1998, ARA&A, 36, 189

Kewley, L. J., Groves, B., Kauffmann, G., & Heckman, T. 2006, MNRAS, 372, 961

Khazov, D., Yaron, O., Gal-Yam, A., et al. 2016, ApJ, 818, 3

Kiewe, M., Gal-Yam, A., Arcavi, I., et al. 2012, ApJ, 744, 10

Kitaura, F. S., Janka, H. T., & Hillebrandt, W. 2006, A&A, 450, 345

Kochanek, C. S. 2014, ApJ, 785, 28

—. 2019, MNRAS, 483, 3762

—. 2020, MNRAS, 493, 4945

Kochanek, C. S., Shappee, B. J., Stanek, K. Z., et al. 2017, PASP, 129, 104502

Kozyreva, A., Nakar, E., & Waldman, R. 2019, MNRAS, 483, 1211

Kreckel, K., Armus, L., Groves, B., et al. 2014, ApJ, 790, 26

Kresse, D., Ertl, T., & Janka, H.-T. 2021, ApJ, 909, 169

Krisciunas, K., Contreras, C., Burns, C. R., et al. 2017, AJ, 154, 211

Kron, R. G. 1980, ApJS, 43, 305

Kuncarayakti, H., Maeda, K., Bersten, M. C., et al. 2015, A&A, 579, A95

Landolt, A. U. 1992, AJ, 104, 340

Leloudas, G., Hsiao, E. Y., Johansson, J., et al. 2015, A&A, 574, A61

Leonard, D. C., Filippenko, A. V., Li, W., et al. 2002a, AJ, 124, 2490

Leonard, D. C., Filippenko, A. V., Gates, E. L., et al. 2002b, PASP, 114, 35

Leung, S.-C., & Fuller, J. 2020, ApJ, 900, 99

Leung, S.-C., Nomoto, K., & Suzuki, T. 2020, ApJ, 889, 34

Levesque, E. M., Massey, P., Olsen, K. A. G., et al. 2005, ApJ, 628, 973

—. 2006, ApJ, 645, 1102

Li, H., & McCray, R. 1993, ApJ, 405, 730

120

Li, W., Van Dyk, S. D., Filippenko, A. V., et al. 2006, ApJ, 641, 1060

Lisakov, S. M., Dessart, L., Hillier, D. J., Waldman, R., & Livne, E. 2018, MNRAS, 473, 3863

Luckas, P., Trondal, O., & Schwartz, M. 2006a, Central Bureau Electronic Telegrams, 406, 1

Luckas, P., Trondal, O., Schwartz, M., & Subbarao, M. 2006b, IAUC, 8668, 2

Lyman, J. D., Bersier, D., James, P. A., et al. 2016, MNRAS, 457, 328

Maeda, K., Kawabata, K., Tanaka, M., et al. 2007, ApJL, 658, L5

Maguire, K. 2016, Type Ia Supernovae, ed. A. W. Alsabti & P. Murdin (Cham: Springer International Publishing), 1–24

Maguire, K., Jerkstrand, A., Smartt, S. J., et al. 2012, MNRAS, 420, 3451

Makovoz, D., & Marleau, F. R. 2005, PASP, 117, 1113

Makovoz, D., Roby, T., Khan, I., & Booth, H. 2006, Society of Photo-Optical Instrumentation Engineers (SPIE) Conference Series, Vol. 6274, MOPEX: a software package for astronomical image processing and visualization, 62740C

Maoz, D., Mannucci, F., & Nelemans, G. 2014, ARA&A, 52, 107

Martinez, L., & Bersten, M. C. 2019, A&A, 629, A124

Massey, P., Silva, D. R., Levesque, E. M., et al. 2009, ApJ, 703, 420

Mauerhan, J. C., Smith, N., Silverman, J. M., et al. 2013, MNRAS, 431, 2599

Maund, J. R., Mattila, S., Ramirez-Ruiz, E., & Eldridge, J. J. 2014a, MNRAS, 438, 1577

Maund, J. R., Reilly, E., & Mattila, S. 2014b, MNRAS, 438, 938

Maund, J. R., Smartt, S. J., & Danziger, I. J. 2005, MNRAS, 364, L33

Mauron, N., & Josselin, E. 2011, A&A, 526, A156

McCarthy, J. K., Cohen, J. G., Butcher, B., et al. 1998, Society of Photo-Optical Instrumentation Engineers (SPIE) Conference Series, Vol. 3355, Blue channel of the Keck low-resolution imaging spectrometer, ed. S. D'Odorico (Optical Astronomical Instrumentation), 81–92

McCully, C., Hiramatsu, D., Howell, D. A., et al. 2017, ApJL, 848, L32

McQuinn, K. B. W., Skillman, E. D., Dolphin, A. E., Berg, D., & Kennicutt, R. 2016, ApJ, 826, 21

Meynet, G., Chomienne, V., Ekström, S., et al. 2015, A&A, 575, A60

Miller, T. B., van Dokkum, P., Mowla, L., & van der Wel, A. 2019, ApJL, 872, L14

Miyaji, S., Nomoto, K., Yokoi, K., & Sugimoto, D. 1980, PASJ, 32, 303

Mokiem, M. R., de Koter, A., Vink, J. S., et al. 2007, A&A, 473, 603

Moriya, T., Tominaga, N., Blinnikov, S. I., Baklanov, P. V., & Sorokina, E. I. 2011, MNRAS, 415, 199

Moriya, T. J., Blinnikov, S. I., Tominaga, N., et al. 2013, MNRAS, 428, 1020

Moriya, T. J., & Eldridge, J. J. 2016, MNRAS, 461, 2155

Moriya, T. J., Förster, F., Yoon, S.-C., Gräfener, G., & Blinnikov, S. I. 2018a, MNRAS, 476, 2840

Moriya, T. J., Müller, B., Chan, C., Heger, A., & Blinnikov, S. I. 2019, ApJ, 880, 21

Moriya, T. J., Sorokina, E. I., & Chevalier, R. A. 2018b, SSRv, 214, 59

Moriya, T. J., Tominaga, N., Langer, N., et al. 2014, A&A, 569, A57

Moriya, T. J., Yoon, S.-C., Gräfener, G., & Blinnikov, S. I. 2017, MNRAS, 469, L108

Morozova, V., Piro, A. L., Fuller, J., & Van Dyk, S. D. 2020, ApJL, 891, L32

Morozova, V., Piro, A. L., Renzo, M., et al. 2015, ApJ, 814, 63

Morozova, V., Piro, A. L., & Valenti, S. 2017, ApJ, 838, 28

—. 2018, ApJ, 858, 15

Morrell, N., & Folatelli, G. 2006, Central Bureau Electronic Telegrams, 422, 1

Mowla, L., van der Wel, A., van Dokkum, P., & Miller, T. B. 2019, ApJL, 872, L13

Müller, B., Tauris, T. M., Heger, A., et al. 2019, MNRAS, 484, 3307

Nakaoka, T., Kawabata, K. S., Maeda, K., et al. 2018, ApJ, 859, 78

Nakaoka, T., Moriya, T. J., Tanaka, M., et al. 2019, ApJ, 875, 76

Neugent, K. F., Massey, P., Georgy, C., et al. 2020, ApJ, 889, 44

Noebauer, U. M., Taubenberger, S., Blinnikov, S., Sorokina, E., & Hillebrandt, W. 2016, MNRAS, 463, 2972

Nomoto, K. 1984, ApJ, 277, 791

—. 1987, ApJ, 322, 206

Nomoto, K., Sparks, W. M., Fesen, R. A., et al. 1982, Nature, 299, 803

Nomoto, K., Thielemann, F. K., & Yokoi, K. 1984, ApJ, 286, 644

Nomoto, K. I., Iwamoto, K., & Suzuki, T. 1995, PhR, 256, 173

Nordin, J., Brinnel, V., Giomi, M., et al. 2019, Transient Name Server Discovery Report, 2019-464, 1

Nozawa, T., & Fukugita, M. 2013, ApJ, 770, 27

Nozawa, T., Yoon, S.-C., Maeda, K., et al. 2014, ApJL, 787, L17

O'Connor, E., & Ott, C. D. 2011, ApJ, 730, 70

Ofek, E. O., Cameron, P. B., Kasliwal, M. M., et al. 2007, ApJL, 659, L13

Oke, J. B., Cohen, J. G., Carr, M., et al. 1995, PASP, 107, 375

Pastorello, A., Zampieri, L., Turatto, M., et al. 2004, MNRAS, 347, 74

Pastorello, A., Valenti, S., Zampieri, L., et al. 2009, MNRAS, 394, 2266

Patton, R. A., & Sukhbold, T. 2020, MNRAS, 499, 2803

Paxton, B., Bildsten, L., Dotter, A., et al. 2011, ApJS, 192, 3

Paxton, B., Cantiello, M., Arras, P., et al. 2013, ApJS, 208, 4

Paxton, B., Marchant, P., Schwab, J., et al. 2015, ApJS, 220, 15

Paxton, B., Schwab, J., Bauer, E. B., et al. 2018, ApJS, 234, 34

Paxton, B., Smolec, R., Schwab, J., et al. 2019, ApJS, 243, 10

Pejcha, O. 2020, The Explosion Mechanism of Core-Collapse Supernovae and Its Observational Signatures (Cham: Springer International Publishing), 189–211

Pejcha, O., & Thompson, T. A. 2015, ApJ, 801, 90

Perley, D. A. 2019, PASP, 131, 084503

Perley, D. A., Quimby, R. M., Yan, L., et al. 2016, ApJ, 830, 13

Perlmutter, S., Aldering, G., Goldhaber, G., et al. 1999, ApJ, 517, 565

Persson, S. E., Murphy, D. C., Krzeminski, W., Roth, M., & Rieke, M. J. 1998, AJ, 116, 2475

Pessi, P. J., Folatelli, G., Anderson, J. P., et al. 2019, MNRAS, 488, 4239

Poelarends, A. J. T., Herwig, F., Langer, N., & Heger, A. 2008, ApJ, 675, 614

Polshaw, J., Kotak, R., Chambers, K. C., et al. 2015, A&A, 580, L15

Popov, D. V. 1993, ApJ, 414, 712

Prieto, J. L., Garnavich, P. M., Phillips, M. M., et al. 2007, arXiv e-prints, , arXiv:0706.4088

Prieto, J. L., Kistler, M. D., Thompson, T. A., et al. 2008, ApJL, 681, L9

Quataert, E., Fernández, R., Kasen, D., Klion, H., & Paxton, B. 2016, MNRAS, 458, 1214

Quataert, E., & Shiode, J. 2012, MNRAS, 423, L92

Raab, H. 2012, Astrometrica: Astrometric data reduction of CCD images, ascl:1203.012

Renzo, M., Ott, C. D., Shore, S. N., & de Mink, S. E. 2017, A&A, 603, A118

Rieke, G. H., Young, E. T., Engelbracht, C. W., et al. 2004, ApJS, 154, 25

Riess, A. G., Filippenko, A. V., Challis, P., et al. 1998, AJ, 116, 1009

Rigon, L., Turatto, M., Benetti, S., et al. 2003, MNRAS, 340, 191

Rockosi, C., Stover, R., Kibrick, R., et al. 2010, in Ground-based and Airborne Instrumentation for Astronomy III, ed. I. S. McLean, S. K. Ramsay, & H. Takami, Vol. 7735, International Society for Optics and Photonics (SPIE), 355 – 365

Rodríguez, Ó., Pignata, G., Anderson, J. P., et al. 2020, MNRAS, 494, 5882

Sabach, E., & Soker, N. 2014, MNRAS, 439, 954

Salim, S., Rich, R. M., Charlot, S., et al. 2007, ApJS, 173, 267

Salpeter, E. E. 1955, ApJ, 121, 161

Sanders, N. E., Soderberg, A. M., Gezari, S., et al. 2015, ApJ, 799, 208

Satterfield, T. J., Katz, A. M., Sibley, A. R., MacAlpine, G. M., & Uomoto, A. 2012, AJ, 144, 27

Schlafly, E. F., & Finkbeiner, D. P. 2011, ApJ, 737, 103

Schlegel, E. M. 1996, AJ, 111, 1660

Schmidt, G. D., Stockman, H. S., & Smith, P. S. 1992, ApJL, 398, L57

Schulze, S., Yaron, O., Sollerman, J., et al. 2021, ApJS, 255, 29

Schwab, J., Podsiadlowski, P., & Rappaport, S. 2010, ApJ, 719, 722

Seibert, M., Wyder, T., Neill, J., et al. 2012, in American Astronomical Society Meeting Abstracts, Vol. 219, American Astronomical Society Meeting Abstracts #219, 340.01

Serkowski, K., Mathewson, D. S., & Ford, V. L. 1975, ApJ, 196, 261

Shappee, B. J., Prieto, J. L., Grupe, D., et al. 2014, ApJ, 788, 48

Shiode, J. H., & Quataert, E. 2014, ApJ, 780, 96

Silverman, J. M., Foley, R. J., Filippenko, A. V., et al. 2012, MNRAS, 425, 1789

Silverman, J. M., Nugent, P. E., Gal-Yam, A., et al. 2013a, ApJ, 772, 125

—. 2013b, ApJS, 207, 3

Silverman, J. M., Pickett, S., Wheeler, J. C., et al. 2017, MNRAS, 467, 369

Skibba, R. A., Engelbracht, C. W., Dale, D., et al. 2011, ApJ, 738, 89

Skrutskie, M. F., Cutri, R. M., Stiening, R., et al. 2006, AJ, 131, 1163

Smartt, S. J. 2009, ARA&A, 47, 63

—. 2015, PASA, 32, e016

Smartt, S. J., Valenti, S., Fraser, M., et al. 2015, A&A, 579, A40

Smith, J. A., Tucker, D. L., Kent, S., et al. 2002, AJ, 123, 2121

Smith, M. P., Nordsieck, K. H., Burgh, E. B., et al. 2006, in Proc. SPIE, Vol. 6269, Society of Photo-Optical Instrumentation Engineers (SPIE) Conference Series, 62692A

Smith, N. 2013, MNRAS, 434, 102

Smith, N. 2017, Interacting Supernovae: Types IIn and Ibn, ed. A. W. Alsabti & P. Murdin (Cham: Springer International Publishing), 403–429

Smith, N., Chornock, R., Silverman, J. M., Filippenko, A. V., & Foley, R. J. 2010, ApJ, 709, 856

Smith, N., Li, W., Filippenko, A. V., & Chornock, R. 2011a, MNRAS, 412, 1522

Smith, N., Li, W., Silverman, J. M., Ganeshalingam, M., & Filippenko, A. V. 2011b, MNRAS, 415, 773

Smith, N., Li, W., Foley, R. J., et al. 2007, ApJ, 666, 1116

Smith, N., Ganeshalingam, M., Chornock, R., et al. 2009, ApJL, 697, L49

Soker, N. 2019, MNRAS, 490, 2430

—. 2021, ApJ, 906, 1

Sollerman, J., Cumming, R. J., & Lundqvist, P. 1998, ApJ, 493, 933

Spiro, S., Pastorello, A., Pumo, M. L., et al. 2014, MNRAS, 439, 2873

Stanway, E. R., & Eldridge, J. J. 2018, MNRAS, 479, 75

Stetson, P. B. 2000, PASP, 112, 925

Strader, J. 2017, Transient Name Server Classification Report, 2017-833, 1

Strader, J., Chomiuk, L., Tremou, E., et al. 2017, The Astronomer's Telegram, 10616, 1

Stritzinger, M. D., Phillips, M. M., Boldt, L. N., et al. 2011, AJ, 142, 156

Stritzinger, M. D., Taddia, F., Fraser, M., et al. 2020, A&A, 639, A103

Sukhbold, T., & Adams, S. 2020, MNRAS, 492, 2578

Sukhbold, T., Ertl, T., Woosley, S. E., Brown, J. M., & Janka, H. T. 2016, ApJ, 821, 38

Taam, R. E., & Sandquist, E. L. 2000, ARA&A, 38, 113

Taddia, F., Stritzinger, M. D., Sollerman, J., et al. 2013, A&A, 555, A10

Taddia, F., Stritzinger, M. D., Bersten, M., et al. 2018, A&A, 609, A136

Tang, Q.-W., Wang, X.-Y., & Tam, P.-H. T. 2014, ApJ, 794, 26

Taramopoulos, A., Payne, H., & Briggs, F. H. 2001, A&A, 365, 360

Tarchi, A., Neininger, N., Greve, A., et al. 2000, A&A, 358, 95

Tartaglia, L., Sand, D. J., Valenti, S., et al. 2018, ApJ, 853, 62

Terman, J. L., Taam, R. E., & Hernquist, L. 1994, ApJ, 422, 729

Thompson, T. A., Prieto, J. L., Stanek, K. Z., et al. 2009, ApJ, 705, 1364

Tominaga, N., Blinnikov, S. I., & Nomoto, K. 2013, ApJL, 771, L12

Tonry, J. L. 2011, PASP, 123, 58

Tully, R. B., Rizzi, L., Shaya, E. J., et al. 2009, AJ, 138, 323,
   http://edd.ifa.hawaii.edu/

Turatto, M., Suzuki, T., Mazzali, P. A., et al. 2000, ApJL, 534, L57

Uenishi, T., Nomoto, K., & Hachisu, I. 2003, ApJ, 595, 1094

Ugliano, M., Janka, H.-T., Marek, A., & Arcones, A. 2012, ApJ, 757, 69

Valenti, S., Sand, D., Pastorello, A., et al. 2014, MNRAS, 438, L101

Valenti, S., Sand, D., Stritzinger, M., et al. 2015, MNRAS, 448, 2608

Valenti, S., Howell, D. A., Stritzinger, M. D., et al. 2016, MNRAS, 459, 3939

Van Dyk, S. D. 2016, Supernova Progenitors Observed with HST, ed. A. W. Alsabti &
   P. Murdin (Cham: Springer International Publishing), 1–27

Van Dyk, S. D., Davidge, T. J., Elias-Rosa, N., et al. 2012, AJ, 143, 19

Van Dyk, S. D., Zheng, W., Maund, J. R., et al. 2019, ApJ, 875, 136

van Loon, J. T., Cioni, M. R. L., Zijlstra, A. A., & Loup, C. 2005, A&A, 438, 273

Vink, J. S., de Koter, A., & Lamers, H. J. G. L. M. 2000, A&A, 362, 295

—. 2001, A&A, 369, 574

Walmswell, J. J., & Eldridge, J. J. 2012, MNRAS, 419, 2054

Wanajo, S., Müller, B., Janka, H.-T., & Heger, A. 2018, ApJ, 852, 40

Wanajo, S., Nomoto, K., Janka, H. T., Kitaura, F. S., & Müller, B. 2009, ApJ, 695, 208

Wood-Vasey, W. M., Wang, L., & Aldering, G. 2004, ApJ, 616, 339

Woosley, S. E., & Heger, A. 2015, ApJ, 810, 34

Woosley, S. E., Heger, A., & Weaver, T. A. 2002, Reviews of Modern Physics, 74, 1015

Woosley, S. E., & Weaver, T. A. 1995, ApJS, 101, 181

Wright, E. L., Eisenhardt, P. R. M., Mainzer, A. K., et al. 2010, AJ, 140, 1868

Wu, S., & Fuller, J. 2021, ApJ, 906, 3

Xue, M., Jiang, B. W., Gao, J., et al. 2016, ApJS, 224, 23

Yaron, O., & Gal-Yam, A. 2012, PASP, 124, 668, https://wiserep.weizmann.ac.il/

Yaron, O., Perley, D. A., Gal-Yam, A., et al. 2017, Nat. Phys., 13, 510

Yoon, S.-C., & Cantiello, M. 2010, ApJL, 717, L62

Zacharias, N., Finch, C. T., Girard, T. M., et al. 2013, AJ, 145, 44

Zackay, B., Ofek, E. O., & Gal-Yam, A. 2016, ApJ, 830, 27

Zapartas, E., de Mink, S. E., Justham, S., et al. 2021, A&A, 645, A6

—. 2019, A&A, 631, A5

Zha, S., Leung, S.-C., Suzuki, T., & Nomoto, K. 2019, ApJ, 886, 22

Zhang, J., Wang, X., József, V., et al. 2020, MNRAS, 498, 84

Zhang, K., & Bloom, J. S. 2020, ApJ, 889, 24